X線画像に基づく大腿骨の認識技術と内部固定用インプラントの評価法に関する研究

福 井 大 学 審 査

学位論文［博士（工学)］

A Dissertation Submitted to the
University of Fukui for the Degree of
Doctor of Engineering

A study on intelligent recognition technique of femur based on radiological images and evaluation method of internal fixation implants

X 線画像に基づく大腿骨の認識技術と内部固定用インプラントの評価法に関する研究

2021 September

Liu Kaifeng
刘锴锋

UNIVERSITY OF FUKUI

Abstract

Department of Advanced Interdisciplinary Science and

Technology Doctor of Engineering

The femur plays an important role in the human body. Due to its specific location and shape, the femur is susceptible to injury when subjected to external energy impact. For reasons such as reduced bone density, femoral fractures are highly prevalent in the elderly population and are associated with high mortality and disability rates. With the increasing trend of the ageing population worldwide, the diagnosis, treatment and postoperative evaluation of femoral fractures have become urgent public health issues.

Due to its minimally invasive nature, internal fixation is widely used as a treatment option to stabilize femoral neck fractures. The effectiveness and stability of fixation of the implant critical to the healing and functional recovery of femoral neck fractures and is an essential guide for the surgeon in selecting an internal fixation system. However, there is no long-term reliable assessment method to quantify the effectiveness of implant fixation without affecting patient behaviour and to synthesize long-term treatment data. The common evaluation method used by surgeons is to manually label and measure displacement data using computed tomography (CT) images of patients at different times, which requires an experienced surgeon and is very time consuming, and the measurements are susceptible to subjective images by the surgeon.

In this study, two solutions were proposed to solve the above problems. One is based on the analysis of Hansen's pin, we proposed a measurement method based

on 3D point cloud matching, in which the injured femur and implant were reconstructed in 3D and converted into point cloud data. Due to the properties of the femur, whose shape does not change significantly during the patient's recovery, we cropped the uninjured portion of the femur and performed rigid registration of the femur after surgery and after the one-year recovery period. That is, no projection transformation was performed during the registration process. The obtained point cloud alignment matrix was applied to the 3D point cloud of Hansson pins to transform the point cloud data of different periods into the same spatial coordinate system. The endpoint coordinate information of the pins was obtained by locating their axes and outer enclosing frames to analyze the migration of the implants.

In the second method, we constructed a CT image alignment framework with negative mutual information as the similarity function. In order to optimize the alignment speed, a multi-resolution pyramid framework is introduced to transform the alignment process into a hierarchical alignment process with different resolutions, which improves the alignment speed. To guarantee registration accuracy, we divide the registration into two stages: coarse registration and fine registration. In the process of fine registration, considering the symmetrical structure of the femur, we used 3D convolutional networks for biomedical image segmentation (3D-UNet), segmented the injured femur as a mask, and then converted the 3D point cloud to measure the displacement.

In the experimental part of the measurement of femoral internal fixation implant displacement, we used CT image data from 10 patients, including two CT images scanned within a one-year postoperative interval. The implant displacements obtained by manual measurement were used as comparison data for both measurement methods. Based on the 3D point cloud alignment method, the percentage of overlapping points was greater than 80% in all ten data sets after the alignment was completed. The final result of the measurement is smaller and faster than the measurement error of the traditional method. In the experiments to validate the multi-resolution framework-based method, the best metric was 0.9547 and 0.9450, respectively, during the training of the left femur and right femur segmentation models. By comparing the lengths of Hansson pins calculated by the femur-based registration method with the traditional method, we found that the method has good measurement stability. In addition, the experimental results show

that the error fluctuation of the traditional method is higher, and the measurement is unstable. More importantly, the proposed method in this paper is much less time consuming than the manual measurement and obtains similar measurement results. In addition, both methods achieve 3D display of femur and implant displacements. The degree of displacement can be visualized along with the quantification of displacement data.

In conclusion, we have developed a method for evaluating the stability of internal fixation implants for femoral neck injuries that can provide a basis for the surgeon's decision to select an internal fixation system. In addition, the proposed method of postoperative evaluation of femoral internal fixation allows for the most comprehensive evaluation of implant stability without mirroring the patient's normal life. Both evaluation methods not only quantify the amount of implant displacement but also visualize the displacement and provide input to the surgeon's decision making. The measurement results are stable and reliable, avoiding the subjective influence in the process of manual displacement measurement. The method proposed in this study is mainly used for fracture and postoperative implant stability evaluation and has a wide range of applications.

Acknowledgements

Before I had a chance to savour my life as a student, I had already arrived at the end of my doctoral studies. When I think back on my life in Japan, I feel happy when I first came to Japan, helpless when I faced difficulties alone, and grateful for the help I received from my advisor.

First, I would like to express my sincere gratitude to my supervisor, Prof. Dr. Kouki Nagamune. I still remember how nervous I was when I first met my supervisor after coming to Nagamune's lab. Prof. Nagamune greatly influenced my academic goals, and his hard work, conscientiousness, optimism, and rigour have always inspired me to overcome difficulties. When I encountered a bottleneck in my academic career, I received encouraging emails from Prof. Nagamune late at night, which helped me to regain my confidence. Although my supervisor is always busy every day, every time I encountered a problem, I received guidance and concern from him the first time. This made me feel very warm in my overseas study life alone.

I send my warm thanks to Prof. Keisuke Oe, who has provided me with many valuable suggestions in my academic research, which has further improved my knowledge of medical research. Each time Prof. Keisuke Oe's insightful comments on my dissertation helped me improve some mistakes that I did not realize in my dissertation.

Doctoral studies are a constant process of encountering difficulties and solving hardships, and I would like to thank all the students in the Nagamune lab for their help in this process. In particular, I would like to thank Mr Masanori Adachi for his help in Japanese, which I am not good at. I want to thank everyone in the research lab for being very friendly, and everyone is willing to help others no matter what problems they encounter.

Finally, I would like to thank my parents and sister for their support and understanding of my academic pursuits. The encouragement from my family has given me the courage to face every difficulty I encountered. It has been two years since I last returned to China, and I am very apologetic for not being there for my

family in their time of need. I am also profoundly grateful to my family for their dedication.

Liu Kaifeng

April 29, 2021, Fukui Japan

Contents

List of Figures

List of Tables

List of Tables

THA	**T**otal **H**ip **A**rthroplasty
CT	**C**omputerized **T**omography
APC	**A**nterior **P**osterior **C**ompression
LC	**L**ateral **C**ompression
VS	**V**ertical **S**hear
CMI	**C**ombined **M**echanical **I**njuries
AP	**A**ntero-**P**osterior
ISS	**I**njury **S**everity **S**core
CNN	**C**onvolutional **N**eural **N**etworks
ROI-Pooling	**R**egion **o**f **I**nterest-**P**ooling
FPN	**F**eature **P**yramid **N**etworks

Chapter 1
Introduction

The femur and pelvis are essential components of the human body and are connected to the trunk and lower extremities, as shown in Figure 1.1. Due to their particular position, the pelvis and femur are susceptible to fracture under external forces. The elderly are at a high risk of fracturing due to the decline in reflective function and osteoporosis. With the increasing population ageing population, the diagnosis, treatment, and postoperative evaluation of femoral fractures have become urgent public health issues.

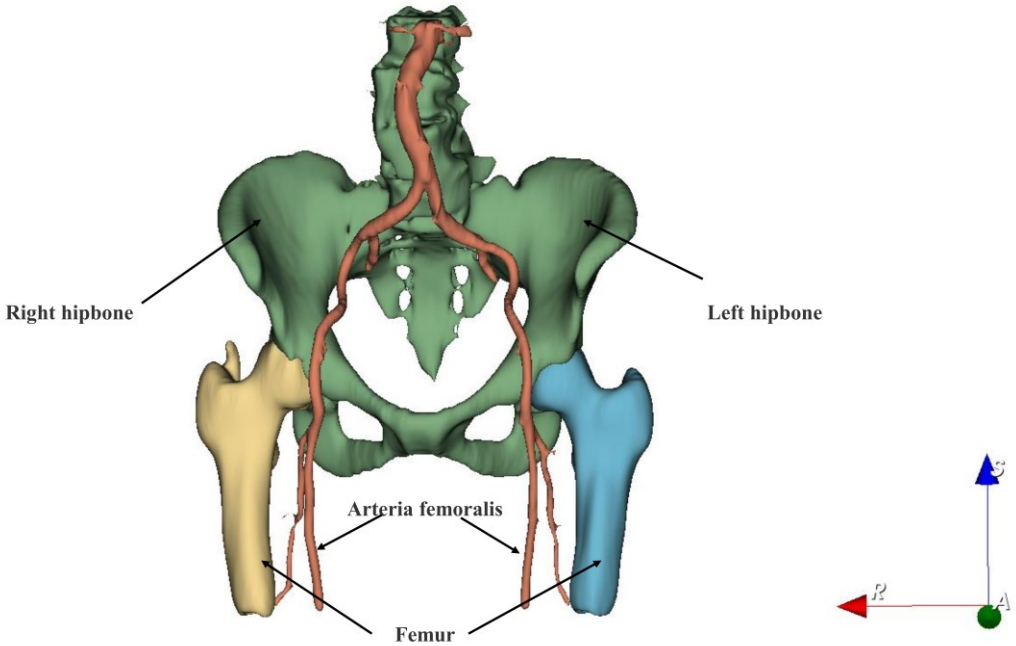

Figure 1.1 Structure of pelvic and femur.

Femoral neck fracture is a typical clinical traumatic fracture that occurs from the subtrochanter to the base of the femoral neck and accounts for approximately 3.61 % of systemic fractures [1] and nearly half of hip fractures [2]. The majority of patients are between the ages of 50 and 70, and studies have shown that the incidence in countries such as the United States and Japan is rising year by year [3]. In the next decade, along with the world's growing aging, the number of the elderly would be worrying. According to statistics, the number of people over the age of 65 will rise from 37.1 million to 77.2 million by 2040, and the incidence of hip fracture in the

elderly will rise as well, with 6.3 million patients worldwide predicted by 2050. The global hip fracture incidence is that at a rate of about 1.6 million per year [4]. The female population is twice as high as the male population of these patients [5].

Currently, for treating Garden I and Garden II stable femoral neck fractures, the use of internal fixation has become a consensus among orthopedic surgeons [6]-[8]. With internal fixation, the risk of infection, dislocation, femoral fracture, and laxity is lower than with total hip arthroplasty (THA) [9]. Additionally, internal fixation surgery provides minimal invasiveness and significantly reduces postoperative hospitalization time [10]. Various op-tons are currently available for stabilizing the internal fixation of femoral neck fractures, including cannulated screws, dynamic hip screws, proximal femoral locking plates, and other implants. The published literature suggests that implant failure is one of the main reasons for reoperation after internal femoral fixation [11]. Consequently, selecting the appropriate internal fixation solution for the patient to ensure postoperative implant stability with a minimum of movement is critical to the success of the procedure.

The current approach to studying the stability of internal fixation solutions is mainly biomechanical simulation. Researchers have used stress testers to simulate human gait behavior by applying pressure to synthetic bones or cadaveric femora with internal fixation and calculating the implant displacement as a stability criterion [12]–[15]. The use of finite element models is also one of the standard methods to simulate implants' mechanical properties such as stress, strain, the load to failure, and displacement [16]–[18]. The majority of the published literature evaluating internal fixation solutions utilizes simulation models created with a limited number of parameters. These models, therefore, only simulate the forces and displacements of the femur and implant in a particular situation. Nevertheless, during the patient's postoperative recovery, the femur is subjected to a complex combination of forces that vary with the movement's posture. Conventional biome-chemical simulation results, accordingly, do not provide a comprehensive evaluation of the implant.

Besides, femoral neck fractures require a lengthy recovery period after surgery, especially in the elderly, who have slow bone healing. Computerized tomography (CT) medical images are simple to obtain and can be acquired at all postoperative time points. It can provide the most direct information about the implant's

displacement under realistic postoperative motion conditions of the patient, which is not easy to achieve with traditional mechanical simulation and finite element methods. To obtain the displacement data of the target object inside the patient, the plastic surgeon primarily selects rigid references in the radiographic images and measures the target object's position relative to the reference object in different image sequences, respectively. The position coordinates are used to calculate the displacement of the target object in the different image sequences. Such a method is complicated to operate and vulnerable to the subjective factors of the surgeon.

1.1 Objectives

In this research, the femur and Hansson pins are used as objects to evaluate the stability of internal fixation implants used for femoral neck fractures. The aim to propose a method to segment the human left femur and right femur by trained image segmentation models such as 3D-UNet respectively. The method is able to generate masks of femur parts, which will be used as constraints for the next step of femur fine alignment.

Furthermore, the approach for fine alignment of rigid references to the fracture site using point cloud information from 3D reconstruction and multi-resolution pyramidal models is proposed using Hansson pins as internal fitting implants for femoral neck wounds. It is necessary and unique that the thesis examines the limitations of conventional approaches such as the restriction of biomechanical simulation in simulating the actions of patients and the inability to measure displacement quickly and accurately in the course of diagnostics using CT medical images. The experimental results show that these methods simplify manual displacement measurements dramatically and minimize the measuring time without reducing measurement accuracy compared to conventional manual displacement measurement methods.

1.2 Thesis Structure

This paper provides a brief description of the progress of research on femoral neck fractures using the current mainstream image segmentation techniques for

segmenting the proximal femur. The segmented information is used to analyze fracture detection methods further and evaluate postoperative stability.

The article is structured as follows.

Chapter 1 outlines a description of the main research background of the thesis and the relevant advances and standard methods for clinical treatment of femoral neck fractures. The purpose of this thesis and the significance of the study are described.

Chapter 2 introduces the biological anatomy of the femur, the trauma classifications, radiographs and CT scan techniques to provide theoretical support for further studies.

Chapter 3, a method using 3D point cloud matching of the femur, is proposed to evaluate internal fixation methods used for femoral neck injuries.

Chapter 4, using a multi-resolution pyramid-based method, CT images from different periods are aligned with the femur as the reference. The PCA algorithm is used to evaluate the implant's stability.

Chapter 5, summary and outlook, summarizes the main research contents and related results of this paper, analyzes the experiments and proposes better solutions for further work.

Chapter 2

Background study

2.1 Biological anatomy of the femur and injury classification

Figure 2.1 shows the anatomy of the femur. A femoral neck fracture is a fracture that occurs within the joint capsule between the articular surface of the femoral head and the rotor of the femur. The incidence of femoral neck fractures presents two poles in different age groups. It is common in older people who are prone to falls, and in a small number of younger people due to high-energy collisions such as vehicle collisions and falls from heights. Fractures of the femoral neck account for approximately 5% of all fractures.

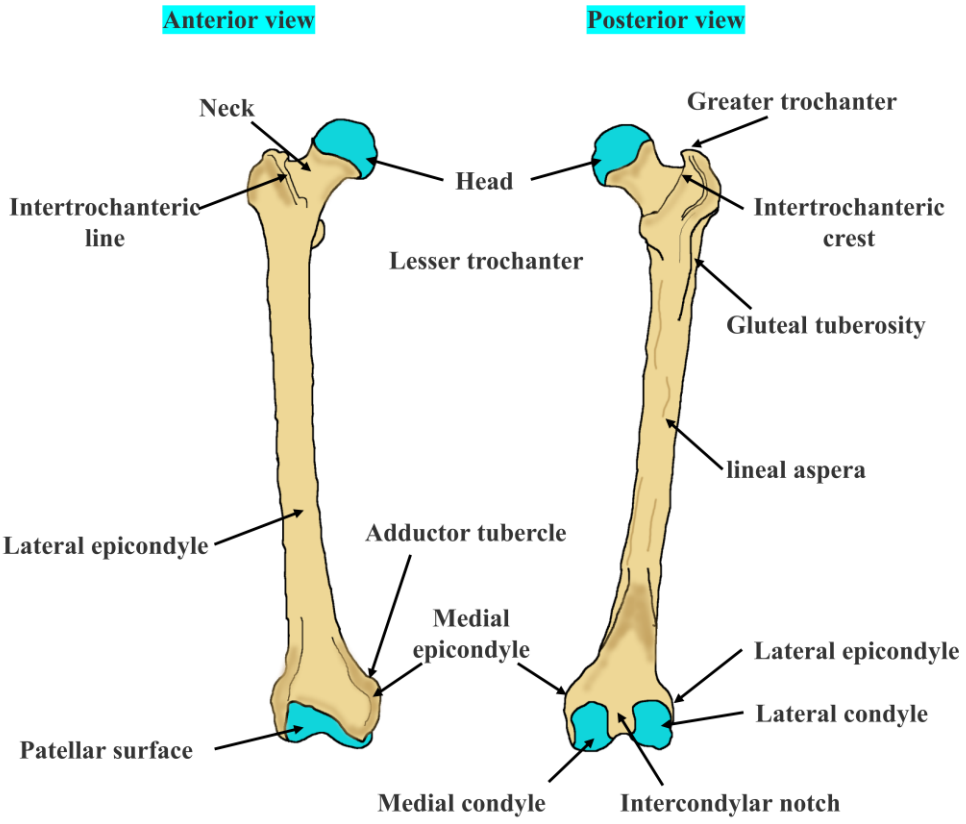

Figure 2.1 The anatomy of the femur.

The pattern of blood supply is unique to the femoral neck: approximately 1/5 of the proximal femoral head is supplied by a small concave artery within the femoral ligament, and this artery is usually not damaged in femoral neck fractures, but its supply area is too small. Most of the femoral head is supplied by branches of blood vessels entering from the base of the femoral neck at the attachment of the joint capsule, which enter the femoral head proximally within the cancellous bone of the femoral neck, but all these vessels are damaged and broken when the femoral neck is fractured, especially in intracapsular fractures.

Intra-articular hemorrhage following a femoral neck fracture leads to an increase in intracapsular pressure, when greater than that of the lesser concave artery, terminates the blood supply to that artery the other remaining undamaged arteries, thus exacerbating ischemia. The increased intracapsular pressure also impedes venous blood return, causing an increase in intramural pressure in the bone marrow cavity, which also exacerbates ischemia.

For stable femoral neck fractures, internal fixation is a widely accepted treatment modality by orthopaedic surgeons. A detailed evaluation of the patient's overall condition, including the type of fracture injury and the placement of pins for internal fixation, is required prior to performing internal fixation surgery. The implantation position cannot be accurately determined by x-rays alone. 3D reconstruction through CT images can provide a clear picture of the damage in the patient's body and formulate a treatment plan. The evaluation of the stability of the internal fixation is also crucial, as implant relaxation and displacement are the main causes of surgical failure and reoperation. Using CT images, it is possible to observe the displacement of the implant in the patient after surgery and provide a basis for the surgeon's postoperative evaluation.

Garden's typing divides intracapsular fractures into four types based on the degree of fracture displacement, and the schematic diagram of each type is shown in Figure 2.2 [19].

(1) Type I is an incomplete fracture.

(2) Type II is a complete fracture without displacement.

(3) Type III is a complete fracture with partial displacement and partial insertion of the fracture end, abduction of the femoral head, and mild external rotation and superior displacement of the femoral neck segment.

(4) Type IV is a completely displaced fracture with significant external rotation and upward displacement of the femoral neck segment. The articular capsule and synovial membrane are severely damaged.

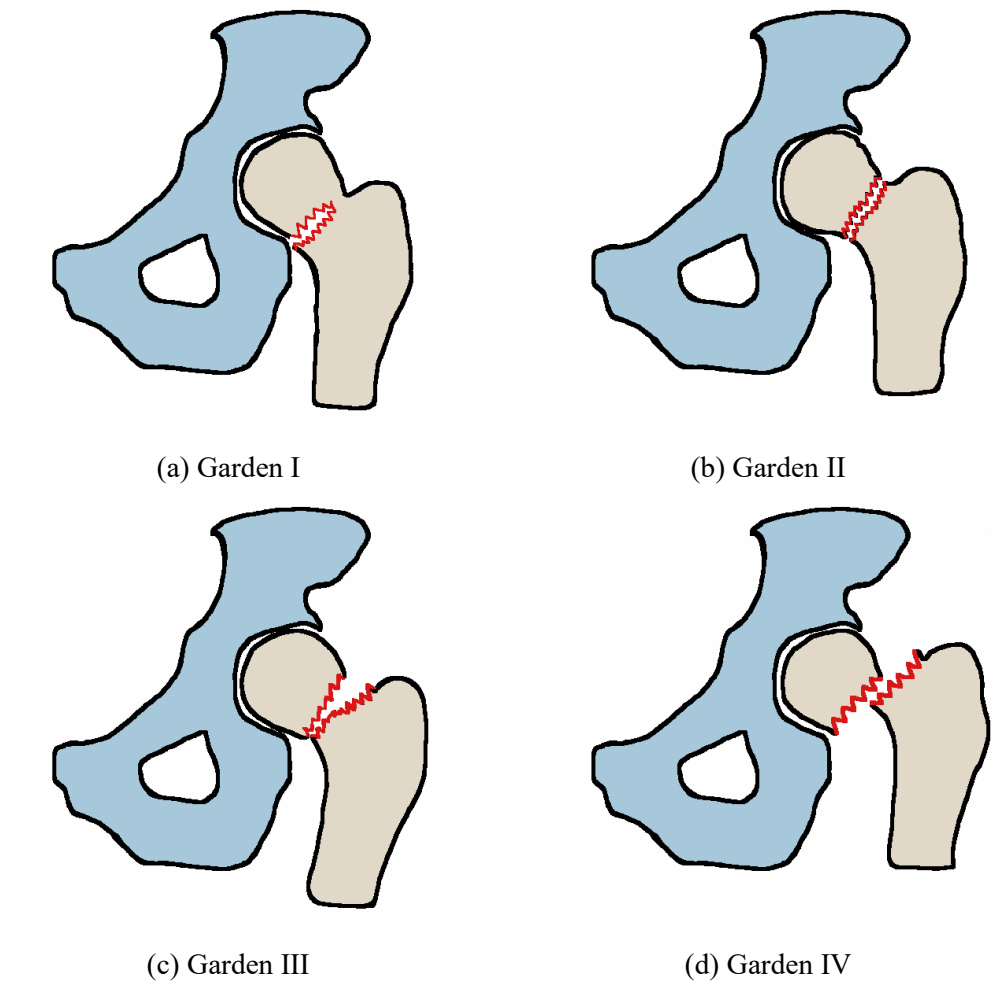

(a) Garden I (b) Garden II

(c) Garden III (d) Garden IV

Figure 2.2 Garden classification.

Type I and II are stable fractures because the fracture ends are not displaced or are less displaced and the degree of fracture damage is less.

Pauwels analysis is divided according to the angle of view between the fracture line and the perpendicular line of the femoral technique: Type I, Pauwel angle <30°; Type II, Pauwel angle between 30° and 50°, and Type III, Pauwel angle > 50° [20]. The greater the slope of the fracture line, the more unstable it is. Below 30°, the fracture surface is embedded between each other, the site is stable and easy to heal;

above 50°, it bears a great shear ground stress, the site is unstable, and the prognosis is poor. However, the precise measurement of this angle of view should be made only after placing the fracture distally in the internal rotation position and clearing the anteversion angle.

A number of factors affect the treatment of femoral neck fractures, including age, fracture type, and psychological factors, among others. Internal fixation, hemiarthroplasty, or complete hip replacement are the most common treatments for femoral neck fractures. Patients usually choose internal fixation to return the femoral head to health, and arthroplasty is the final cure for femoral neck fractures. Internal fixation is preferred for patients younger than 60 years old if there are no obvious symptoms of femoral head ischemia, according to conventional wisdom. Hip arthroplasty is preferred for patients over 80 years old with displaced fractures; for patients between 60 and 80 years old, treatment is determined by the patient's injury, fracture type, mental factors, and whether other systemic diseases are present [21].

2.2 Radiological assessment of traumatic injuries

2.2.1 Plain x-rays

X-ray is a typical orthopaedic trauma examination method. In X-ray imaging, the bones and the surrounding associated soft tissues can significantly contrast, so the bones are clearly imaged. X-ray plain film is easy to operate. It requires relatively low equipment and environment and does not require additional post-processing, so it is very suitable for the initial diagnosis of trauma and is very helpful for the judgment of injury and the guidance of subsequent treatment.

For pelvic trauma, an x-ray can accurately determine the severe instability of the pelvic ring and provide the basis for preliminary fracture typing. Anteroposterior (AP) films of the patient's pelvic ring can provide a great deal of information about pelvic injury. Anteroposterior radiographs are taken with the patient in a lying position. And the pelvic rim at an angle of 45° to 60° to the longitudinal axis of the trunk.

Using the left-right symmetry of the pelvic ring in the AP plain film, it is possible to determine whether the pelvic ring is significantly displaced. In addition, the integrity of the pubic symphysis can be clearly observed in the AP plain film. The

conditions for determining the occurrence of separation of the pubic symphysis and the damage to the pelvic ring anteriorly by a fracture of the pubic branch. The sacroiliac joint is usually accompanied by a crescentic fracture, which is one of the information that AP plain films can provide.

2.2.2 Computerized tomography scan

Computerized tomography (CT) scan is a method of generating cross-sectional images of the body based on the difference in the absorption of X-rays by various tissues of the body and reconstructing images in the coronal and sagittal planes on this basis. Compared to conventional X-ray films, CT scan images provide a higher resolution view of human tissue. Unlike X-ray films, CT images record three-dimensional image information and do not cause image overlap, which makes CT images play an irreplaceable role in femur injury diagnosis, treatment of internal fixation and postoperative evaluation.

Chapter 3
3D point cloud registration-based evaluation method for internal fixation implants

3.1 Introduction

Proximal femoral fractures are a skeletal trauma that occurs worldwide and is highly prevalent in the elderly [26]. These fractures account for nearly half of all hip fractures, and their incidence is increasing every year. There is a study that predicts a doubling of the number of proximal femur fractures in 2025 compared to 1990 [27]. Statistics available show that the ratio of male patients to female patients is 1: 2 [28]. The commonly used treatments for femur fractures are internal fixation, hemi-arthroplasty and total hip arthroplasty (THA)[29]. For the best functional result and early recovery allowing tolerable weight-bearing, pin fixation is one of the internal fixations widely used in treating femoral neck fractures [30].

Despite pin fixation is a frequent operation in clinical treatment for bone fractures, there are some severe complications following the insertion of implants, which are well introduced in the literature. Among them, loosening of screw or pin is one of the most common problems, representing 3% to 10% of all cases [31]. Besides, migration is another problem rarely mentioned in the literature but with high morbidity and mortality [32].

According to the quantitative analysis of medical images in eight clinical cases, Weil et al. classified medical migration types. They built biomechanical models for five different implants to explore the factors affecting migration. They argued that due to insufficient support for the pin's proximal end, instability of the medial cortex, and fixed friction sources within the femoral and neck, the pin's position would shift during the continuous alternating loading and unloading process [33]. In some published literature, bone density varying in different locations due to osteoporosis

is also one reason for pins' migration. Cavalcante et al. reported a case in which a 70-year-old female patient suffered the inter-trochanteric fracture due to a fall and was treated with cephalomedully osteosynthesis fixed. In the postoperative evaluation, it was found that the medial migration of the cephalic screw to the inner side of the pelvis resulted in slow fracture healing and pain to the patient. According to the analysis of the patient's health, it may be related to osteoporosis [34].

From the operative technique's perspective, the fracture varus malreduction occurred at the fracture site and was not reduced before the pins were inserted will lead to the movement of pins or lag screw [35]. Moreover, in the insertion of pins, there are operating technical errors that will also cause migration [36]. Lucke et al. presented a case that an old male patient with the inner fixation using Gamma3 nail and complained of pain on day 19 after the operation. Based on the result of radiographs, the lag screw migrates 5 cm into the pelvis, and it was believed that the unsuitability of implant design during nail in-sertion should be blamed [37].

In the literature review, the complication of migration resulting in significant risk for morbidity and mortality. First of all, avascular necrosis and nonunions are serious solae of femoral neck fractures. In [38], 69 cases of femoral neck fractures were treated with internal fixation, with nonunion and avascular necrosis up to 23.2% of the patients. Then, periprosthetic fractures are also severe complications that account for 5% to 8% [39]. Even in early cases, fractures were extending from the distal to the tip of the implant [40]. These will cause the penetration of the surrounding bones and the destruction of the joints and may compress or damage the internal tissues and organs inside the pelvis [41]. Thein et al. described the case of a 69-year-old woman who was performed with an internal fixation using a short gamma 3 nail due to a reverse interactive femur structure caused by a fall. At weeks after surgery, the radiological assessment shows the migration of the lag screw into the pelvis and compressing a branch of the left internal iliac artery causes embolism. Finally, the head and neck of the femur are removed [42].

Computerized tomography (CT) scan is a commonly used method to measure fracture displacement or implant displacement in patients with no trauma to the body. However, current CT-based medical 3D reconstruction techniques are mostly used to directly perform fracture displacement measurements on the reconstructed models.

Kaur, J., & Chopra, R. Kaur, J., & Chopra, R. performed CT scans and 3D reconstruction of the facial skeleton in one hundred patients with midface fractures and used the reconstructed 3D models to visualize the extent of major fractures and displacement of fragments [43]. In the literature [44], the authors used reconstructed 3D models to classify mandibular fractures and measure fracture displacement according to a reference. No method of fusing CT medical image information from multiple time points has been proposed to measure the movement of targets within the patient.

This chapter presents a method to measure implant displacement in the treatment of proximal femur fractures by overlapping multiple time points of CT image information, using the internal fixation implant Hansson pins as the object of study. The core of this method is to align the fractured femur using a 3D point cloud and convert the Hansson pins point cloud to the same coordinate system to measure the displacement.

3.2 Materials and Methods

3.2.1 Patients and CT images

Hyogo Prefectural Awaji Medical Center provided CT image data for 10 patients with proximal femur fractures from March 2012 to January 2015. All of these patients were treated with Hansson pins for internal fixation. These patients underwent CT scans preoperatively, postoperatively, and after a one-year recovery period. We selected two sets of CT sequences from each patient postoperatively and after the one-year recovery period as the study data for information extraction and fusion. Figure 3.1 presents the CT images preoperatively, postoperatively as well as a review of the patient one year later.

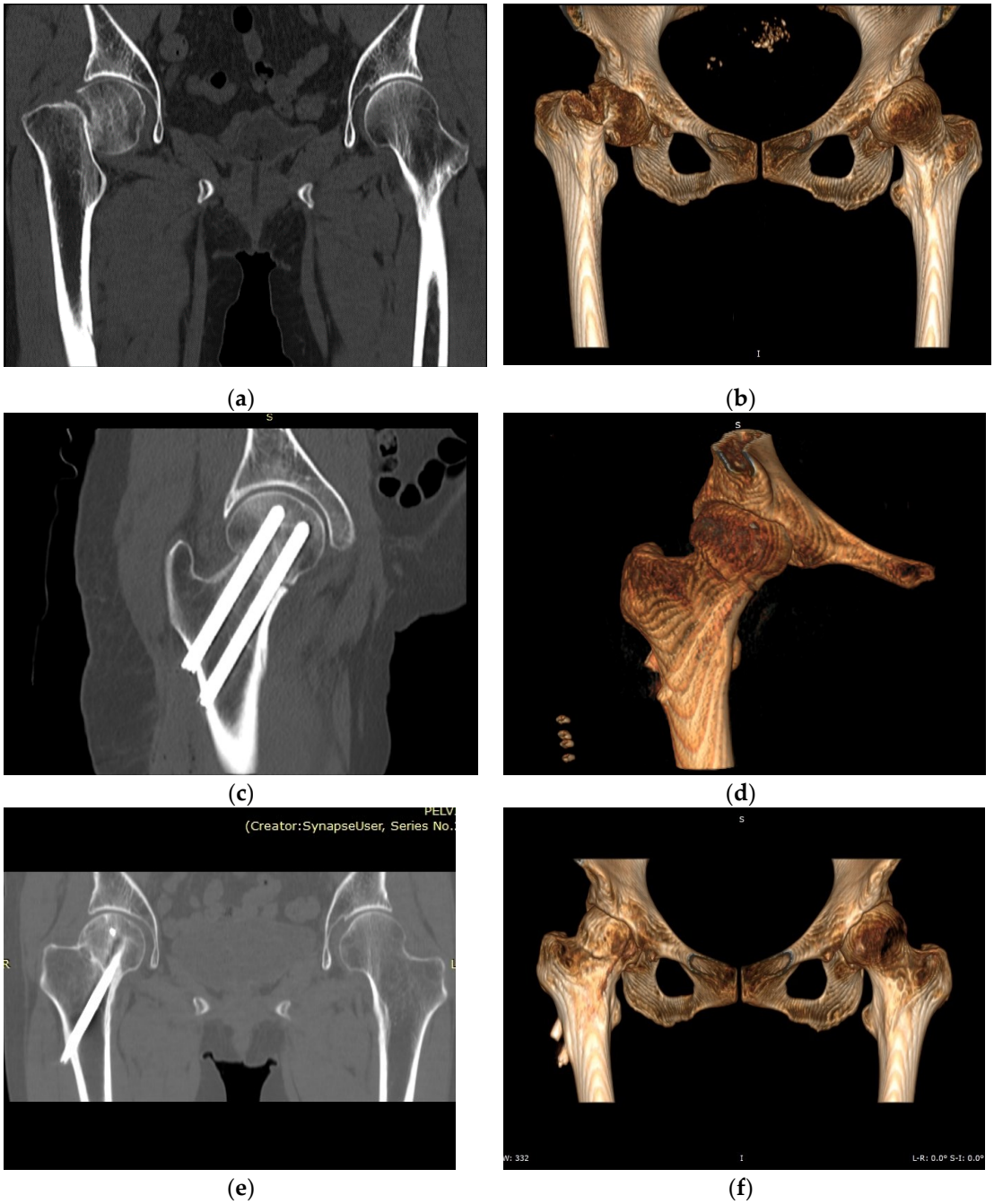

(**a**) (**b**)

(**c**) (**d**)

(**e**) (**f**)

Figure 3.1 Intracapsular fracture occurring due to low energy falls in the elderly: (a) Preoperative CT diagnostic image; (b) Preoperative 3D reconstruction model; (c) Postoperative 3D reconstruction model; (d) Postoperative 3D reconstruction model; (e) A year later 3D reconstruction model; (f) A year later 3D reconstruction model.

Hansson pins are unthreaded nails with a diameter of 6.5 mm and a length of 70 mm to 120 mm and were used as internal fixation implants in all cases. This internal fixation system was designed by Prof. Lars Ingvar Hansson of Lund University, Sweden [45]. Each pin consists of the outer sleeve and the inner movable hook pin. When the pins are implanted in the femur, the inner hook pin can be screwed out and engages in the subchondral bone, which provides the Hansson pins with a solid anti-

rotational force. As shoen in Figure 3.2, parallel positioning enables fracture dynamization, maintaining constant contact with bone during resorption. Physiological compression at the fracture site is permitted.

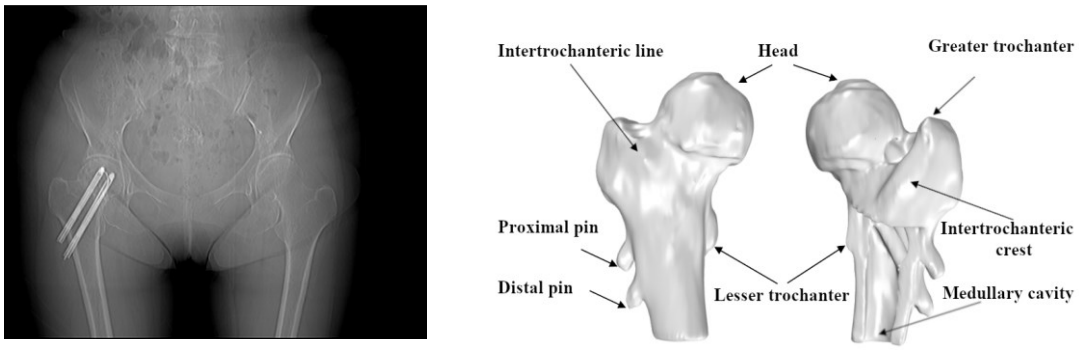

(**a**) (**b**)

Figure 3.2 Hansson pin fixation of femoral neck fractures: (a) Anteroposterior-posteroanterior X-ray (AP X-ray) of intracapsular fracture fixation with two Hansson pins; (b) Hansson pin location in the femur's anatomy.

3.2.2 Conventional methods of displacement measurement based on CT images

The traditional method of measuring implant movement is similar to measuring fracture displacement after a fracture. The surgeon estimates the fracture location or the target object's position based on a 3D reconstructed model. The reference and target object positions are positioned in the axial plane, coronal plane, and sagittal plane of the CT image, respectively, and a new coordinate system is created based on the characteristics of the reference. The criterion for reference selection is usually that the shape and anatomical position of the reference remains relatively constant over the CT sequences obtained from multiple time scans. Generally, the surgeon uses the greater trochanter, lesser trochanter, gluteal tuberosity, and other protuberance-containing regions as reference points.

CT images are usually shown as a two-dimensional image on a monitor that can be interpreted as an image created by three-dimensional spatial perspective projections. The information in the figure is subject to angular errors. In the majority of instances, a three-dimensional coordinate scheme must be rebuilt. Euclidean distances are calculated by finding the pins' endpoint coordinates in various CT image sequences. The equation is

$$d = \sqrt{(x_1 - x_2)^2 + (y_1 - y_2)^2 + (z_1 - z_2)^2} \ . \tag{3.1}$$

where (x_1, y_1, z_1) and (x_2, y_2, z_2) denote the coordinates of the same point in the two measurements, respectively.

3.2.3 3D reconstruction of CT images

Starting from the top left corner and creating 3D arrays/tensors of points and cells, the medical image is similar to the 2D natural image. The i axis grows to the right (width), the j axis grows to the bottom (height), and the k axis grows backward. Unlike two-dimensional natural images, the basic units that make up a CT image are voxels, and voxel (i, j, k) represents the intensity value of the voxel as (i, j, k).

To better describe the anatomical position of humans, doctors and radiologists usually use anatomical coordinate system. Figure 3.3 depicts the anatomical image coordinate system, which is made up of three planes that describe the standard anatomical position of a human: the axial plane, the sagittal plane, and the coronal plane. The green plane is the axial plane, which runs parallel to the ground and divides the body into above and below; the red plane is the sagittal plane, which runs perpendicular to the ground and divides the body into left and right; and the blue plane is the coronal plane, which runs perpendicular to the ground and divides the body into front and back.

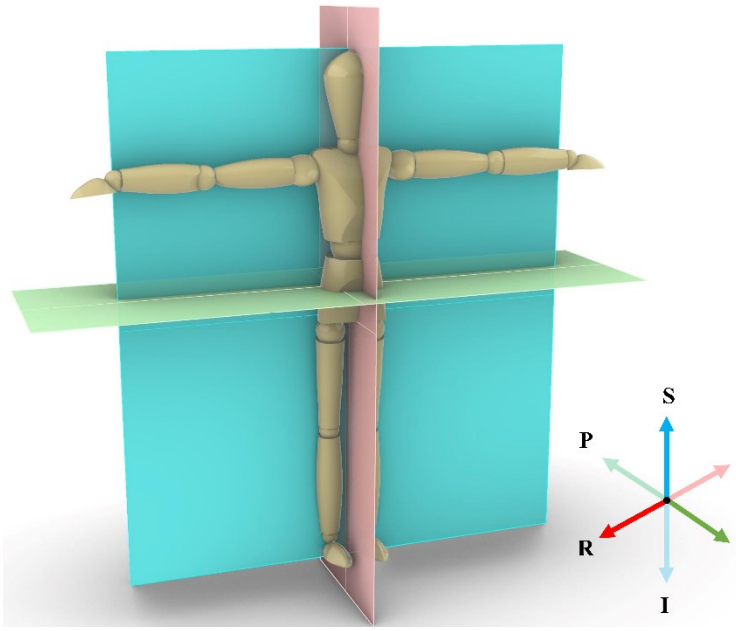

Figure 3.3 Anatomical coordinate system.

Commonly used anatomical coordinate systems are LPS (Left, Posterior, Superior) and RAS (Right, Anterior, Superior) coordinate systems. In this chapter we use the RAS coordinate system.

The process of 3D reconstruction using software can be regarded as the process of image conversion from Image coordinate system to anatomical coordinate system. The conversion process needs to consider the position of the image origin in the anatomical coordinate system and the distance between voxels.

Organs in different CT sequences have different coordinates in the same coordinate system. This is because different models of equipment have different parameters when performing CT scans, such as the layer spacing of the CT slice. In addition, the patient's body posture and position relative to the scanning device change with each CT scan. Image coordinate system is created with the scanning device as the reference, which causes the same target objects to not overlap completely in anatomical coordinate system as shown in Figure 3.4. The green and red models were created by 3D reconstructing different periods of CT images from the same patient. Both models use the RAS coordinate system, but both have different coordinates in space. At this point, the displacement results of the pins measured are the vector sum of the relative displacement of the implant and the displacement of the patient's femur in space.

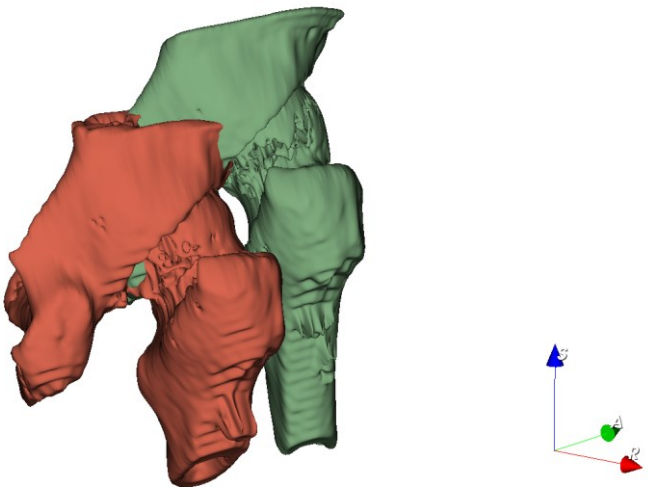

Figure 3.4 Models generated from different series of CT images are placed in the same coordinate system.

In order to accurately measure the displacement of pins, the 3D models of pins in both sequences need to be transformed into a coordinate system established with the same reference. In this chapter, we selected the proximal femur, which does not change significantly in morphology during the one-year recovery process, as the reference. The pin and femur were reconstructed and converted into 3D point clouds according to the postoperative CT images and the CT images after one year of recovery, respectively. To boost alignment accuracy and shorten matching time, various model reconstruction techniques are used in this article. For example, only the femur section without the femoral head and the pins were used as guides, as seen in Figure 3.5, since the femoral neck fracture will alter the femoral head location, and pin position will affect the matching accuracy. In addition, we remove the discontinuous, femur-independent interference points generated during the 3D reconstruction, and only retain the body of the proximal femur.

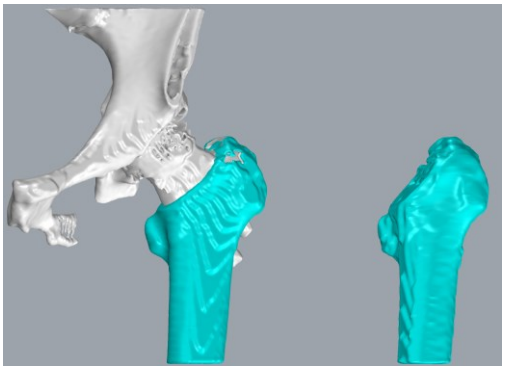

Figure 3.5 Selected a partial femur model containing the greater trochanter, intertrochanteric crest and filled the interior to use it as a reference.

Furthermore, partial femur data decreases the number of points in the model and the time it takes to convert coordinates. Moreover, we filled the model's interior during the model reconstruction process to minimize point cloud noise during the alignment process. The measurement method is depicted in Figure 3.6.

During model reconstruction, another technique has been to roughly position the axis of the femoral component used for orientation in the z-direction of space. As a consequence, the obtained model can be fine aligned directly. The implant shift can be calculated after applying the rotation matrix obtained from the alignment on the pins.

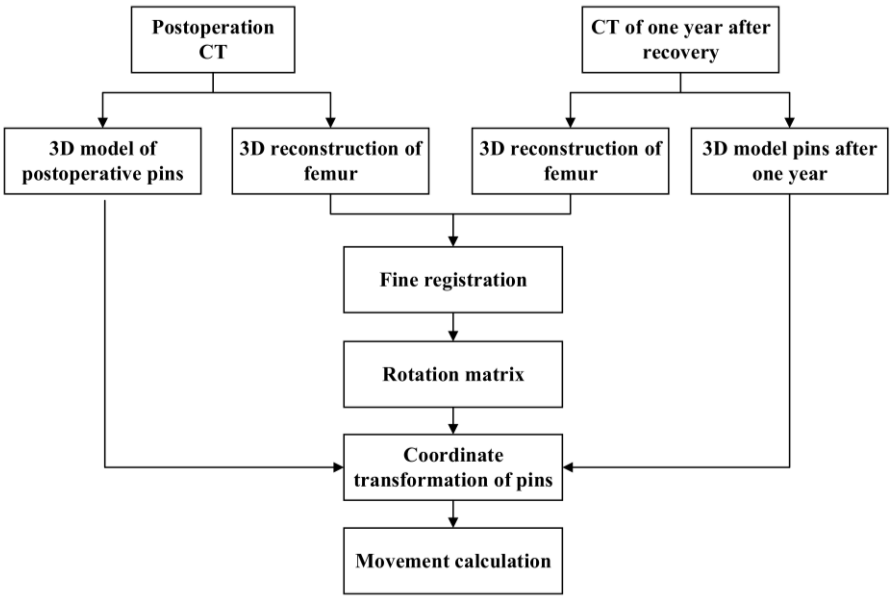

Figure 3.6 The process of 3D matching of femur and pins' coordinate transformation.

3.2.4 3D data format and conversion

In this section, we use two 3D model data formats, STL and PLY. The STL format was proposed by 3D Systems in 1987 and was originally used in stereolithography computer-aided design software. Currently, the STL file format is used as a common format for 3D modeling software, mainly for 3D printing and data conversion between different 3D modeling software. STL files are available in two representations: text and binary.

PLY files were introduced in 1994 and are mainly used to store the values obtained from 3D scans. This file format is mainly used to describe 3D objects in the form of polygon sets and is characterized by a simple method and comprehensive information storage. Unlike STL, this file format can store the color, transparency, material coordinates and data confidence of 3D objects, and can set different properties.

We can export the 3D model of femur and Hansson pin in STL format after 3D reconstruction of CT images using 3D slice software. For point cloud alignment, an STL file is converted to PLY point cloud data and down sampled.

3.2.5 Point cloud registration and key technologies

The registration of common 3D point clouds can be divided into two stages: coarse and fine registration.

Coarse registration refers to the initial alignment of the point cloud when the relative position of the point cloud is completely unknown. This step does not require the corresponding points in the two point clouds to achieve high precision coincidence, which just involves finding a rotation translation transformation matrix that allows the two point clouds to be relatively similar, and then converting the point cloud data to be aligned into a unified coordinate system, which can provide a good initial value for fine registration. Common coarse alignment algorithms:

Point Feature Histogram (PFH)-based alignment algorithms such as Sample Consensus Initial Alignment (SAC-IA). Alignment algorithms based on exhaustive search, such as 4-Point Congruent Set. The fine registration further realizes the transformation of the point clouds with the minimum variance of the corresponding point positions based on the effects of the coarse registration. It then obtains a more precise rotation-translation transformation matrix as a result. The algorithm's speed of operation and convergence to global optimization are heavily reliant on the initial transformation estimates and the establishment of correspondences during the iterative process. Consequently, the initial locations of the two point clouds are crucial to the outcome of fine recordings, and the correct collection of matching points cannot collapse into local extremes during the Iteration process, and the convergence and final recording accuracy of the algorithm are determined. Iterative Cloest Point (ICP). is one of the most widely used fine alignment algorithms.

In this section, we used the RAS coordinate system mentioned above for the initial coordinate system of the 3D model during the reconstruction of the femur and Hansson. Due to the specificity of CT medical images, the pose of the human skeleton is basically the same in the RAS coordinate system. Therefore, we can directly perform fine alignment on the femur and reduce the alignment time.

3.2.6 Iterative Closest Point

The Iterative Closest Point (ICP) algorithm is an iterative optimization approach that uses least squares to solve rigid transformations for optimal alignment of two sets of point clouds [46]. The aim of this algorithm is to use unique geometric features to find the rotation and translation parameters between the point cloud to be matched and the reference point cloud. The matched point cloud data is transformed using these parameters. The iterations will then be repeated until the transformed results

meet the convergence accuracy criteria. Figure 3.7 depicts the ICP algorithm execution procedure in this article.

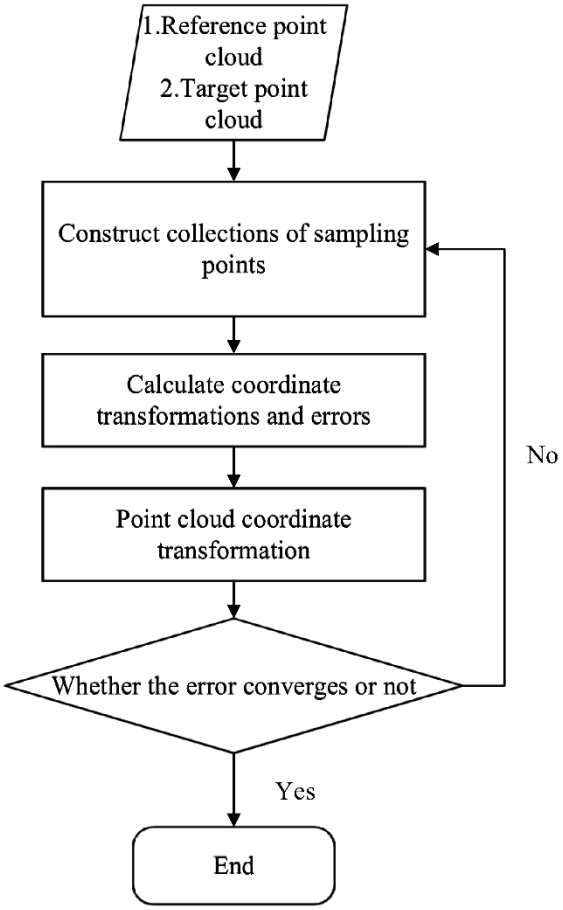

Figure 3.7 Alignment process using the ICP algorithm.

The basic algorithm of the ICP is as follows: $\mathbf{R_n}$ is defined as the rotation matrix after the Nth matching, and $\mathbf{t}$ is the translation vector.

Step 1: Take the two sets of point clouds **P** and **Q** as the initial point set of fine registration, where **P** is the point cloud to be matched and **Q** is the reference point cloud. **P**'s center is flattened to coincide with the center of **Q**, and the translation vector is $\mathbf{t_0}$.

Step 2: For each point $\mathbf{p_i}$ in **P**, we search for the corresponding point $\mathbf{q_i}$ in **Q**, from the corresponding points pairs, and then use the direction vector threshold to eliminate the wrong corresponding point pair. The product function is defined as

$$E(\mathbf{R}, \mathbf{t}) = \min \frac{1}{n} \sum_{i=1}^{n} \| \mathbf{q}_i - \mathbf{R} \cdot \mathbf{p}_i \|^2 \tag{3.2}$$

Then we compute the rotation matrix that minimizes the mean square of the distance.

Step 3: Point cloud **P** rotates according to the optimal solution in Equation (3.2), as follows.

$$\mathbf{P_n} = \mathbf{R_{n-1}} \cdot \mathbf{P_{n-1}}, (n >= 2) \tag{3.3}$$

The rotation matrix **R** can be solved by analyzing the covariance matrix between the corresponding point clouds.

Step 4: Determine whether the error $E(\mathbf{R}, \mathbf{t})$ is less than the preset value. If it is true, the iterations are stopped and failing, in which case Steps 2 and 3 are repeated until the iterations are completed. Then, the result can be expressed as

$$\mathbf{R} = \prod_{i=1}^{n} \mathbf{R}_i \tag{3.4}$$

$$t = \mathbf{R} \cdot t_0 \tag{3.5}$$

$$\mathbf{P}_n = \mathbf{R} \cdot \mathbf{P} + t_0 \tag{3.6}$$

The ICP algorithm based on neighborhood features is widely used. Compared with the traditional algorithm, it can improve the point search rate and improve the matching points' accuracy. The time cost of point cloud matching using the ICP algorithm depends on the femur part's points number. It also depends on the computing power of the CPU. In this chapter, the hardware information we used is shown in Table 3.1.

Table 3.1 Hardware information.

Hardware	Configuration
CPU	Core i7-2700k 3.50GHz
Memory	16GB
Operating system	Windows10

3.3 Experiment

3.3.1 Data Preprocessing and Registration of Models

In this stage, we used a 3D Slicer [47] to reconstruct the 3D model. The 3D Slicer is a free open-source software for medical image analysis, visualization, and image-guided therapy research, which can be used on a variety of operating systems.

We adopted the threshold tool and build-in Otsu algorithm to generate 3D models of the femur and the Hansson pin, respectively. Otsu is an algorithm to calculate the binarization segmentation threshold of an image proposed by Japanese scholar Otsu in 1979 [48]. Among the 3D models, the skeleton model's minimum threshold range was 150, and the minimum threshold range of the pins were 1400. We applied these parameters, and the 3D models were reconstructed. Figure 3.8 lists the models used in the next stage. Figure 3.8 a,b presents how the pins and femur models were constructed, respectively, and that they share the same coordinate system. With the processing of 10 sets data, we obtained 10 sets of models. Then, fine registration was performed using the ICP method.

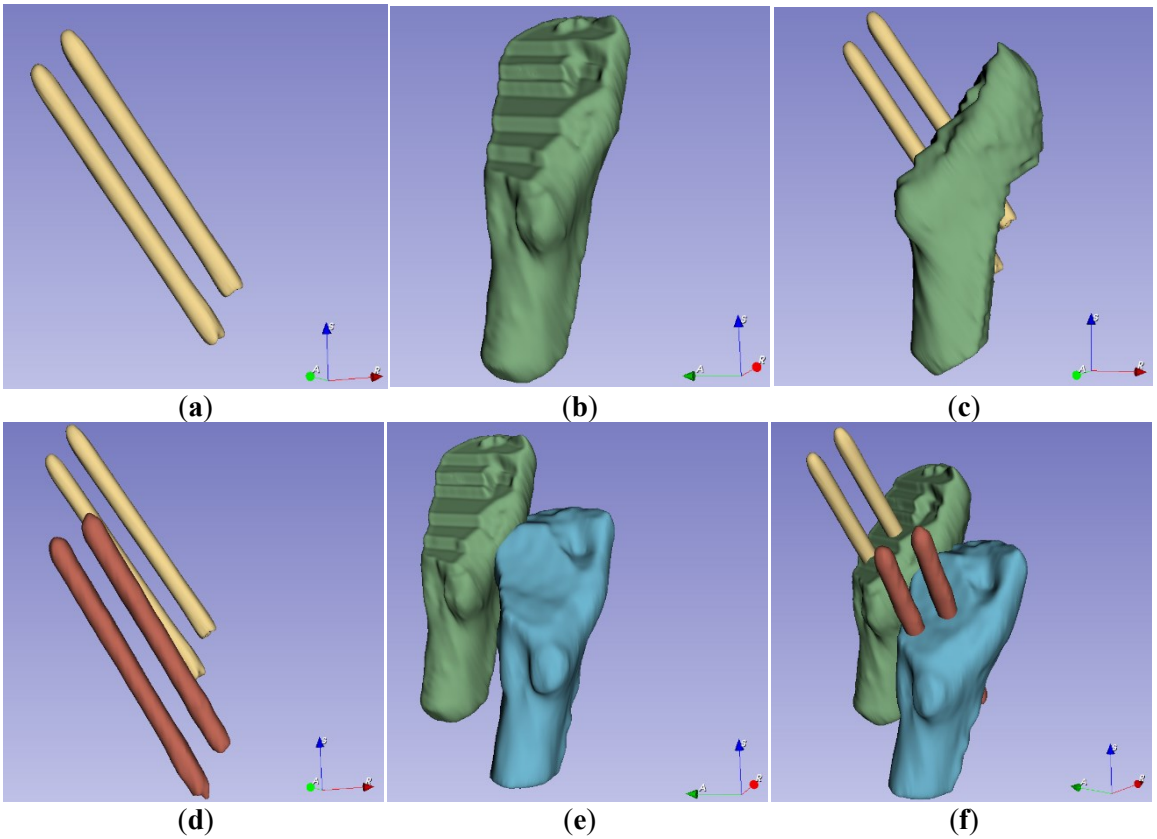

Figure 3.8 Using 3D Slicer to reconstruct 3D model of bone with the same initial direction: (a) The pins model reconstructed using CT images. (b) A part model of the femur. (c) Assembling the pins and femur from the same group of CT images in the same coordinate system. (d) Comparison of pins from different sets of dates. (e) The green model comes from

postoperative data, and the blue model comes from CT images after a one-year recovery period. (f) All the models use the same initial direction.

According to the different iterations' registration results listed in Table 3.2, the registration accuracy remained stable when the iteration exceeded 125. The improvement in registration accuracy is less than 0.1% for an increase of 25 iterations. After the alignment was completed, we used the obtained rotation matrix and translation vectors to calculate the pin and femur positions.

Table 3.2 Result of accuracy comparison with different iterations.

Iterations	Points Whose Distance Is Less Than 0.5 mm		
	Case 1	Case 2	Case 3
25	22.83%	5.77%	31.63%
50	42.22%	10.87%	57.82%
75	37.75%	21.31%	57.27%
100	37.50%	50.17%	57.18%
125	37.50%	49.12%	57.19%
150	37.50%	49.08%	57.19%
175	37.50%	49.09%	57.20%
200	37.50%	49.08%	57.20%
225	37.51%	49.08%	57.22%
250	37.51%	49.08%	57.24%

3.3.2 Measurement Based on 3D Coordinate System of CT Images

3.3.2.1 Manually Measure the Displacement Reference Value

To verify the effectiveness and accuracy of the method proposed in this chapter, we manually aligned the femur and pins models and measured the displacement of the pin endpoints. By repeating the operation three times, as we mentioned above, and calculating the average value, we obtained the reference values of actual pin migration used to verify the traditional method's accuracy and the accuracy of the method proposed in this chapter. Figure 3.9 explains that we imported two groups of 3D reconstruction models before and after a one-year recovery period into the Rhinoceros software [49], matched the two models artificially, and measured the displacement data of the corresponding point of the pins.

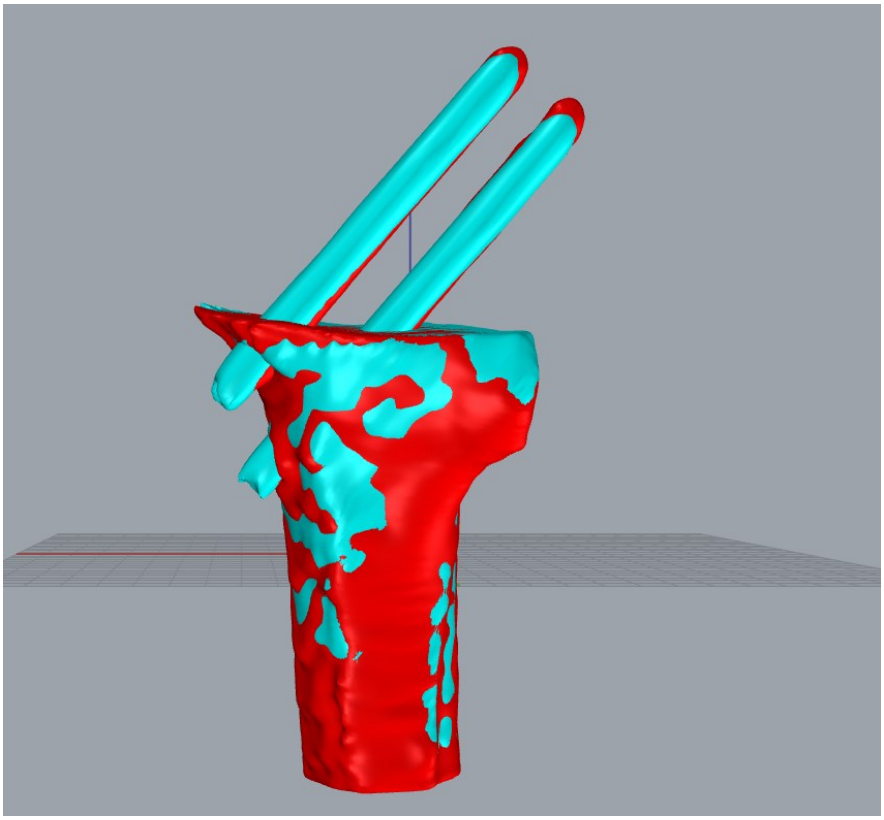

Figure 3.9 Manually matched and measured displacement of pins.

3.3.2.2 Measurement by the Traditional Method

The first step in creating a coordinate system is to locate the centerline of the medullary cavity, which hardly changes its relative position without significant damage to the corpus femoris. In the software RadiAnt [50], we performed multiplanar reconstruction to CT images to obtain three mutually perpendicular planes. By moving two of the planes, we found the medullary cavity's projection, and located the centerline of the medullary cavity, line **L**, according to the position information in two mutually perpendicular planes. The process of locating line **L** is shown in Figure 3.10. The midline of the medullary cavity was defined as the z-axis, with its positive direction pointing to the greater trochanter.

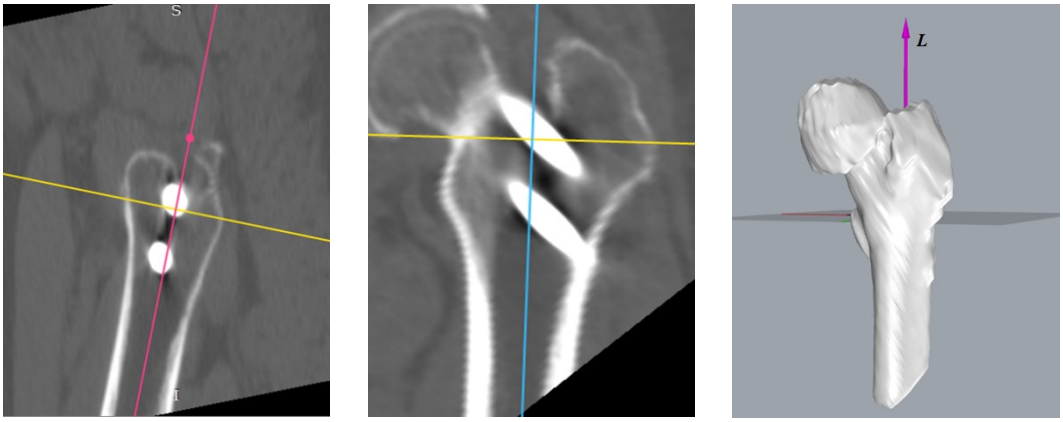

(a) (b) (c)

Figure 3.10 According to the projection of the medullary cavity centerline in plane 1 (red line) and plane 2 (blue line), we located the position of: (a) plane 1, (b) plane 2, and (c) the centerline in the 3D model.

Figure 3.11a shows the process of creating the x-axis in the left femur. We located the farthest point A from the z-axis in the lesser trochanter region. The line that goes through point A and vertical to the z-axis is the x-axis, with the positive direction pointing to point A. Additionally, the intersection point O of the x-axis and z-axis is the coordinate origin. We defined the line passing through the origin and perpendicular to the x-axis and z-axis as the y-axis. The positive direction of the y-axis is the direction of the cross product of the z-axis and the x-axis. Similarly, the coordinate system in the right femoral model, as shown in Figure 3.11c, was established.

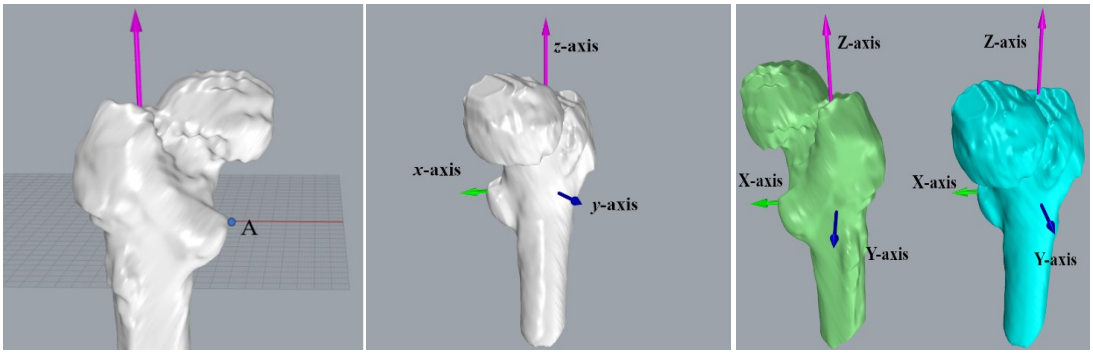

(a) (b) (c)

Figure 3.11 Establishing the right and left femoral coordinate system: (a) reference point A in the lesser trochanter region. (b) left femoral coordinate system, and (c) comparison of the left and right femoral coordinate systems.

Figure 3.12 presents the established coordinate system, the process of measuring the proximal pin's coordinates, and the distal pin's endpoints.

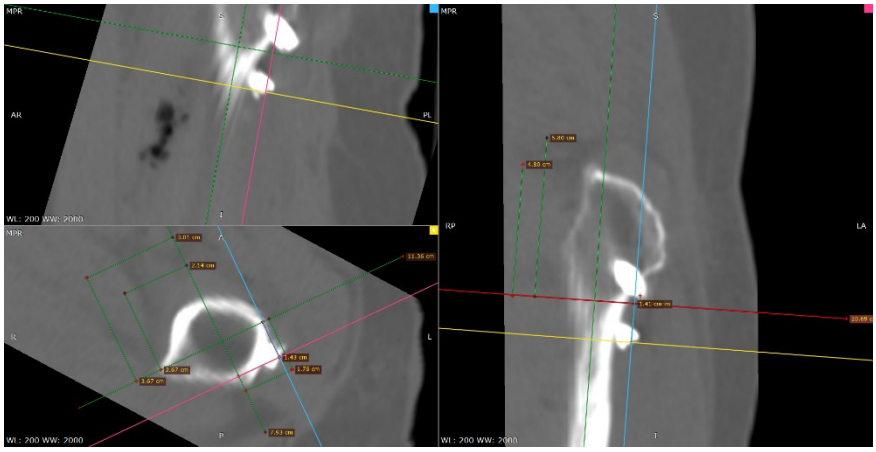

Figure 3.12 Using software RadiAnt to measure the position of the Hansson pin.

3.3.2.3 Calculation of Pin Displacement Based on Point Cloud Matching

Figure 3.13 exposes the position of the pins and femur after registration with 125 iterations. The white point cloud is the data measured after the surgery, and the green one is the point cloud to be matched based on the data after a one-year recovery. Then the green point cloud transforms into the red part using position transformation.

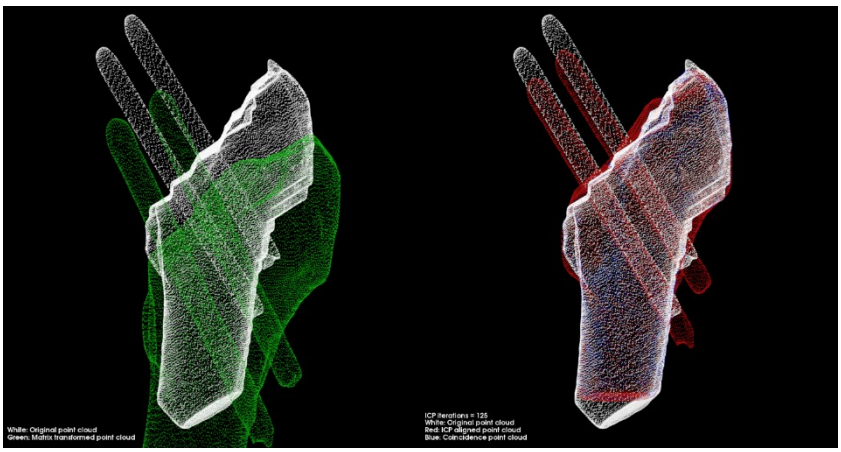

Figure 3.13 Performing position transformation on the pins and femur after registration with 125 iterations.

We eliminated the femur part and quantitatively calculated the pins' movement in the three-dimensional space. As shown in Figure 3.14, the principal component analysis was used to calculate the direction vector for obtaining relative angles, drawing the bounding box for the pins, and obtaining the endpoint coordinates. Meanwhile, the actual length of pins listed in Table 3.3 was used to calibrate the length scale of the point cloud data.

Table 3.3 The length of pins and information of patients in each case.

Case No.	Length of Pins		Gender	Age
	Proximal	Distal		
1	80	90	female	79
2	85	95	female	76
3	80	95	female	81
4	90	100	female	65
5	80	90	female	78
6	75	90	female	85
7	85	100	female	79
8	85	90	female	77
9	80	90	female	73
10	80	90	female	67

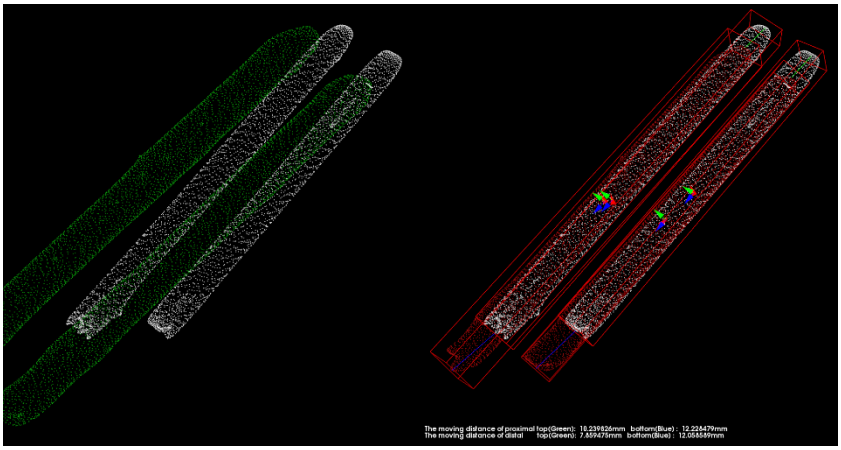

Figure 3.14 Visualization of pins' movement and calculation of moving distance and rotation angle.

After femur registration, each femur model's alignment effect was evaluated on the basis of the distance from each point in the converted femur point cloud to the nearest point in the benchmark point cloud. This subsection used the maximum value, the average value, the proportion of points whose distance was less than 2 mm, and the proportion of points whose distance was less than 0.5 mm as evaluation criteria.

Additionally, for a more precise analysis of the Hansson pin's movement in the femur, we transformed the aligned model into a new coordinate system. Figure 3.15 describes the new coordinate system of the proximal pin and the distal pin after transformation. The red pin depicts the point cloud of the Hansson pin postoperatively, and the green pin depicts the point cloud of the Hansson pin one year after surgery.

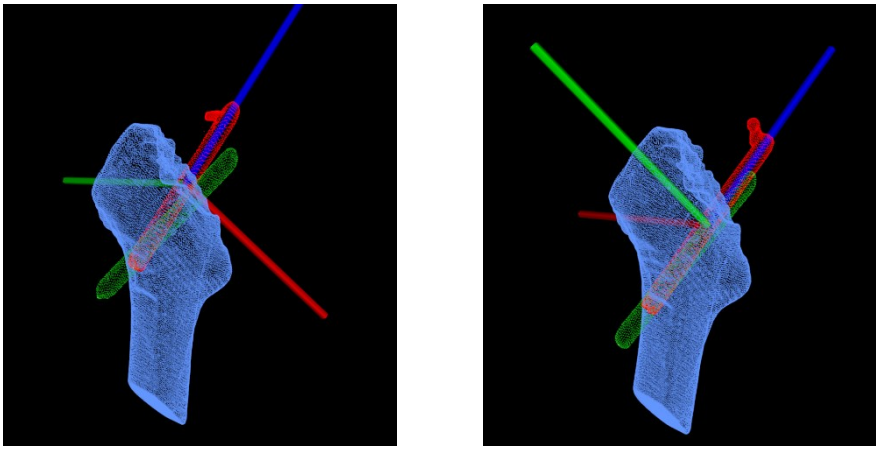

(**a**) (**b**)

Figure 3.15 Converting the aligned point cloud data to the new coordinate system: (a) the coordinate system of the proximal pin; (b) the coordinate system of the distal pin.

According to the 3D point cloud of the postoperative proximal pin in Figure 3.15a, we fit its central axis, the blue axis, as the z-axis of the new coordinate system, pointing to the top of the Hansson pin as the positive direction. The center of the point cloud of the pin served as the origin of the coordinate system. Passing the origin, the y-axis was established parallel to the hook pin, and the positive direction was defined as the direction of the pin elongation. Furthermore, the y-axis vector and z-axis vector's cross product was used as the vector of the red x-axis. Moreover, the direction was determined by the result of the cross product. Similarly, a new coordinate system for the distal pin in Figure 3.15b was built.

3.4 Results

3.4.1 Result of Registration

Table 3.2 describes the result of registration with different iterations. From the proportion of points whose distance to the corresponding point was less than 0.5 mm, when the iterations reached 125, the optimal result could be obtained.

Table 3.4 shows the time used when the iterations were set to 125 for the 3 cases in the table that were randomly selected from the 10 cases. The time increased by five milliseconds for each additional point.

Table 3.4 Time consumed for different size point cloud registrations.

Case No	Number of Points in the Model	The Time Spent (min)

1	47,354	3.80
2	17,878	1.69
3	26,357	1.75

Figure 3.16 presents the data preprocessing results, and the 10 groups of models based on the CT images. The models' main directions in each group were the same and could be used directly for fine registration.

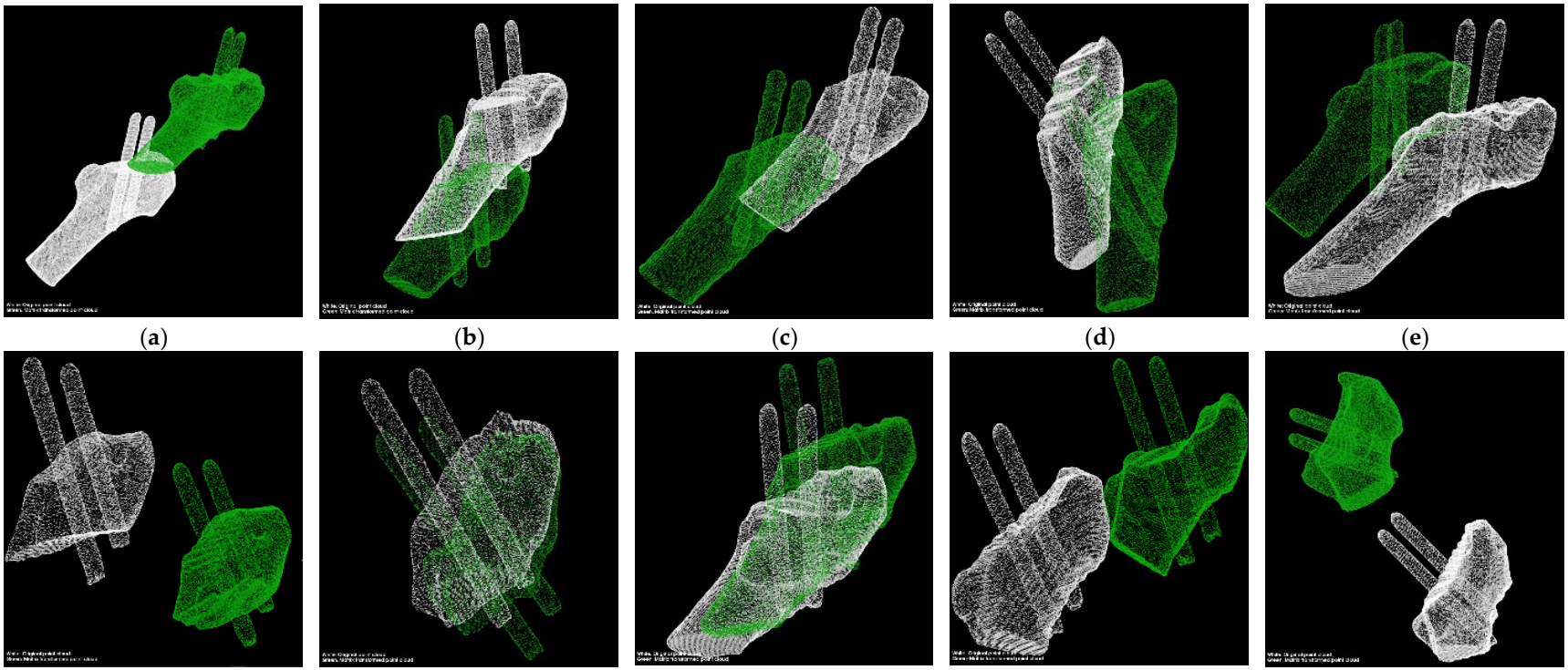

Figure 3.16 3D point clouds preprocessing. (a) to (j) are the point clouds of the 10 cases without performing alignment, respectively. The white point cloud is generated based on postoperative CT images, and the green point cloud is generated based on CT images scanned after the one-year recovery period.

Figure 3.17 displays the results after the position transformation using the matrix obtained from the registration. The red model can be regarded that the green model in Figure 3.16 transformed their coordinate systems to the coordinate systems of white models.

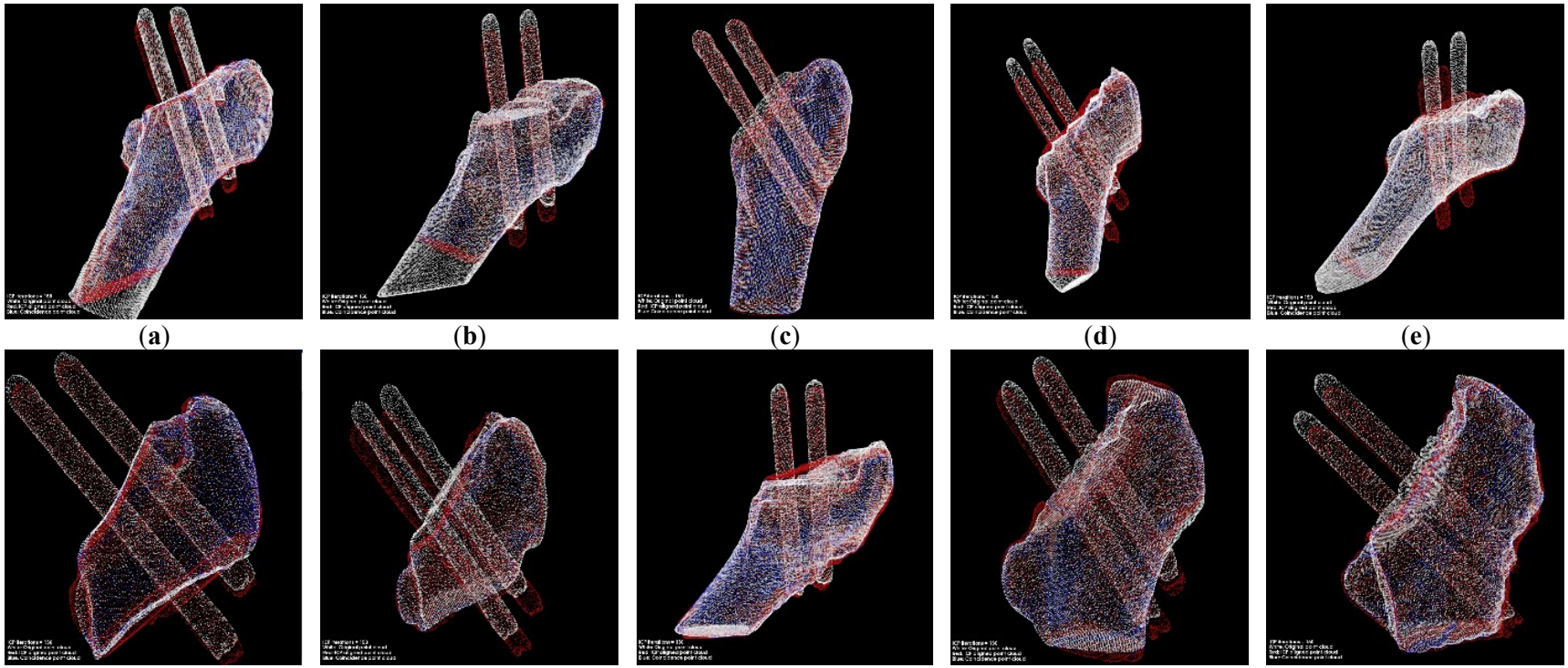

Figure 3.17 Transformation using the matrix obtained from the registration. (a) to (j) are the point clouds after fine registration for each of the 10 cases. The white point cloud is generated based on the postoperative CT images. The red point cloud is transformed

As shown in Figure 3.18, the pins and the bounding boxes of each group were transformed into the same coordination system. The green lines in the image represent the distance traveled by the top vertexes of the pins, and the blue lines describe the moving distance of the lower vertexes of the pins. What is more, the movement of each pin can be perceived from various perspectives. The data we obtained are listed in Table 3.5, and all data are retained with two significant digits.

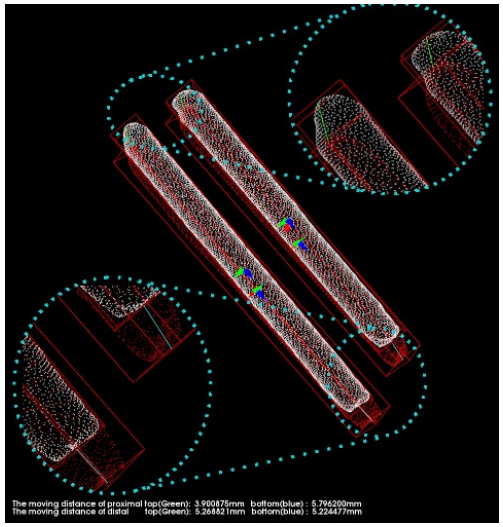
The moving distance of proximal top(Green): 3.990875mm bottom(blue) : 5.796200mm
The moving distance of distal top(Green): 5.268821mm bottom(blue) : 5.224477mm

(a)

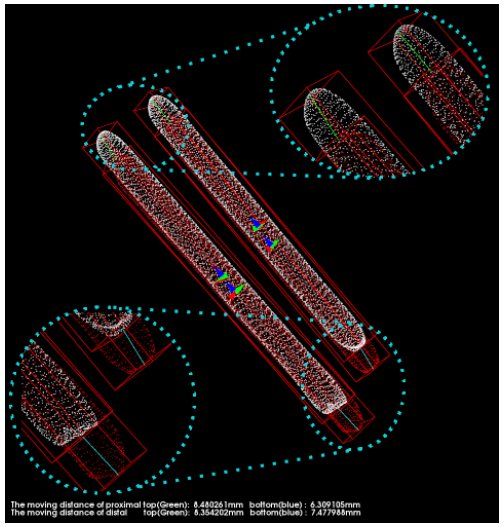
The moving distance of proximal top(Green): 8.480261mm bottom(blue) : 6.309105mm
The moving distance of distal top(Green): 8.354202mm bottom(blue) : 7.477988mm

(b)

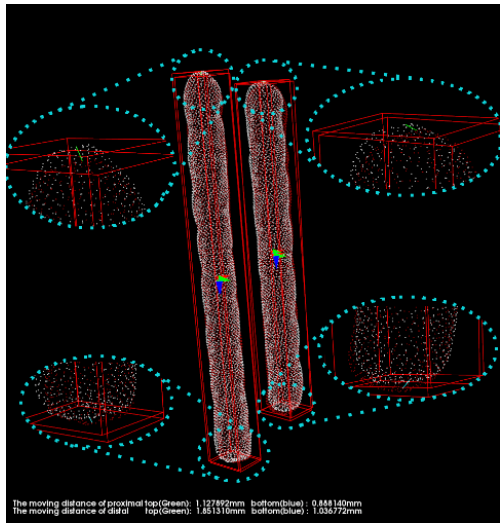
The moving distance of proximal top(Green): 1.127892mm bottom(blue) : 0.888140mm
The moving distance of distal top(Green): 1.851310mm bottom(blue) : 1.036772mm

(c)

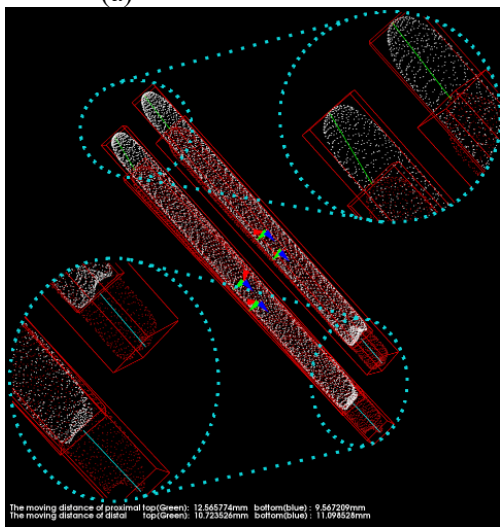
The moving distance of proximal top(Green): 12.565774mm bottom(blue) : 9.567209mm
The moving distance of distal top(Green): 10.723526mm bottom(blue) : 11.098528mm

(**d**)

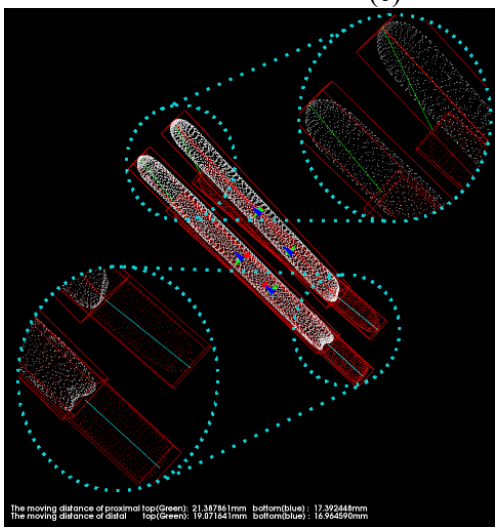
The moving distance of proximal top(Green): 21.367861mm bottom(blue) : 17.392448mm
The moving distance of distal top(Green): 19.871641mm bottom(blue) : 16.964590mm

(**e**)

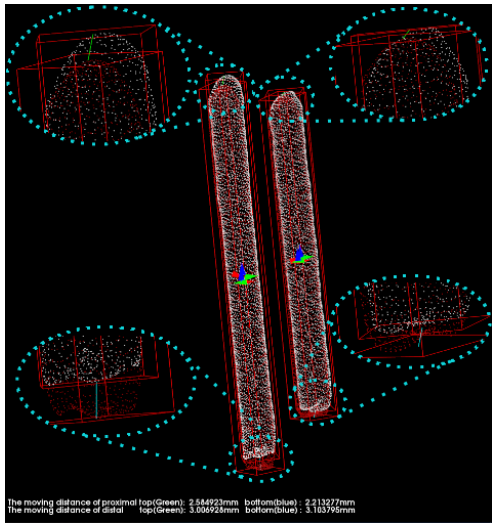
The moving distance of proximal top(Green): 2.584923mm bottom(blue) : 2.213277mm
The moving distance of distal top(Green): 3.006928mm bottom(blue) : 3.183795mm

(**f**)

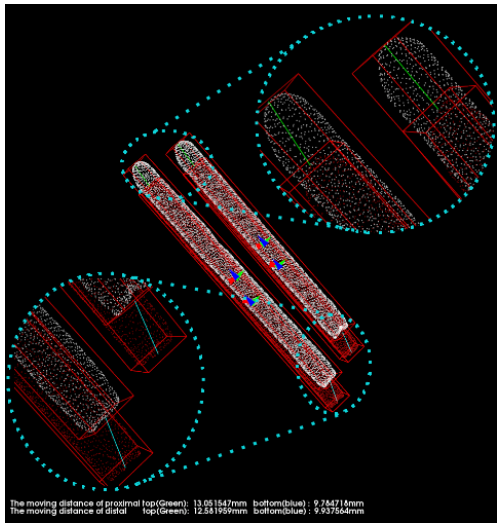
The moving distance of proximal top(Green): 13.051547mm bottom(blue) : 9.784716mm
The moving distance of distal top(Green): 12.581959mm bottom(blue) : 9.937564mm

(**g**)

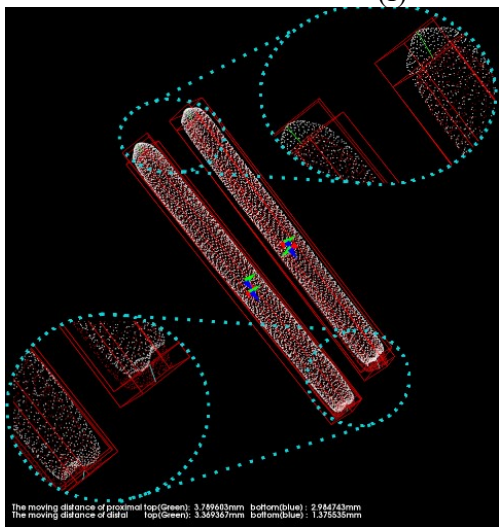
The moving distance of proximal top(Green): 3.789603mm bottom(blue) : 2.994743mm
The moving distance of distal top(Green): 3.369367mm bottom(blue) : 1.375535mm

(**h**)

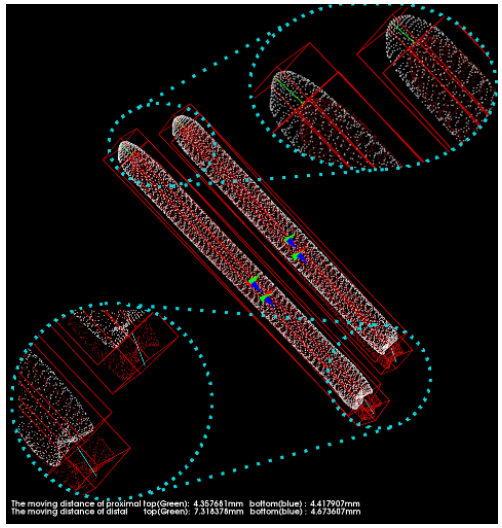
The moving distance of proximal top(Green): 4.357681mm bottom(blue) : 4.417907mm
The moving distance of distal top(Green): 7.316378mm bottom(blue) : 4.673607mm

(**i**)

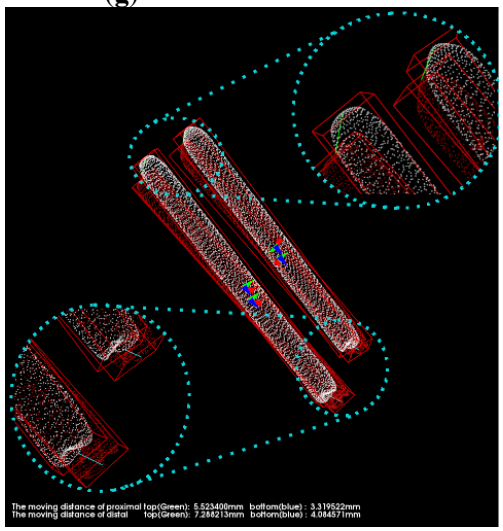
The moving distance of proximal top(Green): 5.523400mm bottom(blue) : 3.319522mm
The moving distance of distal top(Green): 7.288213mm bottom(blue) : 4.084571mm

(**j**)

Figure 3.18 The results of the calculation of the pins' migration. (a) to (j) are the point clouds of pins transformed to the same coordinate system for each of the 10 cases, respectively. The white point cloud is generated based on the postoperative CT images. The red point cloud is transformed form the point cloud generated based on the CT images scanned after one year.

Table 3.5 Result of relative angles and movement of the pins.

Case No.	Proximal Pin			Distal Pin		
	Relative Angle (°)	Top Movement (mm)	Bottom Movement (mm)	Relative Angle (°)	Top Movement (mm)	Bottom Movement (mm)
1	0.93	3.90	5.80	1.69	5.27	5.22
2	1.19	8.48	6.31	0.94	8.35	7.48
3	1.08	1.13	0.89	1.38	1.85	1.04
4	1.85	12.57	9.57	1.96	10.72	11.10
5	11.26	21.39	17.39	3.19	19.07	16.96
6	3.02	2.58	2.21	2.51	3.01	3.10
7	9.00	13.05	9.78	7.58	12.58	9.94
8	2.79	3.79	2.98	2.16	3.37	1.38
9	2.61	4.36	4.42	4.39	7.32	4.67
10	5.17	5.52	3.32	5.45	7.29	4.08

Table 3.6 shows the displacement of the Hansson pin in each direction in the new coordinate system that is discussed in Section 2.5.3.

Table 3.6 Displacement of the Hansson pins.

Case No.	Endpoint	Movement of Proximal Pin (mm)			Movement of Distal Pin (mm)		
		x-Axis	y-Axis	z-Axis	x-Axis	y-Axis	z-Axis
1	top	2.07	0.20	−3.39	0.03	−2.68	−4.61
	bottom	0.73	0.33	−5.85	−0.40	−0.02	−5.27
2	top	0.02	0.57	−8.67	0.58	−1.07	−8.47
	bottom	1.02	−0.91	−6.32	−0.39	0.19	−7.64

3	top	−0.02	−1.10	−0.31	1.67	−0.03	−0.85
	bottom	−0.56	0.33	−0.62	−0.61	0.40	−0.75
4	top	−2.66	−0.98	−12.63	−2.15	−0.68	−10.89
	bottom	0.03	0.23	−9.85	1.37	−1.18	−11.37
5	top	8.55	−6.27	−19.36	−1.35	−3.43	−18.95
	bottom	−4.08	3.57	−17.12	0.69	1.15	−17.12
6	top	1.18	2.27	−0.59	−2.44	0.27	−1.84
	bottom	−1.45	−0.8	−1.52	1.46	−0.8	−2.69
7	top	−6.15	−6.38	−9.76	7.15	−4.76	−9.26
	bottom	1.11	4.9	−8.51	−5.43	−0.61	−8.35
8	top	1.23	1.76	−3.18	−1.96	1.37	−2.46
	bottom	−1.86	−1.02	−2.15	0.33	−1.16	−0.71
9	top	−0.93	−1.66	−4.03	5.06	−1.89	−5.16
	bottom	−0.44	2.04	−4.01	−1.72	−0.12	−4.45
10	top	−0.71	4.73	−2.96	−5.82	−0.11	−4.45
	bottom	−0.63	−2.59	−2.08	2.72	−0.12	−3.07

3.4.2 Results of Evaluation

In this chapter, we defined the corresponding points in the post-alignment point cloud and the reference point cloud with distances less than 0.5 mm as coincident points, indicated by blue dots in Figure 3.17. The average and maximum distances of the corresponding points in all experimental cases are listed in Table 3.7. Besides, the proportion of corresponding points at a distance of less than 2 mm and the percentage of overlapping points were used to evaluate the degree of overlap between the two point clouds.

Table 3.7 Evaluation results.

Case No.	Iteration (s)	The Average Distance (mm)	The Max Distance (mm)	Points Whose Distance Is Less Than 0.5 mm	Points Whose Distance Is Less Than 2 mm
1	125	0.91	11.87	44.30%	93.77%
2	125	0.92	11.54	49.12%	90.33%

3	125	0.57	4.16	57.19%	97.44%
4	125	1.15	7.79	28.71%	85.33%
5	125	1.02	7.68	37.45%	87.64%
6	125	0.86	4.14	33.45%	94.19%
7	125	1.44	8.01	20.15%	81.17%
8	125	1.02	7.18	38.33%	88.36%
9	125	1.10	5.87	31.82%	85.71%
10	125	0.96	5.67	33.39%	90.80%

Table 3.8 shows that in the first case, the coordinates of the Hansson pins' endpoints and the pins' length calculated using these coordinates were measured for the same patient at two different times using the conventional method. The results show that the length of pins computed using this method had an error between 0.6 mm and 1 mm, which proves that the error of the method proposed in this chapter is limited.

Table 3.8 Results measured by traditional methods.

Pin		Coordinates After the Operation				Coordinates After One-Year Recovery			
		x	y	z	Length (mm)	x	y	z	Length (mm)
Proximal	top point	21.4	−26.7	58	80.04	21.1	−19.5	57.5	81.34
	endpoint	−16.2	17.6	2.96		−18.3	19.5	−2.02	
Distal	top point	30.1	−36.7	47.7	90.03	30.1	−30.3	46.5	91.98
	end point	−14.3	12.1	−14		−15.9	16.3	−18.1	

Table 3.9 compares the results obtained using the conventional method, the method proposed in this chapter, and the manual measurement in the first case. Compared with the traditional method, our method has a clear advantage and improvement in the measurement results' accuracy.

Table 3.9 Comparison results.

Pin	Endpoint	Traditional Method	Our Method

		Manual Measurement (mm)	Displacement (mm)	Relative Error	Displacement (mm)	Relative Error
Proximal	top point	3.30	7.22	118.79%	3.90	18.21%
	bottom point	4.56	5.73	25.66%	5.80	27.11%
Distal	top point	4.92	6.51	32.32%	5.27	7.09%
	bottom point	4.48	6.08	35.71%	5.22	16.62%

Figure 3.19 illustrates the comparison of the results' absolute error values using the conventional method and our method. Where Figure 3.19 a,b shows the displacement of the top and bottom endpoints of the proximal pin, and Figure 3.19c,d shows a comparison of the distal pin measurements.

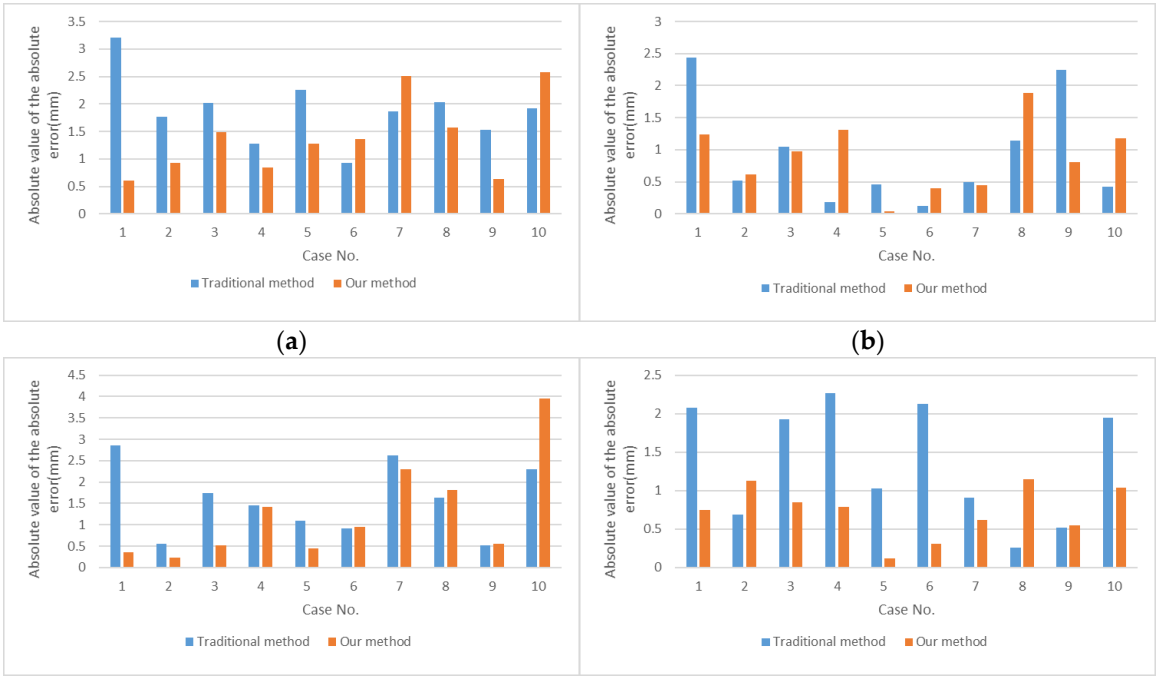

Figure 3.19 Comparison of the absolute value of the absolute error of the results obtained using the traditional method and the method proposed in this chapter: (a) Comparison of top endpoint displacement results on the proximal pin. (b) Comparison of bottom endpoint displacement results on the proximal pin. (c) Comparison of top endpoint displacement results on the distal pin. (d) Comparison of bottom endpoint displacement results on the distal pin.

3.5 Discussion

The incidence of proximal femoral fractures has increased significantly with the population's aging, which has occurred far more among women than men [24]. The preferred treatment for stable femoral neck fractures is internal fixation, where pins or screws are the main components use for internal fixation [25]. Implant stability is critical to the success of internal fixation procedures and femoral healing. Traditional methods of evaluating implant stability mainly use biological simulation and finite element analysis, which have limitations and cannot comprehensively evaluate the stability of implants. CT medical images can provide displacement data of the

implant inside the patient's body and can most directly evaluate the stability of the implant under real force conditions. However, the current clinical practice mainly relies on the manual measurement of displacement data by surgeons, which imposes a significant workload on surgeons, and the accuracy of the measurement results is highly dependent on the experience of surveyors. In this research, we propose a method to measure implants' movement after internal fixation for patients suffering proximal femur fractures, and this method is based on 3D point cloud registration.

In Reference [22], Schopper, Clemens, et al. evaluated two internal fixation systems by simulating the pelvis's pressure on the femur during human gait and measured the force and displacement of the implants in the frontal and sagittal planes. In another study, the authors used finite element models to implement biomechanical simulations of five different configurations of internal fixation implants [23]. In both studies, only the pelvis's pressure on the femur was simulated during the standing phase of the patient's gait, ignoring the interaction forces of the muscles and other organs. More critically, they did not study the internal fixation implants in the fixation effect throughout the patient's postoperative recovery. In daily life, patients spend most of their time sleeping and sitting, which can have a cumulative effect on the implant position and its stability. The method proposed in this chapter directly utilizes authentic postoperative CT medical images of the patient as the basis for the study. The results in Table 3.6 show the displacement of the pins after the patient has experienced one year postoperatively. This method addresses the limitations of traditional biomechanical simulation methods in simulating the complex environment.

We found that the ICP algorithm can provide high precision in fine alignments. However, with the number of points increasing in the point cloud, the time consumed per iteration also grows. To solve a problem that requires a long time, we downsized the point cloud or removed parts of the 3D model with less feature quantity. In our experiment, we used a part of the femur for registration, and satisfactory results were obtained. According to the outcomes listed in Table 3.4, when the number of iterations was set to 125, the time used for registration increased by five milliseconds for each additional point. Therefore, we can reduce the registration time by reducing the number of model points while still meeting the registration accuracy requirements. In this study, we also found that a portion of the corresponding points in the aligned

model had a distance greater than 2 mm, and this fraction ranged from 3% to 19%. The possible reason for is that, in the process of 3D reconstruction, some non-femoral regions are identified as the femur as the threshold value is the same as the femur, resulting in some irregular points existing in the generated femur. Since these points do not belong to the femur, the corresponding points cannot be found, but the nearest points are matched, which affects the experimental results. The extraction of boundary information from point clouds and the development of point cloud filtering methods are expected to improve the experimental results.

The results in Table 3.9 demonstrate that, in the current study, the newly proposed method showed a significant improvement in the error of the measurement results compared to the method in which the surgeon establishes a coordinate system in the CT images for measurement. The conventional measurement method relies strongly on the expert's experience in establishing the coordinate system and selecting the target location, which is susceptible to subjective factors.

Another important finding based on the results listed in Table 3.6 was that the Hansson pin moved gradually downward in the femur, whose coordinate system was built and is described in Section 2.5.3. In 10 cases, all pins moved along the Hansson pin's central axis, toward the lateral aspect of the femur. For seven of the cases, the distal pins were displaced to varying degrees in the opposite direction of the hook pin extension, and the displacements of the top ends were greater than the displacements of the bottom ends, indicating that the pins also rotated to the opposite direction of the hook pin elongation during the displacement process.

In Figure 3.8e, the smoothness of the two femoral models' outer surface without the femoral head is not consistent; this is because the two 3D femoral models originated from different CT image sequences. These two sequences were scanned one year apart and used different scanning equipment and scanning parameters. The green model was derived from CT medical images after an internal fixation surgery with an image layer spacing of 3 mm. The blue model was derived from CT images after a one-year recovery period with an image layer spacing of 1.5 mm. While cutting the 3D model, the images with a large layer spacing produced significant faults at the incision, which did not affect the reference registration.

The major limitation of this study is that we used the built-in threshold tool of a 3D Slicer to implement the automatic 3D reconstruction of CT medical images. The reconstructed 3D model contained the whole femur and the connected part of the pelvis, which needed to be artificially segmented in order to obtain the alignment object, as shown in Figure 3.4. In addition, it was necessary to manually remove the interfering points generated during the 3D reconstruction process to avoid the influence of these interfering points on the registration results. The average time required to manually remove the interference points and segment the alignment object was 120 s. The time required to measure the implant displacement depended on the number of sampling points of the alignment object and can be controlled to be less than 200 s. The total time required to complete an implant displacement was approximately 270 s. Since the preprocessing of the 3D point cloud data in this study was independent of the displacement calculation stage, the automatic segmentation of the reference part could also be achieved by other methods in future studies to reduce the time consumption. In addition, the purpose of this study was to verify the effectiveness of the proposed method, therefore there was no optimization in our study for the registration time. The main time of the displacement calculation stage was spent on the alignment of the reference 3D point cloud, and we could reduce the time consumption by decreasing the number of sampling points.

3.6 Conclusions

In this investigation, the aim was to present a method based on point cloud matching for evaluating the stability of internal fixation implants in femur fractures during patient recovery. This method was based on the Hansson pins analysis and is widely applicable to the analysis of other implants used for fixation. We reconstructed the femur and implant using CT images of patients at different times after internal fixation surgery. A portion of the femur with no femoral head was selected as a reference, and the pin-point clouds from different periods were converted to the same coordinate system to calculate the endpoint displacement of the corresponding pin. Meanwhile, a new coordinate system based on the pin axis and extension direction of the hook pin was used to evaluate the Hansson pin as a feature.

Since the same initial orientation was chosen for the same set of data in the 3D reconstruction model, the femur's rough alignment was avoided, which reduced the alignment time and improved the accuracy. Furthermore, the measurement error in our study was limited, and the method yielded satisfactory results.

Chapter 4
Implant evaluation method based on femur intelligent segmentation and multi-resolution frame registration

4.1 Introduction

Femoral neck fractures (FNFs) constitute a common surgical trauma worldwide, with a patient population of 1.6 million per year and growing annually [51]. Aging people have a high incidence of femoral neck fractures due to their tendency to low-energy fall and high prevalence of osteoporosis prevalence [52]. Previous epidemiological studies have indicated that the incidence is approximately twice as high in females as in males [53]. Particularly with the aging of the population in all countries, the prevalence of femoral neck fractures increases over the years, accompanied by high mortality and disability rates [54]. It is expected that by 2050, the number of patients with FNFs will exceed 6 million worldwide [55], which will account for a significant proportion of orthopedic work and constitute a health care burden significant in terms of socio-economic impact.

Plastic surgery literature now agrees that cannulated screws and the dynamic hip screw (DHS) are the most commonly used treatment modalities for stable fractures classified as Garden I or II [56]. The internal fixation is minimally invasive compared to total hip arthroplasty (THA) and can significantly reduce the postoperative hospital stay [57] –[58]. Nevertheless, the use of internal fixation hip implants is associated with medium to long-term surgical complications such as chondrolysis, osteonecrosis, avascular necrosis, and mechanical failure of the implant, accompanied by a high rate of rehospitalization and reoperation [59]–[61].

Much literature has been presented to analyze and study internal fixation results with hip implants. Marco Bigoni et al. analyzed postoperative patient mortality, complications, and reoperation rates statistically by following 244 elderly patients

who underwent internal fixation with implants over 10 years from January 2008 to December 2018 [62]. The results indicate that internal fixation effectively stabilizes femoral neck fractures, and the patient's postoperative mortality and complication rates are only associated with individual patient comorbidities. Ref. [63] has conducted mechanical simulations of implants for the treatment of stable femoral neck fractures using synthetic bones. That study evaluated hip implants' ability with different configurations by limiting relative motion at the fracture site using a manual hydraulic press to simulate hip compression, i.e., to measure the amount of resistance of the pins. In the experimental part, the femur's stability was compared between two internal fixation systems by simulating force by the spine to the femur, with one of the internal fixation systems using two parallel cannulated screws and the other framework using three cannulated screws forming a pyramidal shape. In [64], the authors modeled the fracture with segmented human cadaveric femora. Using the servo-hydraulic device to simulate the force components in the frontal and sagittal planes in human gait motion, they measured the displacement of both internal fixation systems at different loads. Moreover, Jiantao Li et al. proposed a method analyzing five different implant configurations using a finite element approach [65]. They evaluated the mechanical properties such as stress and strain in different postoperative weight-bearing states of patients by computer simulation. In contrast, ref. [66] analyzed the stresses applied to the femur and related tissues under different fracture types after internal fixation of femoral neck fractures from a biomechanical perspective. It assessed the mechanical stability of mainstream fixation techniques such as cannulated screws, hip screw systems, proximal femur plates, and cephallomedullary nails.

Among these evaluation methods, the use of statistics to evaluate treatment effectiveness cannot provide specific reasons for pins' failure and requires a large number of experimental samples as a basis for analysis. Mechanical simulations using synthetic bones, cadaveric femora, and finite element-based 3D models all use a simulated stress environment. Obviously, the simulated environment is different from the patient's real behavioral movement after surgery and can only use a limited number of parameters and simulated stresses in a single scenario. What is more, it takes months or years of data collection to assess the effectiveness of internal fixation on patients accurately, which is very difficult for mechanical simulation experiments.

Computed tomography scans provide realistic information about the displacement of implants in the patient's body after surgery. The acquisition of computerized tomography (CT) scan does not place an additional load on the patient's daily movements. Traditionally, however, the measurement of fracture displacement or implant displacement in the body is mainly performed by the surgeon in CT medical images, selecting a reference, measuring the target object's distance relative to the reference in different CT sequences, and calculating the displacement. In [67], the authors acquired two sets of chest computed tomography scans, CT1 and CT2, at an interval of 84 days. The distance of the rib's outer cortex was measured in three planes, using the site of the rib fracture as a reference point to verify that rib fractures become more displaced over time. A similar approach was used by Bugaev and Nikolay et al. to measure axial displacement, sagittal displacement, and coronal displacement, and then they calculated the (Euclidean) distance using the Pythagorean formula [68]. In the literature [69], digital calipers and a protractor were used to measure foot fractures within the CT images' coronal plane. This manual method of measuring implant displacement is complex and time-consuming to perform, and the accuracy of the measurement results is susceptible to subjective influence by the surgeon.

This chapter presents a method for evaluating internal fixation implants based on CT medical image analysis. The Hansson pins system is used as the study object to quantify the implant's movement after surgery and to analyze the effectiveness of the internal fixation system. Our method allows us to analyze the movement of the implant in a specific direction with low impact on the patient, based on real patient data.

4.2 Materials and Methods

4.2.1 Creation of Data Sets

In this chapter, we constructed Dataset A and B for training the segmentation models of the left and right femur, respectively, and Dataset C for femur registration and displacement measurement of the implant. In the segmentation femur stage, this chapter uses 3D-UNet, a semantic segmentation framework, which differs from the instance segmentation framework; 3D-UNet can only classify pixels in an image. In

our study, if the dataset used for training does not partition anatomically left and right, the trained model will also label the healthy femur that is symmetrical with the injured femur as the target object. While in Section 2.2, the mask required for fine registration is only the femur that is fixed with the implant. To avoid registration failure, we construct the left femur and right femur datasets separately and train two segmentation models for the left and right femurs.

4.2.1.1 Dataset A and B

High-quality medical image collection is challenging due to the need to protect patient privacy and data security. Additionally, the annotation of images requires a large number of experienced surgeons; therefore, it is quite costly to integrate high-quality annotated data, limiting the development of medical image segmentation algorithms, which has become an accepted fact in the field of medical image research [70]. Consequently, no publicly available medical image datasets specifically for femoral fractures are available. However, some of the images in the dataset that are currently publicly available for other research purposes contain the femur we need. In these raw CT images, in addition to containing the entire left and right femur, adjacent tissues and organs such as the pelvis, spine, and ribs are also included. Which can considerably increase the GPU's memory usage, making it necessary for us to extract regions of interest (ROIs), i.e., image information that contains only femur parts. Furthermore, we need to label the femur information as ground truth for training manually.

We used Pelvic Reference Data, a free dataset used for commercial, scientific, and educational purposes, as the original data [71] –[72]. This dataset was created to serve as a reference for the rigid registration of clinical images. The process of removing irrelevant information from CT images is shown in Figure 4.1.

Figure 4.2 displays the coronal images viewed from the anterior side. The complete image (b) is shared between the two datasets, and as a complement, each of the two datasets also contains unique left femur (a) and right femur (c). In this way, we can simply expand the dataset and accurately distinguish between left and right femur when segmenting CT images that contain a complete structure. By removing the data with poor image quality, in Dataset A, we ended up with 112 images of the left femur, of which 84 images were used for training, and 28 images formed the

validation set. Similarly, 113 images were collected in Dataset B. A total of 85 images were used for training, and 28 images were used for validation. Subsequently, manual annotation of the femur for the constructed dataset.

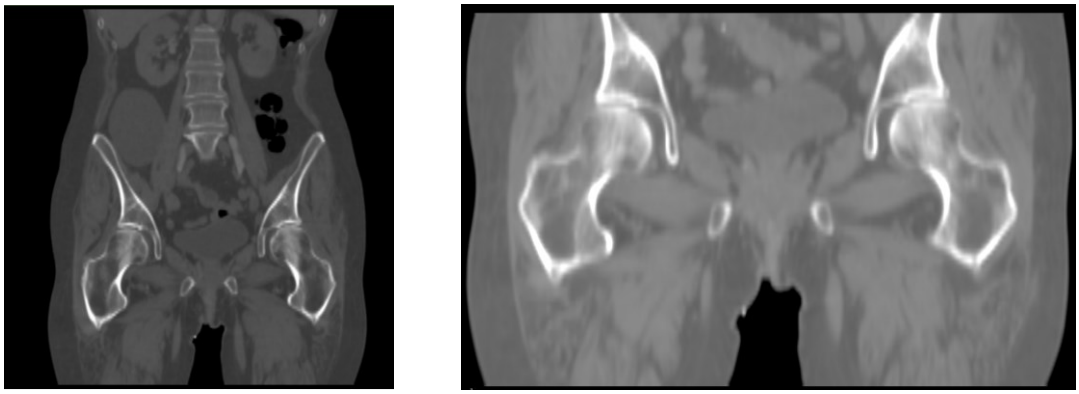

(a) (b)

Figure 4.1 Cropping of CT images: (a) raw CT data in Pelvic Reference Data, including symmetrical femur, pelvis, spine, etcetera; (b) cropped CT images.

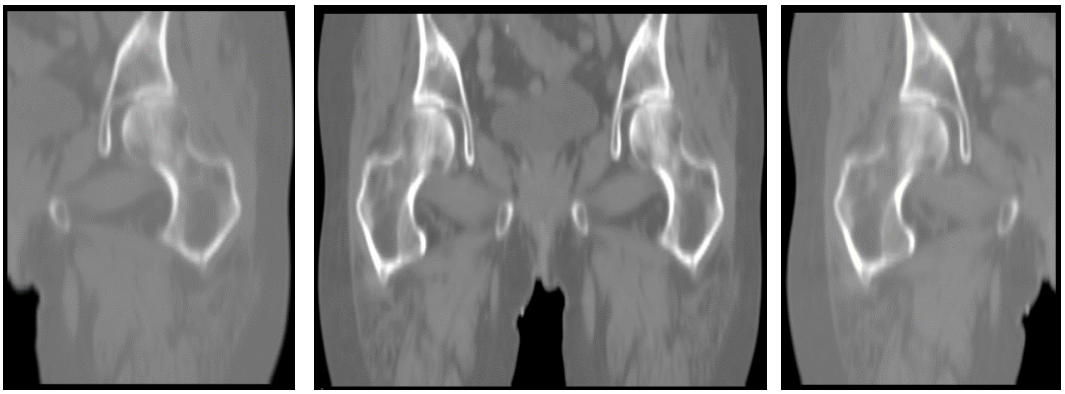

(**a**) (**b**) (**c**)

Figure 4.2 Coronal images viewed from the anterior side: (a) left femur; (b) images shared by both datasets; (c) right femur.

4.2.1.2 Dataset C

In Dataset C, we collected 10 cases from March 2012 to January 2015 provided by Hyogo Prefectural Awaji Medical Center. Each case underwent two CT scans after internal fixation surgery and one year later.

All cases associated with intracapsular fractures and the patient's age ranged from 69 to 65 years. These cases all used the Hansson Pin System (Hansson Pins, Swemac, Linköping, Sweden) [73]. Hansson pin is a 6.5-diameter unthreaded nail with various specifications and the length ranging from 75 to 150 mm. The implant has an

integrated hook on each pin's tip that deploys to provide rotational stability of the femoral head following insertion. Typically, using two pins for fixing and screwing out the hook pins when fixing (Figure 4.3). Table 4.1 lists information such as the patient's age and the pins used.

Table 4.1 The length of pins and information of patients in each case.

Case No.	Length of Pins (mm)		Sex	Age	Location of Fracture
	Proximal	Distal			
1	80	90	Female	78	Left femur
2	80	90	Female	79	Left femur
3	70	85	Female	90	Left femur
4	80	90	Female	65	Left femur
5	85	95	Female	76	Left femur
6	90	100	Female	64	Right femur
7	80	95	Female	81	Right femur
8	80	90	Female	80	Right femur
9	80	90	Female	67	Right femur
10	75	90	Female	85	Right femur

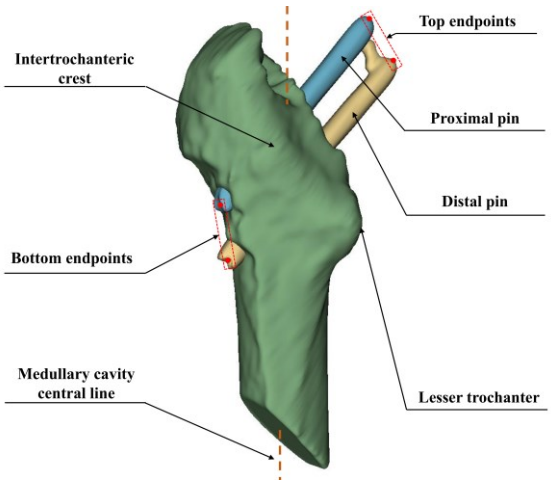

Figure 4.3 The position of Hansson pins in the anatomy of the femur.

Figure 4.4 illustrates the different situations during a CT scan. Generally, in the examination during the recovery period from surgery, the CT data is cropped and transformed to provide a clearer and faster diagnosis, that is, a localized CT image of the left or right femur. In contrast, the complete femur and pelvis are sometimes retained in the CT image to visualize information around the fracture site. To obtain high robustness of the trained femur segmentation model and avoid the femur segmentation failure in the next step, we convert all images to the right, anterior, superior (RAS) anatomical coordinate system and use empty images to supplement the missing parts.

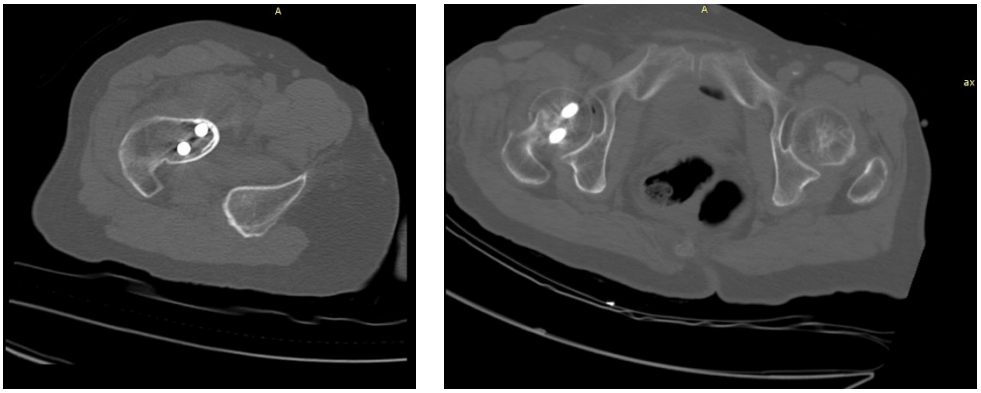

(**a**) (**b**)

Figure 4.4 The partial CT image versus the complete CT images: (a) partial CT images containing a single femur; (b) CT images containing the complete femur structure.

4.2.2 Registration of the Femur

For measuring the postoperative displacement of the Hansson pins, it is necessary to select a reference with rigid morphological properties. Depending on the setting in which the Hansson pin is used, the shape and X-ray absorptivity of the proximal femur does not change unless structural damage occurs, which satisfies the requirements for use as a reference. Femur image registration is the transfer of images containing femur and implants from the same patient at different times, different scanning devices, different scenes, and others to the same spatial coordinate system and strict alignment with femur as the reference. After this transformation, it is possible to measure the position information of Hansson pins at different times.

Typically for CT image alignment, at least two sets of images containing the same target information are required. The matching criterion is to achieve maximum similarity between the fixed and floating images, a combination of feature space matching algorithm, spatial search algorithm, optimization algorithm, and similarity measure. Commonly used rigid medical image registration algorithms include point set matching based, a genetic algorithm-based, and mutual information-based 3D image registration. The alignment of the femur image in this chapter is rigid, i.e., no affine transformation of the graph is required, which requires high alignment accuracy.

We choose a multi-resolution framework, which uses negative mutual information as the similarity metric function. The framework contains four parts: spatial

transformation module, similarity metric module, interpolator, and optimizer, as shown in Figure 4.5.

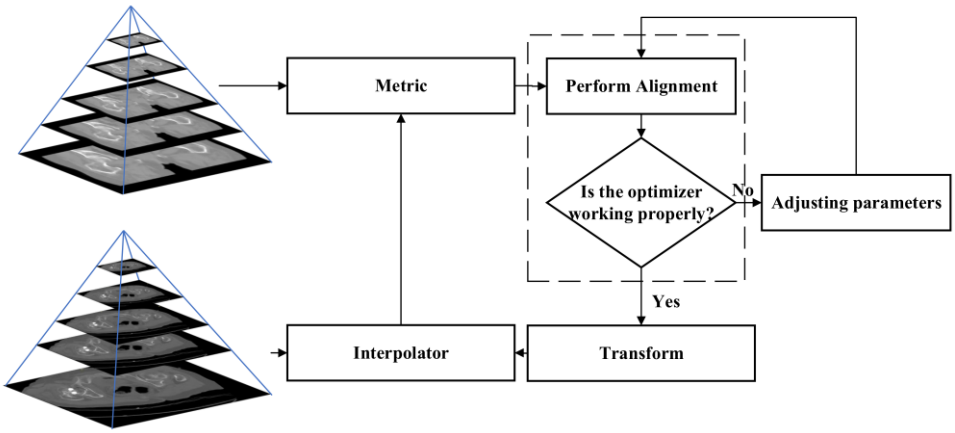

Figure 4.5 Pyramid multi-resolution framework.

This framework is widely used in medical image registration due to its high accuracy, robustness, and fast alignment speed. Its core idea is to input the images in the fixed image pyramid and floating image pyramid into the framework layer by layer. An optimizer is used to drive the alignment process, and an interpolator is used to map the floating images into the new coordinate system [74]-[75].

The method of negative mutual information in the similarity measurement module was proposed by Mattes et al. in 2003. Mutual information forms a continuous histogram estimate of the underlying grayscale image using the Parzen window virtually eliminates the effect on the similarity calculation due to interpolation quantization and binary data discretization during the image space transformation. Image registration can be seen essentially as the process of minimizing the negative similarity function. When we define the set of discrete grayscales for a fixed image as S_F and the set of discrete grayscales for a floating image as S_R, the negative similarity function model can be expressed as

$$S(\mu) = -\sum_{l \in S_F} \sum_{\kappa \in S_R} \frac{p(l,\kappa;\mu)\log_2(p(l,\kappa;\mu))}{p_F(l;\mu)p_R(\kappa)}. \tag{4.1}$$

where $p(l,\kappa;\mu)$ is the joint distribution function, which can be calculated from the values of the Parzen window cubic spline and zero-order B-splines. l,κ are the grayscale values in S_F and S_R, respectively. p_F is the floating image edge probability

distribution and p_R is the fixed image edge probability distribution. μ is the image transformation parameter.

Mattes mutual information function has continuously differentiable characteristics. The optimizer needs to meet the conditions of high speed, low resource consumption, and high robustness to obtain the optimal spatial transformation parameters. Therefore, we choose a multi-resolution algorithm as the optimization search strategy. In this section, we select the patient's CT images before the one-year recovery period as fixed images and the CT data after the one-year recovery period as floating images to construct the Gaussian pyramid. Gaussian pyramids are constructed using Gaussian smoothing and downsampling to create a series of images of varying sizes. These images form a pyramid model from large to small and from bottom to top, as the fixed image and floating image modules present in Figure 4.5.

We take the original fixed image and floating image as the bottom level 0 of the pyramid, and after the discrete low-pass filter calculation, an upper level 1 of the upper pyramid is obtained, and the iterative process is repeated. For getting the Gaussian pyramid layer G_i, it is necessary to perform Gaussian low-pass filtering on its previous level image and then downsample it by inter-row and inter-column, usually for removing pixels in even rows and even columns of the image. The mathematical expression is

$$G_l(i,j) = \sum_{m=-2}^{2} \sum_{n=-2}^{2} \omega(m,n) G_{l-1}(2i+m, 2j+n) \quad (1 \le l \le N, 0 \le i \le R_l, 0 \le j \le C_l) \tag{4.2}$$

where N is the number of Gaussian pyramid layers, R_l and C_l are the number of rows and columns of the image of the ith layer of the Gaussian pyramid, respectively; $\omega(m,n)$ is a two-dimensional 5 × 5 window function with the expression as

$$\omega = \frac{1}{256}\begin{pmatrix} 1 & 4 & 6 & 4 & 1 \\ 4 & 16 & 24 & 16 & 4 \\ 6 & 24 & 36 & 24 & 6 \\ 4 & 16 & 24 & 16 & 4 \\ 1 & 4 & 6 & 4 & 1 \end{pmatrix}. \tag{4.3}$$

When two 3D images containing femur are input to the framework, the registration range defaults to the whole image, and the optimal spatial transformation parameters obtained after iteration corresponds to the global search space. In other words,

although the spatially transformed floating image matches the fixed image, the purpose of our study is to align the femur. The tissues or organs around the pelvis, such as the pelvic bone, will significantly affect the similarity calculation. In this case, the spatial transformation mostly matches the pelvis's position rather than the proximal femur. Therefore, we use the above framework to perform coarse alignment on the images containing the femur. After that, we use the femur's mask and perform fine registration on the region containing the only femur.

4.2.3 3D-UNet Framework

To extract the region of interest, we segmented the proximal femur without the femoral head in the patient's CT images using a model trained by the 3D-UNet framework.

3D-UNet is an end-to-end training model proposed by Özgün Çiçek et al., which is mainly used for semantic segmentation of medical images [76]. The model inherits the features of the 2D-UNet network by using encoder and decoder structures to extract features and recover the semantic feature maps into volumetric images with the same resolution as the original images. Compared with the 2D-UNet network, 3D-UNet uses the image interlayer information to ensure the continuity of mask changes in adjacent images. Moreover, different from the fully convolutional network, which only deconvolutes the feature map, 3D-UNet achieves the multi-scale feature recognition of image features by the symmetric structure of four downsampling and four upsampling, and the skip connection method, i.e., it fuses the shallow features of the same scale in the encoder and the in-depth features from the upsampling to avoid the loss of edge information. The downsampled low-resolution information provides contextual information to the target, and the upsampled high-resolution features improve the network's ability to recognize edge information such as gradients. Figure 4.6 illustrates the 3D UNet network framework used in this chapter. In the encoder structure, we set the network structure to 5 layers, and the number of channels in each layer is 16, 32, 64, 128, and 256, respectively.

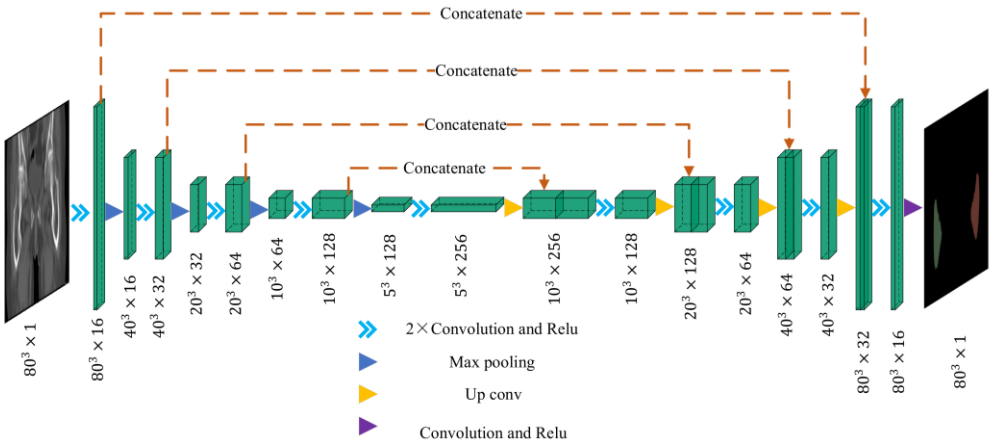

Figure 4.6 The framework of a symmetrical structure of a five-layer network with 1 channel for both input and output and a volume of 80 × 80 × 80.

This study uses dice loss as the loss function, which is widely used in neural networks for medical image segmentation. Dice score coefficient (DSC) is used to evaluate the degree of overlap of two samples, and in binary semantic segmentation, the segmentation effect is evaluated based on ground truth [77]. Hence, we can maximize the overlap of two samples using $1 - \mathrm{DSC}$. Dice loss was first proposed and used in the VNet framework by Milletari et al. and is defined as

$$L_{dice} = 1 - \frac{2\sum_{i=1}^{N} p_i g_i}{\sum_{i}^{N} p_i^2 + \sum_{i=1}^{N} g_i^2} \tag{4.4}$$

where p_i and g_i represent the predicted label and ground truth of each voxel, respectively, during the training process. N is the number of voxels in the input image.

CT images vary depending on patient condition and scanner model. The output segmented femur is often accompanied by segmentation noise, as shown in Figure 4.7. The noise appears as small, separated coherent voxels. The model outputs segmented images in which the femur has the largest number of coherent voxels. To correct this problem of non-femur parts being incorrectly identified, we retain only the largest coherent components in the post-processing of the model output. The mathematical model can be expressed as

$$V_{opt} = \mathrm{argmax}(F(v)). \tag{4.5}$$

where $F(v)$ is a function to calculate the maximum number of contiguous adjacent voxels.

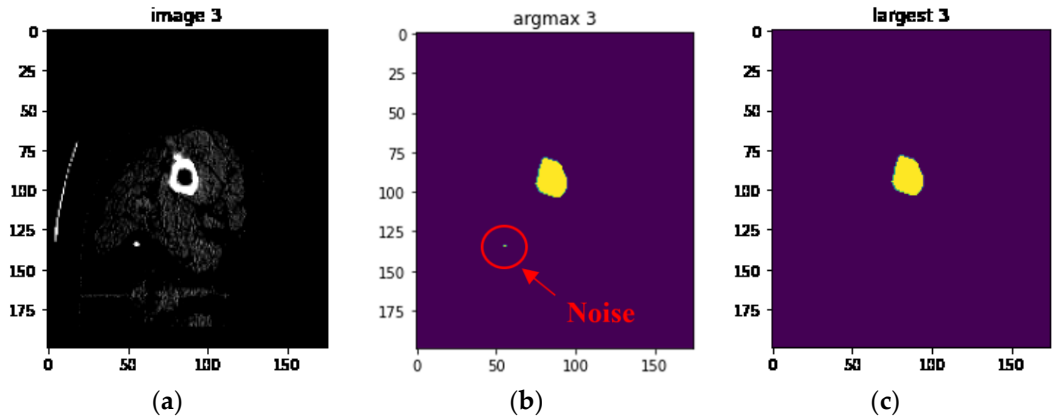

Figure 4.7 In post-processing, remove noise from the image: (a) input images; (b) output image with noise; (c) output image with maximum coherence preserved.

4.2.4 Principal Component Analysis (PCA)

Based on the aligned CT images, the Hansson pins were reconstructed as a 3D model. We use the point cloud data to calculate the displacement distance after locating the endpoints of the pins. In this subsection, we apply the principal component analysis method to fit the pins' axes, as shown in Figure 4.8. The point cloud size and the obtained axes are used to draw the outer envelope of the pins, and the point intersecting the envelope in the direction of the axes is the endpoint of the pins.

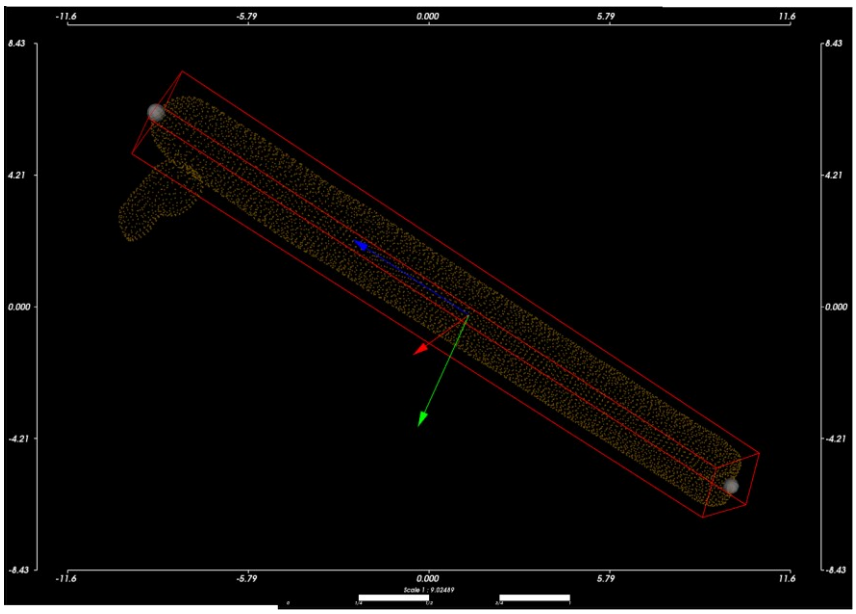

Figure 4.8 The pin's axis and the outer bounding box of the pin intersect are the two endpoints of the implant.

The principal component analysis is a multivariate statistical method commonly used for dimensionality reduction of multidimensional data [78]. The main principle is that the m-dimensional feature vector is mapped to the n-dimensional vector using the orthogonal transformation. This n-dimensional vector is an orthogonal vector constructed based on the original features, where the first vector is the direction with the most considerable variance in the original data.

The algorithm is:

Input:

- M-dimensional sample set $D = (x^{(1)}, x^{(2)}, \ldots, x^{(m)})$;
- The number of dimensions n to be dimensioned down to.

Output: reduced-dimensional sample set D'.

Steps:

1. Standardize all variables.

$$x^{(i)} = x^{(i)} - \frac{1}{m}\sum_{j=1}^{m} x^{(j)} \tag{4.6}$$

2. Calculation of covariance matrix.
3. Computes the eigenvectors and eigenvalues of the covariance matrix.
4. Select the largest n vectors normalized to form a new matrix W.
5. Transform the original matrix.

$$z^{(i)} = W^{T}x^{(i)}. \tag{4.7}$$

6. Output sample set $D' = (z^{(1)}, z^{(2)}, \ldots, xz^{(m)})$.

We define a single point in the point cloud as $P_i = < x_i, y, z_i >$. The point cloud can be represented as a sample set $D = (P_1, P_2, \ldots, P_n)$, by inputting D into the PCA algorithm above, we solve the feature vectors $(\varepsilon_1, \varepsilon_2, \varepsilon_3)$ and form the orthogonal matrix $W = [\varepsilon_1', \varepsilon_2', \varepsilon_3']$ after standard orthogonalization of each feature vector. ε_1', ε_2', and, ε_3' are the main directions of the input point cloud, and the center of mass of the point cloud is taken as the origin of the new coordinate system. Using the point cloud's center of mass as the origin of the coordinate system, ε_1', ε_2', and ε_3' as the axes to form the coordinate system shown in Figure 4.8, where ε_1' is the blue axis, ε_2', is the green axis, and ε_3' is the blue axis. The original point cloud data is converted to the new coordinate system using Equation (4.7). Subsequently, the red enclosing box is constructed according to the point cloud's maximum and minimum values in the three directions of X, Y, and Z.

4.3 Experiment

4.3.1 Input of Images and Training of Segmentation Models

In general, CT images are obtained by data transformation of scanning devices according to the different X-ray beam absorption coefficients of human organs or tissues. The coordinate system origin and voxel spacing of the generated CT images vary depending on the scanning device. The 3D-UNet framework cannot extract voxel spacing as feature information, so we resample the data in Dataset A and B to the same voxel spacing, which is called the specified spacing. To minimize the loss of image detail due to the decrease in slices caused by increasing the specified spacing, we resampled the voxel spacing to 1.5 × 1.5 × 1.5 mm.

The images' orientation may vary from case to case when the training data is input to the neural network. Here, we use the RAS coordinate system to ensure the input data orientation's consistency. In addition, to simplify the feature extraction process of the 3D-UNet network and reduce the impact of femoral edge blur on the segmentation, we remove the information beyond 20HU-220HU from the CT images and convert the intensity range of the remaining information to (0,1). The processed images and labels are illustrated in Figure 4.9.

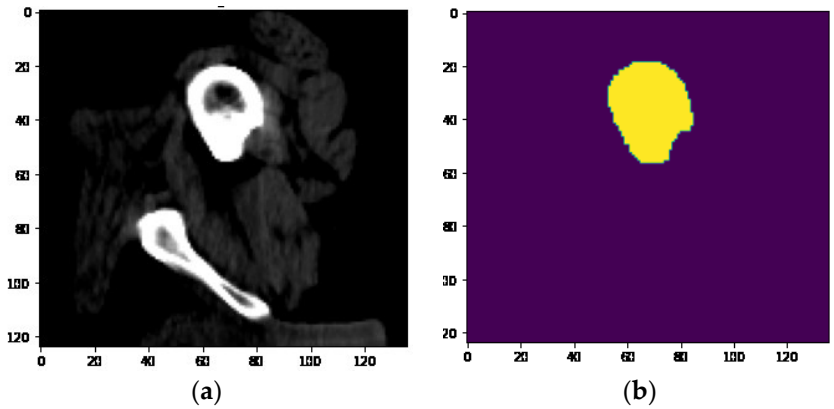

Figure 4.9 The processed images and labels.

In this chapter, the 3D-UNet network is set to five layers, so the size of each input image size should be a multiple of 16. Considering the image's size after specified spacing resampling, we use cropping to augmentation the dataset in this section, and the cropped image size is (80, 80, 80). 3D-UNet has the features of requiring less training data and good results for medical image segmentation. Published literature indicates that the 3D-UNet network can still achieve good segmentation results when

a small number of datasets are used for learning [76]. Thus, we did not use methods other than random crops for data augmentation.

The datasets A and B separately input into the 3D-UNet framework of the previous session for training. In this section, we implement the framework using MONAI, an open-source framework based on PyTorch [79]. The training yields the left femur segmentation model and the right femur segmentation model, respectively. The images in Dataset C were segmented using each of the two trained models according to the femur's left and right positions with internal fixation using Hansson pins. The segmentation information of the injured femur was collected as mask data for the next step.

4.3.2 Registration of References

The CT data acquired postoperatively as fixed images, and the CT data scanned one year later as floating images were simultaneously inputted into the mutual information registration framework in the previous section for coarse alignment. The coarse alignment result is used as input, and the femur segmentation data from the previous step is used as masks for fine alignment of the images. To avoid the influence of mask edge information on the alignment, we use a kernel of size ($27 \times 27 \times 27$) to perform morphological collision processing on the mask.

To verify that segmenting femur by the model can provide an accurate mask for fine alignment, we add an experiment to manually labeled femur as the mask for fine alignment and compare the effect of both masks on fine registration.

The fixed image and floating image after fine registration are shown in Figure 4.10. In the two CT images after alignment, the proximal femur parts without the femoral head are overlapped and served as the reference. Observed in 3D space, the proximal pin and distal pin are in the same spatial coordinate system, and after 3D reconstruction, the voxel data of pins in CT are transformed into point cloud data, as shown in Figure 4.11.

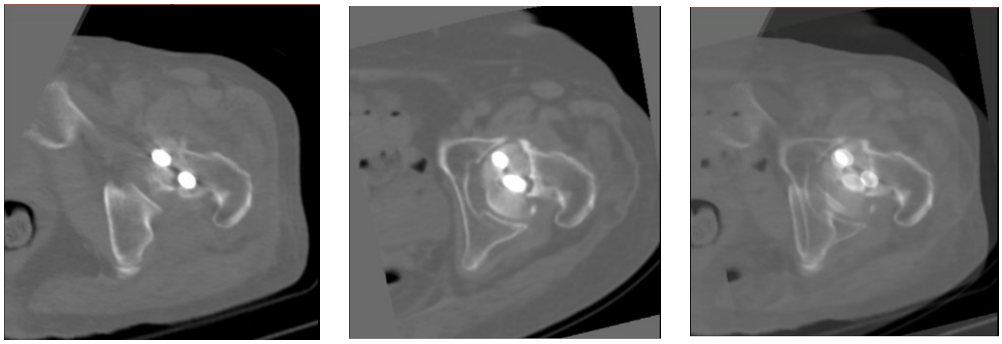

(a) (b) (c)

Figure 4.10 CT images after registration: (a) fixed images; (b) fine-aligned floating images; (c) the two images in the coordinate system with the overlapping femur as the reference.

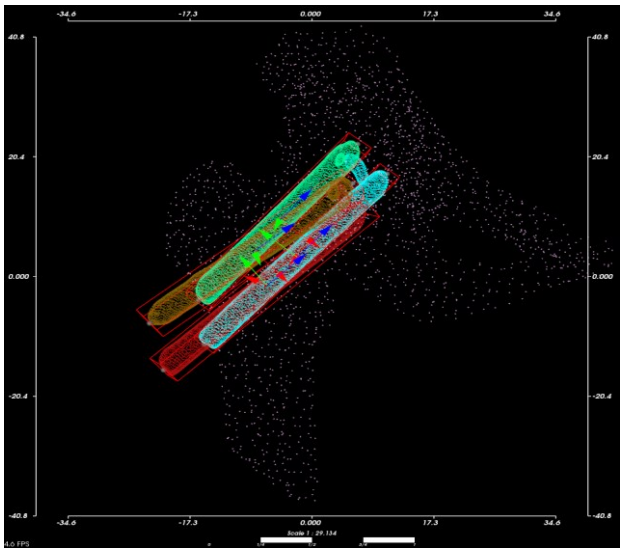

Figure 4.11 3D point clouds of proximal pins and distal pins in the same spatial coordinate system for both previous and posterior CT images. The purple point cloud is part of the proximal femur and pelvis. The green and blue point clouds represent the proximal and distal pins obtained from the first postoperative CT scan. Gold and red point clouds represent the proximal and distal pins from the second CT image after the previous CT scan, respectively.

4.3.3 Calculation of Implant Displacement

Using principal component analysis, we built the pins' outer bounding box, obtained the coordinates of the endpoints of the four pins in Figure 4.11 separately, and calculated the displacement of the corresponding points. To analyze the displacement of Hansson pins more comprehensively, we take the axis of pins as the z axis, the direction of hook extension as y axis, and the direction of the cross product of y and z as x axis to establish a new coordinate system, as shown in Figure 4.12 a,b are the proximal pin and distal pin coordinate systems, respectively. In the new

coordinate system, the proximal pin and distal pin's displacements in different directions are calculated.

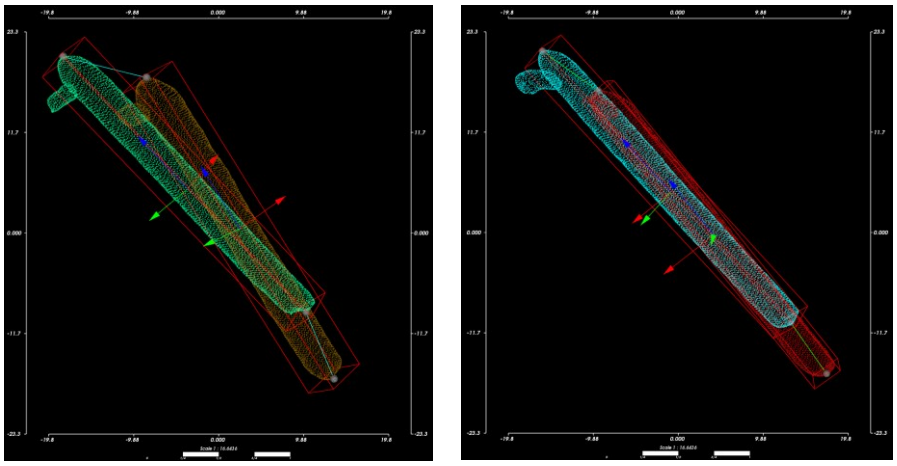

(a) (b)

Figure 4.12 Calculate the displacement of the proximal pin and the distal pin in the specified direction in the newly established spatial coordinate system: (a) establish the coordinate system based on the proximal pin; (b) establish the coordinate system based on the distal pin.

4.3.4 Measurement of Implant Displacement Based on Conventional Methods

In this subsection, to verify our proposed measurement of implant displacement's validity, we used the reference point-based distance measurement method described in [68]. We define the point on the outer surface of the Lesser trochanter farthest from the centerline of the medullary cavity as reference point A. As shown in Figure 4.13a–c, all steps to locate point A were performed entirely using the three planes in the CT images, and no 3D femur model was used to assist in localization. Figure 4.13d is used to assist in showing the position of the reference point in the CT image.

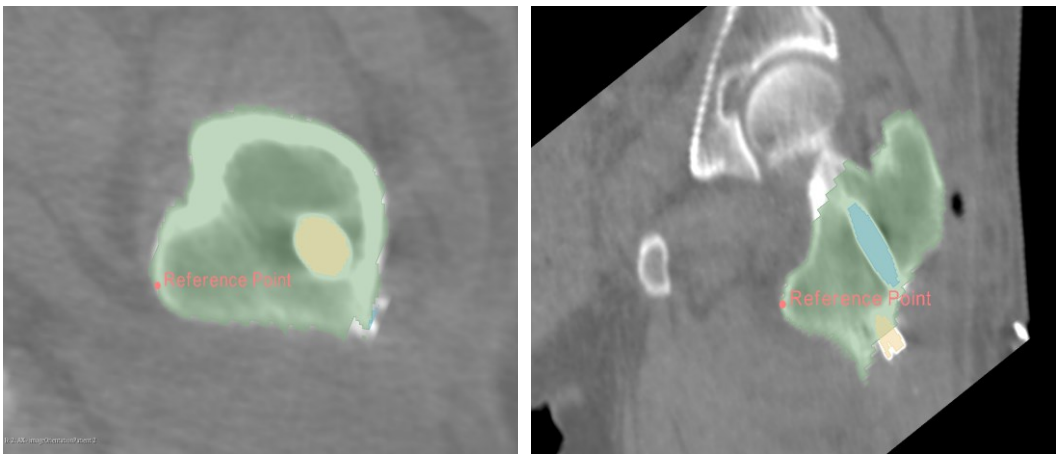

(a) (b)

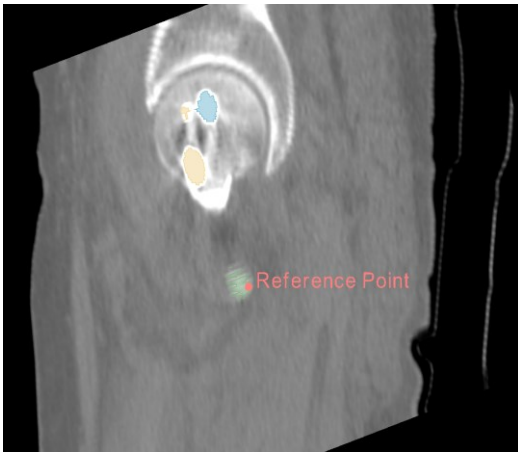

(**c**)

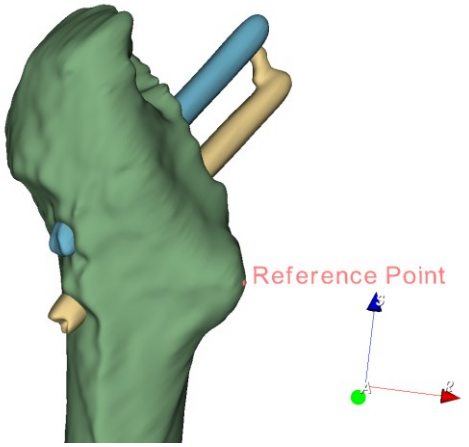

(**d**)

Figure 4.13 Locating reference point A in the CT image: (a) reference point located in the axial plane; (b) reference point located in the sagittal plane; (c) reference point located in coronal plane; (d) display reference point in the 3D model.

Point A is used as the origin, and a new coordinate system is formed with the intersecting lines of the planes, axial plane (green), coronal plane (blue), and sagittal plane (red), as shown in Figure 4.14. The coordinates of the target object are measured in the new coordinate system, and the Euclidean distance is calculated using the formula

$$d = \sqrt{(x_1 - x_2)^2 + (y_1 - y_2)^2 + (z_1 - z_2)^2} \ . \tag{4.8}$$

where (x_1, y_1, z_1) and (x_2, y_2, z_2) represent the coordinates of the same point in the two CT image sequences, respectively.

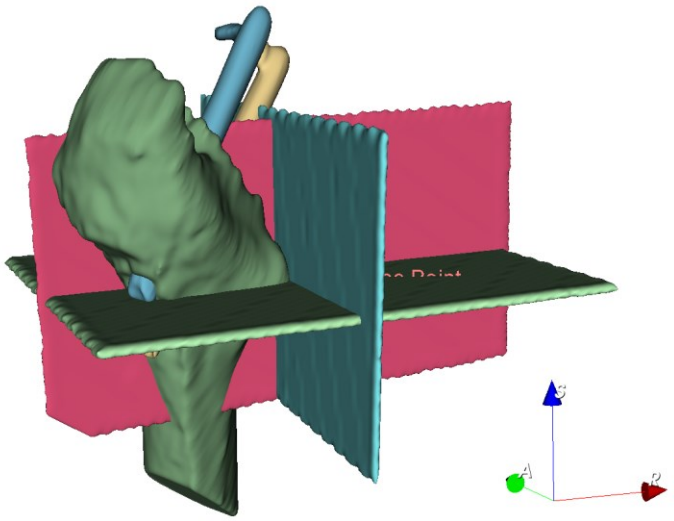

Figure 4.14 Create coordinate system for measurement.

To reduce the measurement error, we measure the coordinates of each point three times and take the average value to plug into Equation (4.8).

4.4 Results

4.4.1 Training Loss, Mean Dice, and Evaluation

Datasets A and B are used to train the left femur segmentation model, and the right femur segmentation model is derived from the same data source with the same image quality. The proportions of the images used for training and validation are also the same. The results of loss and the change of mean dice during the two models' training are shown in Figures 4.15 and 4.16, respectively.

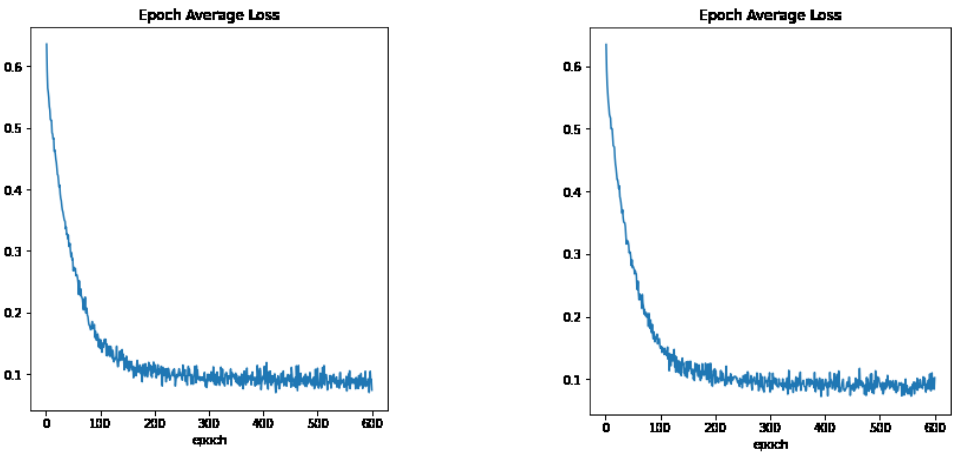

(a) (b)

Figure 4.15 The average loss calculated in training: (a) left femoral segmentation model; (b) right femoral segmentation model.

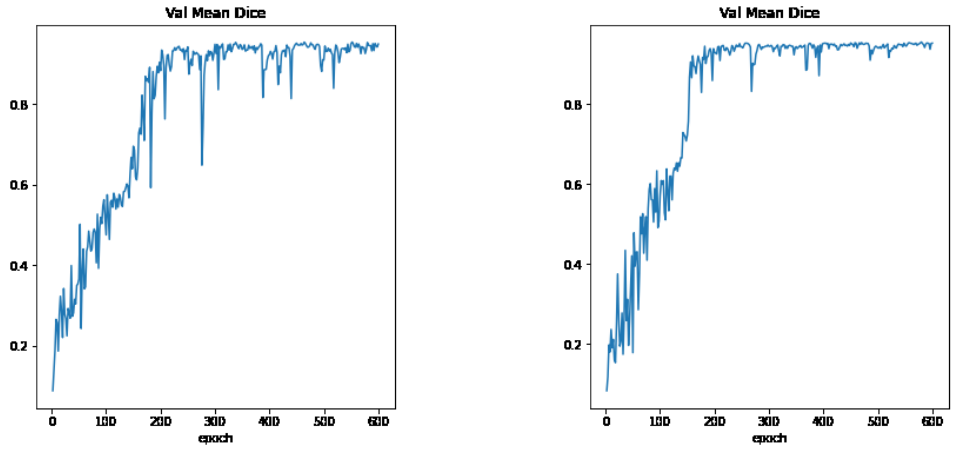

(**a**) (**b**)

Figure 4.16 Mean dice of the model: (a) left femoral segmentation model; (b) right femoral segmentation model.

The best metric was 0.9547 when the left femur segmentation model was trained with peoch of 580, and another model obtained a metric of 0.9450 when the peoch reached 552. When the images in Dataset C are segmented according to the injury site using the two models that were trained, the left segmentation model's evaluation metric is 0.85, and the evaluation metric of the right segmentation model is 0.81, using the manual labeling information as the ground truth. Figure 4.17 shows a comparison of the 3D images of the manually segmented proximal femur and the segmented femur using the model.

4.4.2 Registration Evaluation

A multi-resolution framework using negative mutual information as the image similarity metric function is used to perform coarse registration of the images in each case, and their metric values are listed in Table 4.2.

Table 4.2 Coarse registration metrics.

Left femur	Case no.	1	2	3	4	5
	Metric value	−0.271	−0.039	−0.285	−0.322	−0.467
Right femur	Case no.	6	7	8	9	10
	Metric value	−0.367	−0.259	−0.178	−0.097	−0.331

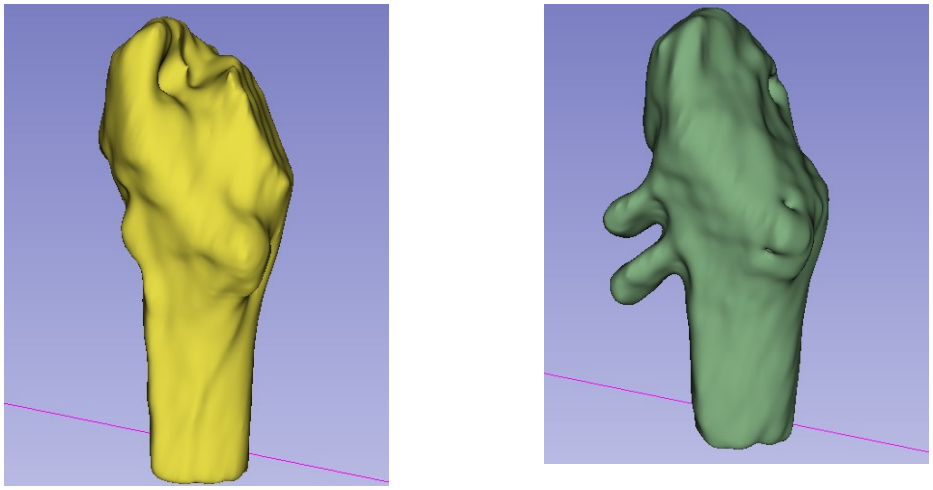

(a) **(b)**

Figure 4.17 Comparison of femoral segmentation results: (a) manual segmentation; (b) segmentation using model.

Figure 4.18 plots the coarse-aligned image with the 3D schematic of the femur. The yellow model presents the skeletal part of the fixed image, and the purple is the floating image. In the femur part, the two images do not entirely overlap; instead, some of the pelvic bones overlap.

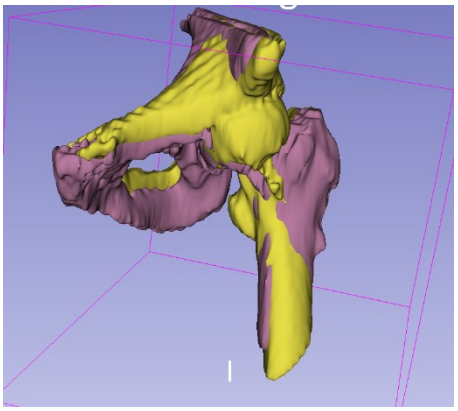

Figure 4.18 Spatial location of femur after coarse alignment.

In the experiments, the label obtained using the segmentation model and the manual annotation is used as the mask to fine align the images, respectively, and the mutual information from the two methods is presented in Table 4.3. For the images in the same case, there is no significant difference in the precision-aligned metric value obtained when different masks are selected.

Table 4.3 Results comparison of fine alignment using different masks.

Left femur		Case No.	1	2	3	4	5
	Metric value	Segmentation model	−0.306	−0.065	−0.364	−0.346	−0.308
		Manual labeling	−0.289	−0.046	−0.357	−0.370	−0.312
Right femur		Case No.	6	7	8	9	10
	Metric value	Segmentation model	−0.337	−0.180	−0.256	−0.270	−0.339
		Manual labeling	−0.360	−0.240	−0.231	−0.259	−0.342

Figure 4.19 shows the 3D schematic diagram of the floating image obtained from the two experiments, where the yellow model is the bone in the fixed image, the green model is the result of alignment with the label generated by the segmentation model as the mask, and the red model is the result of manual labeling as the mask.

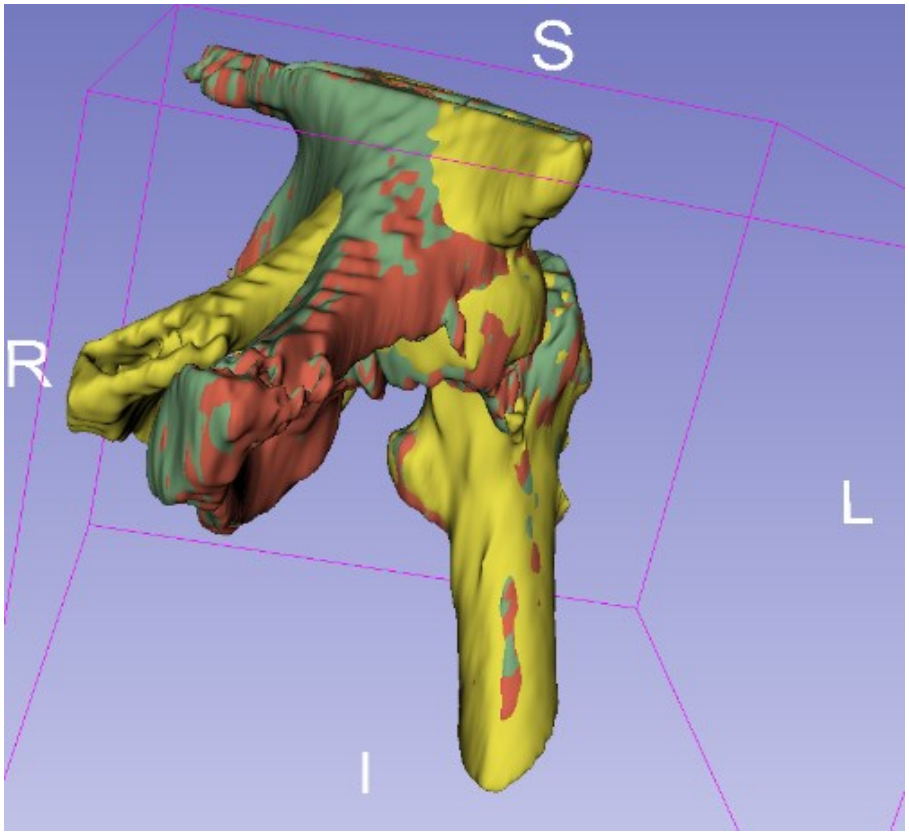

Figure 4.19 Comparison of the results using different labeling as a fine-aligned mask.

The fine-aligned CT images were transformed by 3D reconstruction to obtain the point cloud data, as in Figure 4.20.

4.4.3 Displacement measurement

To ensure that the 3D point cloud data can represent the actual size and accurate displacement calculation of Hansson pins, we compared the pins' actual length with the measured length of the point cloud data, and the results are reported in Table 4.4. Each case

contains two sets of CT images, fixed images, and floating images; all the results are presented. The error between the length of the pins calculated by the point cloud and the actual length is within 2 mm.

Table 4.4 Comparison of the actual length of Hansson pins with the point cloud data.

Fracture Site	Case No.	Proximal Pin (mm)			Distal Pin (mm)		
		Actual Length	Fixed Images	Floating Images	Actual Length	Fixed Images	Floating Images
Left femur	1	80	80.38	82.19	90	90.38	90.39
	2	80	80.28	80.46	90	90.31	90.14
	3	70	70.07	69.49	85	86.96	85.75
	4	80	81.07	81.32	90	90.98	90.10
	5	85	86.77	84.93	95	96.36	96.46
Right femur	6	90	90.24	91.98	100	101.29	101.32
	7	80	79.84	79.89	95	95.29	95.00
	8	80	80.43	79.31	90	90.51	89.86
	9	80	80.61	79.38	90	90.82	89.27
	10	75	75.46	75.44	90	90.80	90.94

Table 4.5 shows the displacement distances of the two endpoints of pins calculated using the point cloud data. Additionally, as discussed in Section 3.3, a new spatial coordinate system was established with the fixed image pins as the reference. We converted the displacements to the new coordinate system for calculating Hansson pins' displacement in a specific direction. The displacements of the pin's endpoints in the three directions in space are listed in Table 4.6.

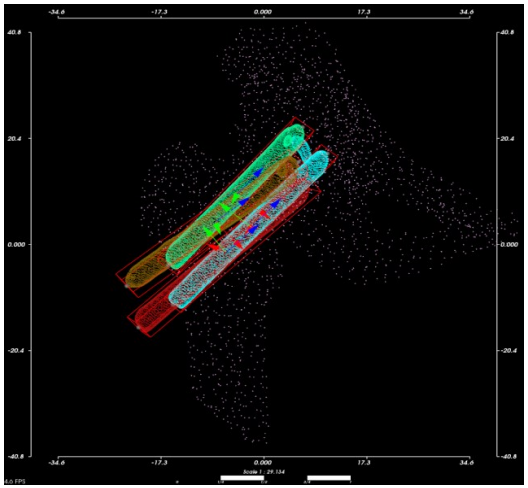

(**a**)

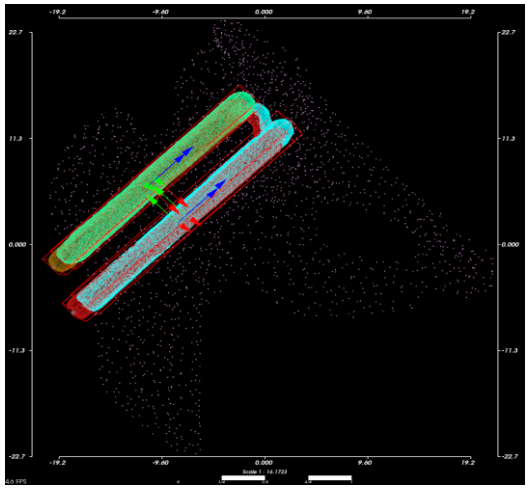

(**b**)

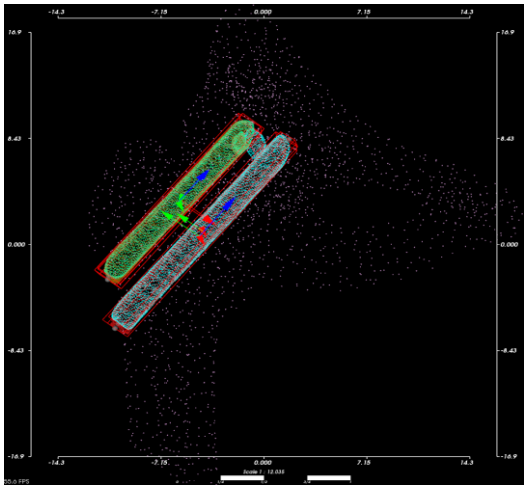

(**c**)

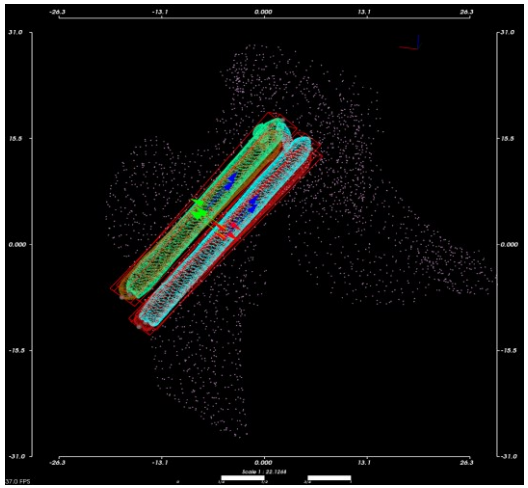

(**d**)

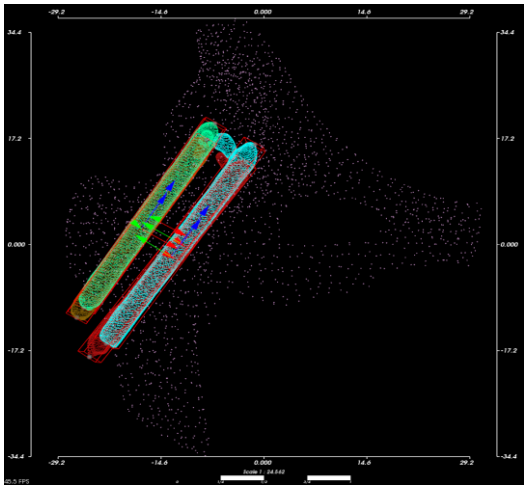

(**e**)

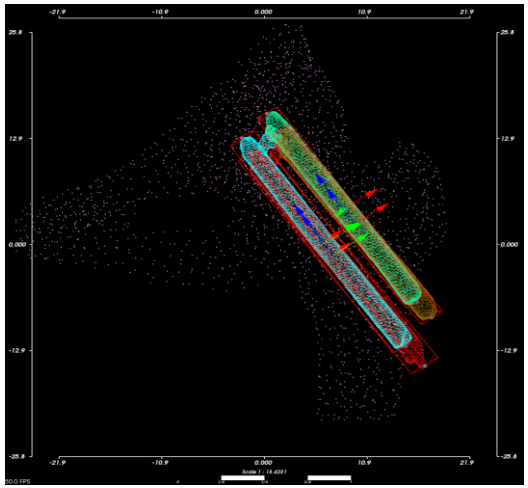

(f)

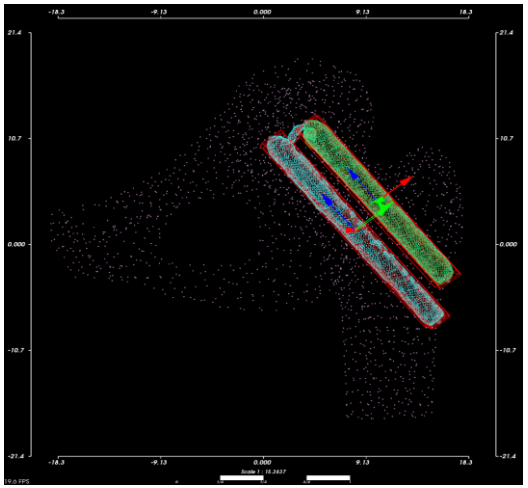

(g)

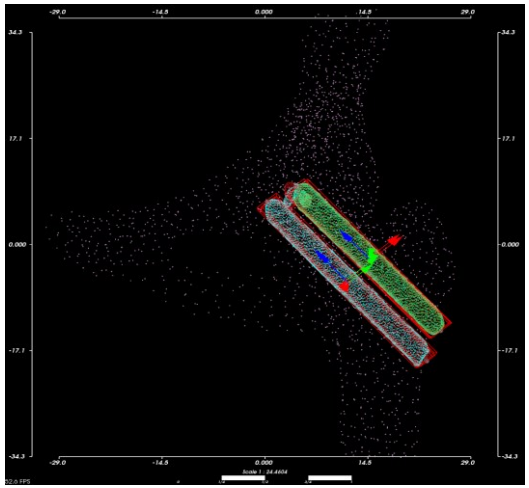

(h)

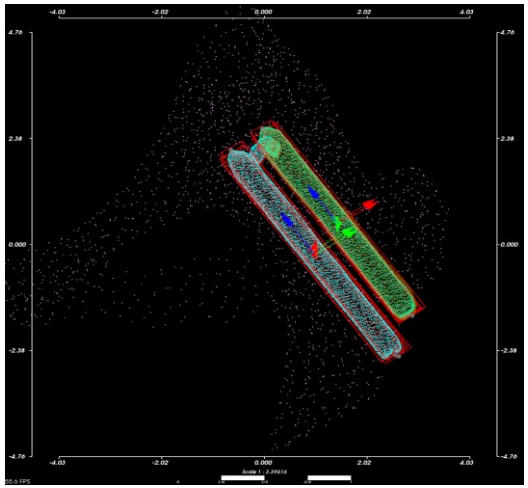

(i)

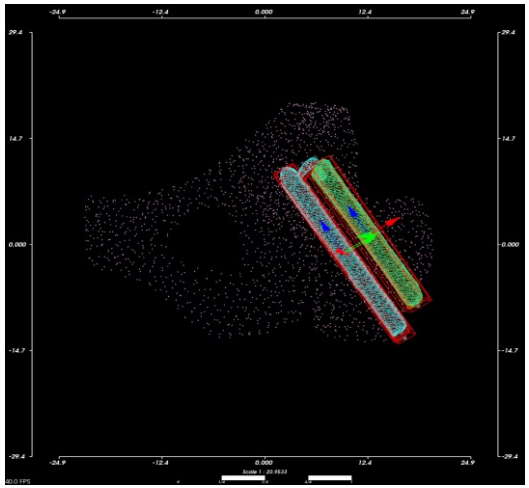

(j)

Figure 4.20 Hansson pins point clouds: from (a–e) is the Hansson pins point clouds used for the left femur; from (f–j) is the Hansson pins point clouds used for the right femur.

Table 4.5 Hansson pins displacement measurement based on 3D point clouds.

Fracture Site	Case No.	Proximal Pin (mm)			Distal Pin (mm)		
		Actual Length	Top Movement	Bottom Movement	Actual Length	Top Movement	Bottom Movement
Left femur	1	80	19.49	17.44	90	16.51	16.11
	2	80	3.18	3.36	90	4.04	3.83
	3	70	0.49	0.26	85	0.55	0.88
	4	80	4.55	4.06	90	4.93	2.47
	5	85	7.62	4.78	95	7.47	7.58
Right femur	6	90	8.41	8.99	100	8.87	10.59
	7	80	0.68	0.90	95	1.06	0.78
	8	80	1.98	0.93	90	1.25	0.82
	9	80	1.46	0.46	90	2.11	0.78
	10	75	0.36	0.39	90	1.96	2.09

Table 4.6 The displacement of Hansson pins' endpoints in each direction after coordinate transformation.

Fracture Site	Case No.	Proximal Pin Displacement (mm)		Distal Pin Displacement (mm)	
		Top Endpoint	Bottom Endpoint	Top Endpoint	Bottom Endpoint

		x axis	y axis	z axis	x axis	y axis	z axis	x axis	y axis	z axis	x axis	y axis	z axis
Left femur	1	7.76	−7.11	−16.39	−5.54	3.10	−16.34	−1.59	−3.19	−16.22	−0.06	2.78	−15.98
	2	0.23	−0.16	−3.18	−0.26	0.01	−3.36	0.00	−0.79	−3.97	−0.44	0.40	−3.79
	3	−0.06	−0.06	−0.47	0.14	0.06	0.11	−0.22	−0.28	−0.39	0.14	−0.29	0.82
	4	2.78	0.88	−3.50	−1.79	−0.73	−3.60	−0.66	−3.32	−3.42	0.37	0.27	−2.45
	5	0.83	0.43	−7.71	−0.22	−0.43	−4.85	0.33	−1.38	−7.46	−0.30	1.73	−7.49
Right femur	6	−1.81	−3.41	−7.28	1.19	2.02	−8.73	1.07	−1.78	−8.74	−0.06	0.94	−10.72
	7	0.45	0.08	−0.49	−0.57	−0.40	−0.53	−0.23	0.05	−1.03	0.19	−0.16	−0.73
	8	0.37	0.58	−1.84	−0.23	−0.50	−0.72	−0.15	0.10	−1.24	0.54	0.05	−0.58
	9	−0.29	−0.30	−1.38	0.30	−0.26	−0.14	−0.51	−0.32	−2.01	0.09	0.60	−0.44
	10	−0.05	0.31	−0.17	−0.30	−0.19	−0.15	−0.18	−0.34	−1.94	0.10	0.38	−2.07

We compared the manual measurement of implant displacement obtained in Section 3.4 with the femur registration-based measurements proposed in this chapter. The difference between the two experimental results is shown in Table 4.7. The measurement error is within 3 mm, except in Case 3, where the measurement error is −3.57 mm.

Table 4.7 The difference between the implant displacement results obtained by the conventional method and femur registration-based method.

Fracture Site	Case No.	Proximal Pin (mm)			Distal Pin (mm)		
		Actual Length	Top Movement	Bottom Movement	Actual Length	Top Movement	Bottom Movement
Left femur	1	80	−0.77	0.54	90	−0.84	−0.18

	2	80	−0.08	−0.36	90	−0.81	−0.31
	3	70	−3.57	−1.89	85	−0.16	−0.34
	4	80	−1.87	−0.62	90	−1.67	−0.88
	5	85	0.55	0.57	95	1.04	2.26
Right femur	6	90	−1.84	−1.68	100	−2.47	1.77
	7	80	1.37	1.91	95	1.61	1.53
	8	80	2.07	2.09	90	0.69	2.86
	9	80	1.98	1.25	90	2.68	2.64
	10	75	0.11	2.46	90	0.21	2.37

Figures 4.21 and 4.22 depict the errors of the lengths of Hansson pins obtained by the method based on femur registration and conventional method from the actual values, respectively. It is used to evaluate the stability line and accuracy of the measurement method.

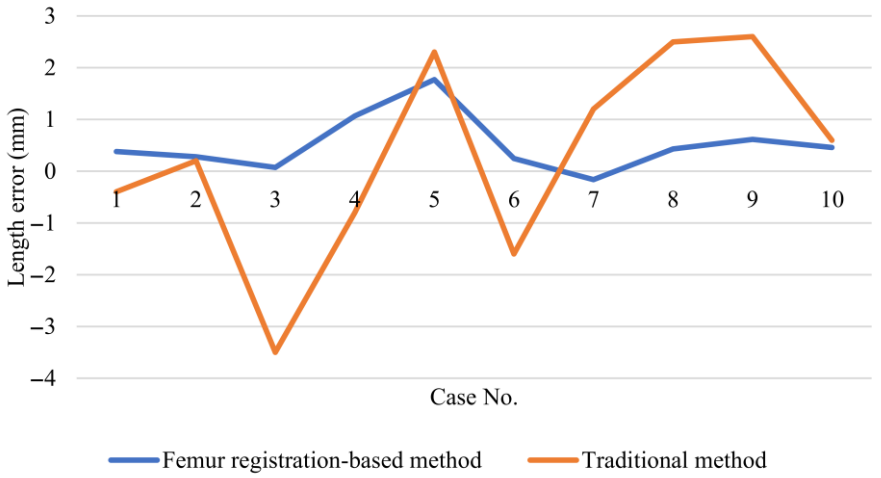

Figure 4.21 Length error of proximal Hansson pins calculated based on femoral registration method and traditional method.

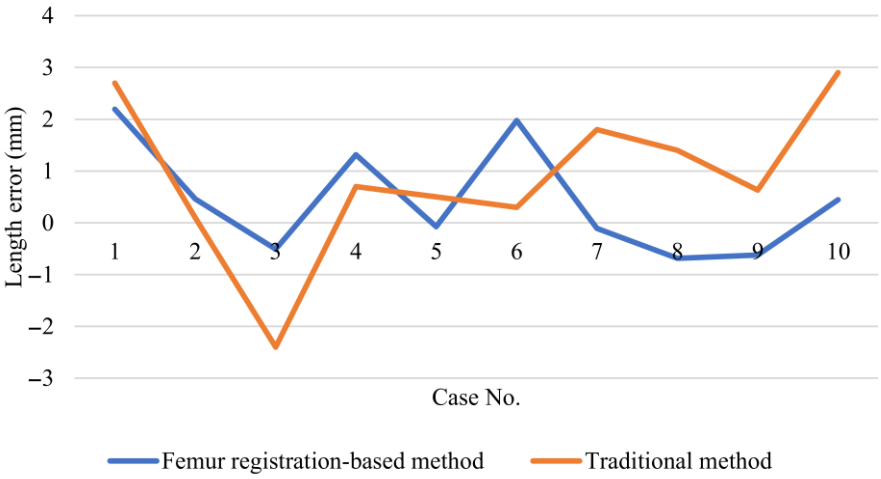

Figure 4.22 Length error of distal Hansson pins calculated based on femoral registration method and traditional method.

4.5 Discussion

Internal fixation using implants is the standard management option for the treatment of stable femoral neck fractures. No evaluation method of the internal

fixation system has been proposed that can use long-term postoperative examination data and measure pins displacement based on the postoperative patient's realistic daily movement. In this chapter, we use the Hansson pins system as the object of study. A neural network with a symmetrical structure was used to segment the injured femur automatically, and the segmented label was used as a mask to register the patient's postoperative CT images at different time points. We calculated the displacement by obtaining the coordinate information of the hip implant from the 3D point cloud generated by the aligned CT images.

This study's focus is to quantify and visualize the movement of the patient's implanted pins after surgery and to evaluate the internal fixation system based on the effect of the patient's regular behavioral habits on the migration of the implant. Generally, the pins' axial displacement is a fundamental criterion, and the quantified displacement of the pins is the most visual data that can be read in radiographs, reflecting the pins' ability to resist axial force. In many postoperative evaluations of orthopedic internal fixation procedures, the degree of implant movement is used as an indicator of the need for reoperation, the mechanical failure of the pins, or the internal fixation device's reliability [80]–[82]. For example, in [83], the migration of screw and K-wire was used as one indicator to analyze the outcome after internal fixation of proximal humeral fractures. Due to the nature of radiographic images, surgeons judge implant failure based on experience only if significant implant displacement occurs. The pins displacement measurement method proposed in this study can quantify the implant's displacement value in any specified direction in 3D space by transforming the coordinate system and visualizing it by 3D reconstruction. Furthermore, we use the segmented femur obtained from a neural network with symmetric properties as the mask for alignment and use the multi-resolution framework as the core for automatic alignment of CT images, which reduces human intervention and dramatically reduces time consumption. Therefore, it can reduce the workload of surgeons and their reliance on experience.

In this chapter's experiments, two sets of CT images for measurement with a one-year interval between scans. In contrast to many literature pieces that use hydraulic devices or finite element simulations to simulate a single motion scenario of the patient, the evaluation method proposed in this chapter is based on the analysis of the pins data presented after the real behavior. Furthermore, we can fuse the patient's CT

data at multiple time points and combine the patient-specific health information for the evaluation of the internal fixation system, avoiding the simulation results that do not match with the real data due to simplified parameters. More importantly, the CT images we use can provide three-dimensional coordinate data with higher accuracy of results compared to two-dimensional radiological images.

We used negative mutual information for the experiments with the coarse and fine alignment of CT images as the evaluation function of image overlap. The metric values of fine registration in some cases listed in Table 4.3 are smaller than those of coarse registration. The fine alignment and the coarse alignment have different ranges of effect in the similarity function. In the coarse alignment, the mutual information is calculated with the whole input image as the range, while the fine alignment has a different range due to the mask's use. The metric values in Table 4.3 are to verify whether there is a difference between the registration using manual annotation and the registration using the mask generated by 3D-UNet and are not correlated with the results shown in Table 4.2.

Another interesting finding in this chapter is that in the 10 cases where Hansson pins were used as the internal fixation system, both proximal and distal pins shifted to varying degrees along the axis of the pins, away from the femoral head, and to a small degree in other directions compared to axial migration. Biomechanical analysis is that since the upper body's major weight within the frontal and sagittal planes produce different components on the femur during normal walking [84]. In Case 2, the displacement in both axial and hook directions was significantly greater than in the other cases and may be related to the severity of the patient's osteoporosis, which will continue to be discussed in future studies.

By comparing the lengths of Hansson pins calculated by the femur-based registration method with the traditional method in Figures 4.21 and 4.22, we found that the measurement stability and accuracy of the proposed method are higher than the traditional method. Only in cases 4 and 6, the traditional method's absolute errors are minor compard to the method proposed in this chapter. Moreover, the traditional method's error fluctuation is large, which indicates that the measurement effect is not stable. More importantly, according to Table 4.7, the method proposed in this chapter

consumes much less time than the manual measurement and obtains similar measurement results.

The cases in dataset C were obtained from Hyogo Prefectural Awaji Medical Center. We only collected records of intracapsular fractures in female patients during the four years from March 2012 to January 2015. This data supports the previous literature's statistical findings that femoral fracture incidence is significantly higher in women than in men [53]. Since male and female femurs have the same symmetrical structure, with no significant differences in morphology and stress environment, it will not affect the experimental results' applicability. Moreover, we will continue to focus on the treatment of intracapsular femur fractures, and in future studies, we will add medical image data from male patients for experimental comparisons.

In this chapter, we use Hansson pins as the object of study, and Table 4.6 demonstrates the displacement of the pins along the axial and the hook pointing direction. The crucial step of the method is the registration of the rigid reference. Thus, the method is widely applicable to evaluating internal fixation implants in other fracture sites, and only different segmentation models need to be trained depending on the rigid reference.

A limitation of the current study is that the pins' calculated displacement values are obtained without ground truth for comparison. For this reason, we use mutual information as the evaluation function in the process of registration of CT images and set the convergence minimum to 1e-6 to ensure the maximum overlap of the registered images. The error is limited to an acceptable range by the intuitive evaluation of the 3D images of the two data sets after alignment. Moreover, to ensure the pins' displacement values' validity, we use the actual length of Hansson pins as the parameter criterion for 3D reconstruction in generating 3D point clouds, and the length error is less than 2 mm. Despite the limitations, the results obtained by this method of measurement can accurately reflect the motion trend of the pins. For overcoming the limitations of this study, more biomechanical experiments are needed as a comparison of the results.

4.6 Conclusions

This study refers to address the problems of traditional internal fixation evaluation methods used for intracapsular fractures, which have low applicability, do not fully reflect the actual postoperative condition of patients, time-consuming, and low accuracy. We proposed a rapid evaluation method for internal fixation systems used for femoral neck fractures in the elderly. The method uses a 3D-UNet neural network to segment the injured femur and uses it as a mask to registers CT images scanned at different times. Further, the registered CT images are converted to point cloud data to quantify the implant's displacement in a specific direction. This method does not affect the patient's postoperative recovery and allows the fusion of long-term data for the evaluation of the internal fixation system.

Encouraging experimental results demonstrate that this method gives more reliable results than the traditional manual measurement of pins displacement. Although the evaluation given in this chapter is preliminary, it is widely applicable to implants' displacement after internal fixation procedures at other sites. A wide range of research prospects is available.

Chapter 5
Conclusions

In this study, our main objective is to propose intelligent evaluation methods to measure the stability evaluation of femoral neck internal fixation protocols. We propose an evaluation method for internal femoral fixation based on 3D point cloud alignment and multi-resolution pyramidal frame alignment. Both evaluation methods are based on two sets of CT medical images of patients with femoral neck fractures after internal fixation and after a one-year recovery period, with no additional detection burden on the patients. Most importantly, the CT medical images record information about the displacement of the implant in the patient's real-life environment, avoiding displacement measurement errors caused by simulated data.

Based on the 3D point cloud matching method, the 3D reconstructed femur and implant models are converted into point cloud data. The ICP algorithm is used to align the two sets of point clouds with the femur as the reference for the postoperative period and the interval of one year. The pins point clouds are converted into the same coordinate system to achieve the measurement of implant displacement information.

Based on the evaluation method of multi-resolution pyramidal alignment, the 3D UNet framework is used to train the femur segmentation model, and the CT images are directly used as the original data set for coarse alignment, after which the segmented femur is used as the mask and refined alignment is performed again. The aligned images can be regarded as two sets of CT images transformed into the same coordinate system. The 3D reconstruction of the aligned CT images is performed, and the implant displacement is calculated.

The major difference between these two methods for evaluating the stability of internal fixation is that the 3D point cloud-based alignment method performs 3D reconstruction and alignment first, followed by displacement measurement. In contrast, in the multi-resolution pyramidal framework-based alignment method, the process is the opposite of the first method, in which the original CT images are aligned. Then 3D reconstruction is performed, and displacement is measured. The experimental results show that the measurement results of both methods are

satisfactory, but the multi-resolution pyramid frame-based alignment method requires fewer considered operations and consumes less time than the first method.

5.1 Limitations

We have used rigorous experimental comparisons in our study in order to verify the accuracy of the proposed method, but there are still some limitations of this paper.

In the method of measuring implant displacement based on 3D point cloud matching, we used the traditional manual measurement method to compare with the method proposed in this paper, and although the experimental results showed that the correctness of our measurement method with the manual measurement method was within the error tolerance, we did not have the accurate real displacement of the implant as the ground truth of the experiment. and, in the experimental data preparation stage, the Manual assistance is still required for the three reconstructions of the proximal femur and Hansson pins.

In the multi-resolution pyramid model-based implant displacement measurement method, we trained two segmentation models, one for the left femur and one for the right femur, according to the anatomical location of the patient's injury, limited by the characteristics of the 3D U-net network. The segmentation models for alignment needed to be manually selected before performing femoral alignment, and full automatic operation was not achieved. Despite these limitations, the results obtained by this measurement method can still accurately reflect the motion trend of the pin.

5.2 Further work

The application prospects of these methods can be further extended by improving the methods that have been proposed. Specific improvements include.

1. Perform migration training on other neural network models applied to natural image segmentation to compare the applicability of different networks for x-ray images.

2. Add biomechanical experiments to the implant displacement measurement experiments for comparison and use real pins displacement data as the ground truth

of the experiments to adjust the county official parameters of the 3D reconstruction process.

Appendix A
List of Publication

Academic Journals

[1]. Liu, K., Nagamune, K. and Oe, K., 2020. Analysis of Single Rod to Pin Frame's Bending Deformation on External Fixation Device in Unstable Pelvic Ring Fracture. International Information Institute (Tokyo). Information, 23(3), pp.213-228.

[2]. Liu, K., Nagamune, K., Oe, K., Kuroda, R. and Niikura, T., 2021. Migration Measurement of Pins in Postoperative Recovery of the Proximal Femur Fractures Based on 3D Point Cloud Matching. Medicina, 57(5), p.406.

[3]. Liu, K.; Nagamune, K.; Oe, K.; Kuroda, R.; Niikura, T. A Postoperative Displacement Measurement Method for Femoral Neck Fracture Internal Fixation Implants Based on Femoral Segmentation and Multi-Resolution Frame Registration. Symmetry 2021, 13, 747. https://doi.org/10.3390/sym13050747

International Conferences

[4]. K. Liu, K. Nagamune and K. Oe, "Angle Measurement of Two Rods in External Fixation Bracket Based on Image Processing," 2019 1st International Conference on Electrical, Control and Instrumentation Engineering (ICECIE), 2019, pp. 1-6, doi: 10.1109/ICECIE47765.2019.8974750.

Bibliography

[1]. Swart, E., Roulette, P., Leas, D., Bozic, K.J. and Karunakar, M., 2017. ORIF or arthroplasty for displaced femoral neck fractures in patients younger than 65 years old: an economic decision analysis. JBJS, 99(1), pp.65-75.

[2]. Pauyo, T., Drager, J., Albers, A. and Harvey, E.J., 2014. Management of femoral neck fractures in the young patient: A critical analysis review. World journal of orthopedics, 5(3), p.204.

[3]. Stevens, J.A. and Rudd, R.A., 2013. The impact of decreasing US hip fracture rates on future hip fracture estimates. Osteoporosis International, 24(10), pp.2725-2728.

[4]. Bentler, S.E., Liu, L., Obrizan, M., Cook, E.A., Wright, K.B., Geweke, J.F., Chrischilles, E.A., Pavlik, C.E., Wallace, R.B., Ohsfeldt, R.L. and Jones, M.P., 2009. The aftermath of hip fracture: discharge placement, functional status change, and mortality. American journal of epidemiology, 170(10), pp.1290-1299.

[5]. Mittal, R.; Banerjee, S. Proximal femoral fractures: Principles of management and review of literature. J. Clin. Orthop. Trauma 2012, 3, 15–23, doi:10.1016/j.jcot.2012.04.001.

[6]. Reina, N.; Bonnevialle, P.; Duval, B.R.; Adam, P.; Loubignac, F.; Favier, T.; Massin, P. Internal fixation of intra-capsular proximal femoral fractures in patients older than 80 years: Still relevant? Multivariate analysis of a prospective multicentre cohort. Orthop. Traumatol. Surg. Res. 2017, 103, 3–7, doi:10.1016/j.otsr.2016.10.013.

[7]. Watson, A.; Zhang, Y.; Beattie, S.; Page, R.S. Prospective randomized controlled trial comparing dynamic hip screw and screw fixation for undisplaced subcapital hip fractures. Anz. J. Surg. 2012, 83, 679–683, doi:10.1111/j.1445-2197.2012.06256.x.

[8]. Fitzpatrick, D.C.; Sheerin, D.V.; Wolf, B.R.; Wuest, T.K. A randomized, prospective study comparing intertrochanteric hip fracture fixation with the dynamic hip screw and the dynamic helical hip system in a community practice. Iowa Orthop. J. 2011, 31, 166–172.

[9]. Richards, J.T.; Overmann, A.L.; O'Hara, N.N.; D'Alleyrand, J.-C.; Slobogean, G.P. Internal Fixation Versus Arthroplasty for the Treatment of Nondisplaced Femoral Neck Fractures in the Elderly: A Systematic Review and Meta-Analysis. J. Orthop. Trauma 2020, 34, 42–48, doi:10.1097/bot.0000000000001656.

[10]. Bjørgul, K.; Olav, R. Outcome of undisplaced and moderately displaced femoral neck fractures: A prospective study of 466 patients treated by internal fixation. Acta Orthop. 2007, 78, 498–504.

[11]. Brandt, E.; Verdonschot, N.; van Vugt, A.; van Kampen, A. Biomechanical analysis of the sliding hip screw, cannulated screws and Targon® FN in intracapsular hip fractures in cadaver femora. Injury 2011, 42, 183–187, doi:10.1016/j.injury.2010.08.021.

[12]. Gardner, A.W.; Toh, M.Z.; A Yew, K.S.; Lie, D.T.T.; Chou, S.M. Cannulated versus non-cannulated cancellous screw fixation for femoral neck fractures: A synthetic bone biomechanical study. J. Orthop. Surg. 2015, 23, 41–46, doi:10.1177/230949901502300110.

[13]. Schopper, C.; Zderic, I.; Menze, J.; Muller, D.; Rocci, M.; Knobe, M.; Shoda, E.; Richards, G.; Gueorguiev, B.; Stoffel, K. Better stability and more predictive fixation of the femoral neck system versus two hansson pins in pauwels ii femoral neck fractures: a biomechanical study. Orthop. Proc. 2021, 103, doi:10.1302/1358-992X.2021.4.

[14]. Augat, P.; Bliven, E.; Hackl, S. Biomechanics of Femoral Neck Fractures and Implications for Fixation. J. Orthop. Trauma 2019, 33, S27–S32, doi:10.1097/bot.0000000000001365.

[15]. Mansur, H.; Alvarez, R.; Freitas, A.; Gonçalves, C.B.; Ramos, M.R.F. Biomechanical analysis of femoral neck fracture fixation in synthetic bone. Acta Ortopédica Bras. 2018, 26, 162–165, doi:10.1590/1413-785220182603182288.

[16]. Tianye, L.; Peng, Y.; Jingli, X.; Qiushi, W.; Guangquan, Z.; Wei, H.; Qingwen, Z. Finite element analysis of different internal fixation methods for the treatment of Pauwels type III femoral neck fracture. Biomed. Pharm. 2019, 112, 108658, doi:10.1016/j.biopha.2019.108658.

[17]. Li, J.; Wang, M.; Zhou, J.; Han, L.; Zhang, H.; Li, C.; Li, L.; Hao, M. Optimum Configuration of Cannulated Compression Screws for the Fixation of Unstable Femoral Neck Fractures: Finite Element Analysis Evaluation. Biomed Res. Int. 2018, 2018, 1–10, doi:10.1155/2018/1271762.

[18]. Li, J.; Wang, M.; Li, L.; Zhang, H.; Hao, M.; Li, C.; Han, L.; Zhou, J.; Wang, K. Finite element analysis of different configurations of fully threaded cannulated screw in the treatment of unstable femoral neck fractures. J. Orthop. Surg. Res. 2018, 13, 272, doi:10.1186/s13018-018-0970-3.

[19]. Garden, R.S., 1961. Low-angle fixation in fractures of the femoral neck. The Journal of Bone and Joint Surgery. British volume, 43(4), pp.647-663.

[20]. Der Pauwels, F., 1935. Schenkelhalsbruch-ein mechanisches problem: grundlagen des heilungsvorganges, prognose und therapie. Ferdinan enke. Verlag, Stuttgart.

[21]. Lowe, J.A., Crist, B.D., Bhandari, M. and Ferguson, T.A., 2010. Optimal treatment of femoral neck fractures according to patient's physiologic age: an evidence-based review. Orthopedic Clinics, 41(2), pp.157-166.

[22]. Zhao S, Gao W, Shan S, et al. Enhance the alignment accuracy of active shape models using elastic graph matching[C]//International Conference on Biometric Authentication. Springer, Berlin, Heidelberg, 2004: 52-58.

[23]. The National Library of Medicine presents MedPix. https://medpix.nlm.nih.gov/home, Accessed 25 February 2021.

[24]. A. Setio et al., "Pulmonary nodule detection in CT images using multiview convolutional networks," IEEE Trans. Med. Imag., vol. 35, no. 5, pp. 1160–1169, May 2016.

[25]. Ketaro Wada, labelme: Image Polygonal Annotation with Python,2016; software available at https://github.com/wkentaro/labelme.

[26]. Zarattini, G.; Breda, L.; Zacharia, M.; Sibona, F. Intra-pelvic migration of sliding hip screw during osteosynthesis of hip fracture: a rare avoidable intraoperative complication. Journal of orthopaedic case reports 2015, 5, 25.

[27]. Parker, M.J. The management of intracapsular fractures of the proximal femur. The Journal of Bone and Joint Surgery. British volume 2000, 82, 937–941.

[28]. Mittal, R.; Banerjee, S. Proximal femoral fractures: principles of management and review of literature. journal of clinical orthopaedics and trauma 2012, 3, 15–23.

[29]. Haentjens, P., Casteleyn, P.P. and Opdecam, P., 1994. Hip arthroplasty for failed internal fixation of intertrochanteric and subtrochanteric fractures in the elderly patient. Archives of orthopaedic and trauma surgery, 113(4), pp.222-227.

[30]. Bosch, U.; Schreiber, T.; Krettek, C. Reduction and fixation of displaced intracapsular fractures of the proximal femur. Clinical Orthopaedics and Related Research® 2002, 399, 59–71.

[31]. Campbell, W. Shoulder and elbow injuries. Canale ST, Beaty JH. Campbell's Operative Orthopaedics. 11th ed. Philadelphia: Mosby, Elsevier 2008, pp. 2640–5.

[32]. Li, X.; Heffernan, M.J.; Kane, C.; Leclair, W. Medial pelvic migration of the lag screw in a short gamma nail after hip fracture fixation: a case report and review of the literature. Journal of orthopaedic surgery and research 2010, 5, 62.

[33]. Weil, Y.A.; Gardner, M.J.; Mikhail, G.; Pierson, G.; Helfet, D.L.; Lorich, D.G. Medial migration of intramedullary hip fixation devices: a biomechanical analysis. Archives of Orthopaedic and Trauma Surgery 2008, 128, 227–234.

[34]. Cavalcante, E.L.B.; de Faria, F.J.; Rodrigues, R.A.; Ribeiro Filho, J.E.G.; de Oliveira, S.G.; Elias, N. Intrapelvic Migration of the Cephalic Screw of a Proximal Femoral Long Intramedullary Nail: Case Report. Revista Brasileira de Ortopedia 2020, 55, 121–124.

[35]. Werner-Tutschku, W.; Lajtai, G.; Schmiedhuber, G.; Lang, T.; Pirkl, C.; Orthner, E. Intra-and perioperative complications in the stabilization of per-and subtrochanteric femoral fractures by means of PFN. Der Unfallchirurg 2002, 105, 881.

[36]. Thies, H.; Reinhardstoettner, C.v. Mediales Auswandern der Schenkelhalsschraube bei Gammanagelung. Der Unfallchirurg 2004, 107, 706–708.

[37]. Lucke, M.; Burghardt, R.D.; Siebenlist, S.; Ganslmeier, A.; Stöckle, U. Medial migration of lag screw with intrapelvic dislocation in gamma nailing-a unique problem? A report of 2 cases. Journal of orthopaedic trauma 2010, 24, e6–e11.

[38]. Koaban, S.; Alatassi, R.; Alharbi, S.; Alshehri, M.; Alghamdi, K. The relationship between femoral neck fracture in adult and avascular necrosis and nonunion: a retrospective study. Annals of Medicine and Surgery 2019, 39, 5–9.

[39]. Hesse, B.; Gächter, A. Complications following the treatment of trochanteric fractures with the gamma nail. Archives of orthopaedic and trauma surgery 2004, 124, 692–698.

[40]. Jones, H.W.; Johnston, P.; Parker, M. Are short femoral nails superior to the sliding hip screw? A meta-analysis of 24 studies involving 3,279 fractures. International orthopaedics 2006, 30, 69–78.

[41]. Heineman, D.J.; van Buijtenen, J.M.; Heuff, G.; Derksen, E.J.; Pöll, R.G. Intra-abdominal migration of a lag screw in gamma nailing: report of a case. Journal of Orthopaedic Trauma 2010, 24, e119–e122.

[42]. Thein, E.; De Cannière, A.; Burn, A.; Borens, O. Medial migration of lag screw after gamma nailing. Injury 2014, 45, 1275–1279.

[43]. Kaur, J. and Chopra, R., 2010. Three dimensional CT reconstruction for the evaluation and surgical planning of mid face fractures: a 100 case study. Journal of maxillofacial and oral surgery, 9(4), pp.323-328.

[44]. Naeem, A., Gemal, H. and Reed, D., 2017. Imaging in traumatic mandibular fractures. Quantitative imaging in medicine and surgery, 7(4), p.469.

[45]. Hansson, L.I. Osteosynthesis with the Hook-Pin in Slipped Capital Femoral Epiphysis. Acta Orthop. Scand. 1982, 53, 87–96, doi:10.3109/17453678208992184.

[46]. Ge, Y.; Maurer, C.R., Jr; Fitzpatrick, J.M. Surface-based 3D image registration using the iterative closest-point algorithm with a closest-point transform. Medical Imaging 1996: Image Processing. Int. Soc. Opt. Photonics 1996, 2710, 358–367.

[47]. Fedorov, A.; Beichel, R.; Kalpathy-Cramer, J.; Finet, J.; Fillion-Robin, J.-C.; Pujol, S.; Bauer, C.; Jennings, M.; Fennessy, F.; Sonka, M.; et al. 3D Slicer as an image computing platform for the Quantitative Imaging Network. Magn. Reson. Imaging 2012, 30, 1323–1341, doi:10.1016/j.mri.2012.05.001.

[48]. Otsu, N. A threshold selection method from gray-level histograms. IEEE Trans. Syst. ManCybern. 1979, 9, 62–66, doi:10.1109/tsmc.1979.4310076.

[49]. McNeel, R.; others. Rhinoceros 3D. Retrieved Jan 2009, 15. Available online: https://www.rhino3d.com (accessed on 21 April 2021).

[50]. Medixant. RadiAnt DICOM Viewer. Available online: https://www.radiantviewer.com (accessed on 9 March 2020).

[51]. Haider, T.; Schnabel, J.; Hochpöchler, J.; Wozasek, G.E. Femoral shortening does not impair functional outcome after internal fixation of femoral neck fractures in non-geriatric patients. Arch. Orthop. Trauma Surg. 2018, 138, 1511–1517, doi:10.1007/s00402-018-3011-0.

[52]. Chen, W.-C.; Yu, S.-W.; Tseng, I.-C.; Su, J.-Y.; Tu, Y.-K.; Chen, W.-J. Treatment of Undisplaced Femoral Neck Fractures in the Elderly. J. Trauma Inj. Infect. Crit. Care 2005, 58, 1035–1039, doi:10.1097/01.ta.0000169292.83048.17.

[53]. Brauer, C.A., Coca-Perraillon, M., Cutler, D.M. and Rosen, A.B., 2009. Incidence and mortality of hip fractures in the United States. Jama, 302(14), pp.1573-1579..

[54]. Miyamoto, R.G.; Kaplan, K.M.; Levine, B.R.; Egol, K.A.; Zuckerman, J.D. Surgical Management of Hip Fractures: An Evidence-based Review of the Literature. I: Femoral Neck Fractures. J. Am. Acad. Orthop. Surg. 2008, 16, 596–607, doi:10.5435/00124635-200810000-00005.

[55]. Sekeitto, A.R.; Sikhauli, N.; van der Jagt, D.R.; Mokete, L.; Pietrzak, J.R. The management of displaced femoral neck fractures: a narrative review. EFORT Open Rev. 2021, 6, 139–144, doi:10.1302/2058-5241.6.200036.

[56]. Lehtonen, E.J.I., Stibolt Jr, R.D., Smith, W., Wills, B., Pinto, M.C., McGwin Jr, G., Shah, A., Godoy-Santos, A.L. and Naranje, S., 2018. Trends in surgical treatment of femoral neck fractures in the elderly. Einstein (São Paulo), 16(3). .

[57]. Eiskjaer, S.; E Ostgård, S. Risk factors influencing mortality after bipolar hemiarthroplasty in the treatment of fracture of the femoral neck. Clin. Orthop. Relat. Res. 1991, 270, 295–300.

[58]. Lu, Q.; Tang, G.; Zhao, X.; Guo, S.; Cai, B.; Li, Q. Hemiarthroplasty versus internal fixation in super-aged patients with undisplaced femoral neck fractures: A 5-year follow-up of randomized controlled trial. Arch. Orthop. Trauma Surg. 2016, 137, 27–35, doi:10.1007/s00402-016-2591-9.

[59]. Oñativia, I.J.; Slulittel, P.A.; Dilernia, F.D.; Viezcas, J.M.G.; Vietto, V.; Ramkumar, P.N.; Buttaro, M.A.; Piuzzi, N.S. Outcomes of nondisplaced intracapsular femoral neck fractures with internal screw fixation in elderly patients: A systematic review. HIP Int. 2018, 28, 18–28, doi:10.5301/hipint.5000532.

[60]. Nanty, L.; Canovas, F.; Rodriguez, T.; Faure, P.; Dagneaux, L. Femoral neck shortening after internal fixation of Garden I fractures increases the risk of femoral head collapse. Orthop. Traumatol. Surg. Res. 2019, 105, 999–1004, doi:10.1016/j.otsr.2019.05.009.

[61]. Johnson, J.P.; Kleiner, J.; Goodman, A.D.; Gil, J.A.; Daniels, A.H.; Hayda, R.A. Treatment of femoral neck fractures in patients 45–64 years of age. Injure 2019, 50, 708–712, doi:10.1016/j.injury.2018.11.020.

[62]. Bigoni, M.; Turati, M.; Leone, G.; Caminita, A.D.; D'Angelo, F.; Munegato, D.; Zatti, G. Internal fixation of intra-capsular femoral neck fractures in elderly patients: Mortality and reoperation rate. Aging Clin. Exp. Res. 2020, 32, 1–6.

[63]. Mansur, H.; Alvarez, R.; Freitas, A.; Gonçalves, C.B.; Ramos, M.R.F. Biomechanical analysis of femoral neck fracture fixation in synthetic bone. Acta Ortop. Bras. 2018, 26, 162–165, doi:10.1590/1413-785220182603182288.

[64]. Schopper, C.; Zderic, I.; Menze, J.; Müller, D.; Rocci, M.; Knobe, M.; Shoda, E.; Richards, G.; Gueorguiev, B.; Stoffel, K. Higher stability and more predictive fixation with the Femoral Neck System versus Hansson Pins in femoral neck fractures Pauwels II. J. Orthop. Transl. 2020, 24, 88–95, doi:10.1016/j.jot.2020.06.002.

[65]. Li, J.; Wang, M.; Li, L.; Zhang, H.; Hao, M.; Li, C.; Han, L.; Zhou, J.; Wang, K. Finite element analysis of different configurations of fully threaded cannulated screw in the treatment of unstable femoral neck fractures. J. Orthop. Surg. Res. 2018, 13, 272, doi:10.1186/s13018-018-0970-3.

[66]. Augat, P.; Bliven, E.; Hackl, S. Biomechanics of Femoral Neck Fractures and Implications for Fixation. J. Orthop. Trauma 2019, 33, S27–S32, doi:10.1097/bot.0000000000001365.

[67]. Bauman, Z.M.; Grams, B.; Yanala, U.; Shostrom, V.; Waibel, B.; Evans, C.H.; Cemaj, S.; Schlitzkus, L.L. Rib fracture displacement worsens over time. Eur. J. Trauma Emerg. Surg. 2020, 1–6, doi:10.1007/s00068-020-01353-w.

[68]. Bugaev, N.; Breeze, J.L.; Alhazmi, M.; Anbari, H.S.; Arabian, S.S.; Holewinski, S.; Rabinovici, R. Magnitude of rib fracture displacement predicts opioid requirements. J. Trauma Acute Care Surg. 2016, 81, 699–704, doi:10.1097/ta.0000000000001169.

[69]. Eastwood, D.M.; Gregg, P.J.; Atkins, R.M. Intra-articular fractures of the calcaneum. Part I: Pathological anatomy and classification. J. Bone Joint Surg. Br. 1993, 75, 183–188.

[70]. Tajbakhsh, N.; Jeyaseelan, L.; Li, Q.; Chiang, J.N.; Wu, Z.; Ding, X. Embracing imperfect datasets: A review of deep learning solutions for medical image segmentation. Med. Image Anal. 2020, 63, 101693, doi:10.1016/j.media.2020.101693.

[71]. Afua A. Yorke, Gary C. McDonald, David Solis Jr., Thomas Guerrero. (2019) Pelvic Reference Data. The Cancer Imaging Archive. DOI: 10.7937/TCIA.2019.woskq5oo.

[72]. Clark K, Vendt B, Smith K, Freymann J, Kirby J, Koppel P, Moore S, Phillips S, Maffitt D, Pringle M, Tarbox L, Prior F. The Cancer Imaging Archive (TCIA): Maintaining and Operating a Public Information Repository, Journal of Digital Imaging, Volume 26, Number 6, December, 2013, pp 1045-1057. DOI: 10.1007/s10278-013-9622-7.

[73]. Hansson, L.I. Osteosynthesis with the Hook-Pin in Slipped Capital Femoral Epiphysis. Acta Orthop. Scand. 1982, 53, 87–96, doi:10.3109/17453678208992184.

[74]. Lv, X. Medical Image Alignment Techniques and Applications, 1st ed.; Science Press: Beijing, China, 2015; pp. 120–129.

[75]. Hans J. Johnson, Matthew M. McCormick, and Luis Ibanez. 2015. The ITK Software Guide Book 1: Introduction and Development Guidelines - Volume 1. Kitware, Inc., Clifton Park, NY, USA.; pp. 377–386.

[76]. Çiçek, Ö.; Abdulkadir, A.; Lienkamp, S.S.; Brox, T.; Ronneberger, O. 3D U-Net: Learning dense volumetric segmentation from sparse annotation. In Proceedings of the International Conference on Medical Image Computing and Computer-Assisted Intervention, Athens, Greece, 17–21 October 2016; Springer: Cham, Switzerland, 2016; pp. 424–432.

[77]. Moeskops, P.; Wolterink, J.M.; Van Der Velden, B.H.M.; Gilhuijs, K.G.A.; Leiner, T.; Viergever, M.A.; Išgum, I. Deep Learning for Multi-task Medical Image Segmentation in Multiple Modalities. In Proceedings of the International Conference on Medical Image Computing and Computer-Assisted Intervention, Athens, Greece, 17–21 October 2016; Springer: Cham, Switzerland, 2016; pp. 478–486.

[78]. Wold, S.; Esbensen, K.; Geladi, P. Principal component analysis. Chemom. Intell. Lab. Syst. 1987, 2, 37–52.

[79]. The MONAI Consortium. Project MONAI. Zenodo. http://doi.org/10.5281/zenodo.4323059 (Available online: https://monai.io/ accessed on 15 December 2020).

[80]. Zhang, Q.; Song, L.; Ning, S.; Xie, H.; Li, N.; Wang, Y. Recent advances in rib fracture fixation. J. Thorac. Dis. 2019, 11, S1070–S1077, doi:10.21037/jtd.2019.04.99.

[81]. Rancy, S.K.; Malliaris, S.D.; Bogner, E.A.; Wolfe, S.W. Intramedullary Fixation of Distal Radius Fractures Using CAGE-DR Implant. J. Wrist Surg. 2018, 7, 358–365, doi:10.1055/s-0038-1669438.

[82]. Jacobs, N.; Seghi, R.; Johnston, W.M.; Yilmaz, B. Displacement and performance of abutments in narrow-diameter implants with different internal connections. J. Prosthet. Dent. 2021, doi:10.1016/j.prosdent.2020.11.008.

[83]. Della Rotonda, G.; Guastafierro, A.; Viglione, S.; Russo, F.; Coscione, A.V.; Ciccarelli, M.; Russo, R. Analysis of early and late clinical and radiologic complications of proximal humeral fractures using open reduction, internal fixation, and intramedullary titanium cage augmentation. J. Shoulder Elb. Surg. 2020, 29, 1843–1851, doi:10.1016/j.jse.2020.01.077.

[84]. Bergmann, G.; Bender, A.; Dymke, J.; Duda, G.; Damm, P. Standardized Loads Acting in Hip Implants. PLoS ONE 2016, 11, e0155612, doi: 10.1371/journal.pone.0155612.